Maria João Quitoles De Oliveira
Licenciada em Biologia Celular e Molecular

Plasmonic substrates for ultrasensitive surface-enhanced Raman spectroscopy: application to the detection of food toxins

Dissertação para obtenção do Grau de Mestre em Biotecnologia

Orientador: Prof. Doutor Hugo Manuel Brito Águas, Faculdade de Ciências e Tecnologia da Universidade Nova de Lisboa
Co-orientador: Prof. Doutor José Ricardo Ramos Franco Tavares, Faculdade de Ciências e Tecnologia da Universidade Nova de Lisboa

Júri:

Presidente: Prof. Doutor Pedro Miguel Calado Simões
Arguente: Doutor César António Tonicha Laia
Vogal: Prof. Doutor Hugo Manuel Brito Águas

Setembro 2015

FACULDADE DE CIÊNCIAS E TECNOLOGIA
UNIVERSIDADE NOVA DE LISBOA

Maria João Quitoles De Oliveira
Licenciada em Biologia Celular e Molecular

Plasmonic substrates for ultrasensitive surface-enhanced Raman spectroscopy: application to the detection of food toxins

Dissertação para obtenção do Grau de Mestre em Biotecnologia

Orientador: Prof. Doutor Hugo Manuel Brito Águas, Faculdade de Ciências e Tecnologia da Universidade Nova de Lisboa
Co-orientador: Prof. Doutor José Ricardo Ramos Franco Tavares, Faculdade de Ciências e Tecnologia da Universidade Nova de Lisboa

Júri:

Presidente: Prof. Doutor Pedro Miguel Calado Simões
Arguente: Doutor César António Tonicha Laia
Vogal: Prof. Doutor Hugo Manuel Brito Águas

Setembro 2015

Plasmonic substrates for ultrasensitive surface-enhanced Raman spectroscopy: application to the detection of food toxins

Para a minha avó Soledade,
com saudade

Para os meus Pais,
"Que nos dão as asas…. E o céu para voarmos bem alto"
James Rollins

Acknowledgements

Agradeço ao Professor Hugo Águas por me ter aceitado como orientanda com a prontidão de um clic, por me ter orientado ao longo deste ano com a sua competência científica e alegre disponibilidade.

Ao Professor Ricardo Franco que sendo meu coorientador me guiou nas encruzilhadas que por vezes o trabalho de investigação encontra, pela sua paciência, conselhos e resposta rápida.
Estou muito grata pelo seu encorajamento em momentos menos fáceis.

Agradeço também ao coordenador do meu mestrado, Professor Carlos Salgueiro, pela eficiência e rapidez que sempre demonstrou no esclarecimento de dúvidas e pela ajuda que simpaticamente me deu na solução de problemas mais burocráticos.

Ao Professor João Sotomayor por me ter ensinado a medir o ângulo de contacto.

Ao departamento de Conservação e Restauro, particularmente à Professora Maria João Melo e Professora Márcia Vilarigues por me terem permitido trabalhar com o espectrómetro de Raman, tão essencial ao meu trabalho.

Ao Doutor Pedro Quaresma pelo esclarecimento de dúvidas e boa disposição, bem como, pelas suas nanostrelas de prata.

Às Mestres Ana Marques e Mafalda Costa, pela disponibilidade para lidar com as idiossincrasias da impressora a cera.

À Mestre Andreia Araújo por me ter ajudado na técnica de deposição física de vapor.

À Mestre Vanessa Otero, pela paciência no esclarecimento de todas as dúvidas, preocupação, conselhos, mas sobretudo pela boa-disposição contagiante mesmo nos dias menos bons! À Tatiana Vitorino por ser madrugadora como eu e me abrir o laboratório, e à Marta por me ter deixado encantar pelas obras em que trabalhava. Aos restantes elementos do laboratório de Conservação e Restauro, Rita, Susana, e Miguel, obrigada pela simpatia e disponibilidade.

À Doutora Inês Gomes por todas as discussões para tentar solucionar problemas, por todos os conselhos, motivação, encorajamento e "bilhetinhos"! Essencialmente, por toda a tua paciência, és uma excelente pessoa e foi um prazer poder conhecer-te!

Às minhas colegas Ana Inês Reis e Mariana Coutinho, pela alegria, almoços e disparates. Tornaram os infindáveis dias de laboratório mais leves.

Aos meus "orientandos", António Lopez e Catarina Bombaça, por me terem permitido desorientá-los proporcionando-me assim a minha primeira experiência de ensino.

À minha vizinha Raquel Maricato, que há 9 anos nos aturamos e que espero que assim continue!

À Ana Nascimento, Marisa Cruz e Tatiana Burrinha, por estarem sempre presentes mesmo nos piores momentos dando-me sempre apoio e força. Pelas conversas "parvoíces" e me fazerem rir. Obrigada por me aturarem e serem minhas amigas!

Aos meus avós, Bina, Francisco e Zé. Obrigada por se preocuparem comigo e o meu bem-estar. Pela força e carinho que me transmitem diariamente. São um exemplo a seguir e sinto muito orgulho por vos ter na minha Vida.

À minha Piglet, pela paciência nas noites de luz acesa a trabalhar. Pelas gargalhadas e uma compreensão que é só nossa. Pelas discussões, carinho e amor. És uma excelente pessoa mesmo que não o saibas tão bem quanto eu. Tenho muito orgulho em te chamar minha irmã.

Ao David, por tudo. Pela pessoa genuinamente boa que és, pelo apoio incondicional e paciência que demonstras diariamente, mesmo quando eu não mereço. Obrigada pelo carinho e amor mais do que alguma vez pensei ser possível. Não há palavras para expressar o quanto sou feliz ao teu lado, obrigada por me fazeres rir. Obrigada por me amares.

Aos meus pais, porque dizer obrigada parece, é, muito pouco. Vocês apoiam-me sempre nas minhas escolhas, mesmo tendo eu tendência para o caminho mais difícil. Obrigada por me ouvirem a falar sobre o meu trabalho e tentarem aconselhar-me, mesmo não o percebendo. Obrigada, porque não têm sido anos fáceis, mas nós os quatro continuamos uma família unida capaz de ultrapassar todas as montanhas. Obrigada por tudo.

"The endless cycle of idea and action,
Endless invention, endless experiment,
Brings knowledge of motion, but not of stillness;
Knowledge of speech, but not of silence;
Knowledge of words, and ignorance of the Word.
All our knowledge brings us nearer to our ignorance,
All our ignorance brings us nearer to death,
But nearness to death no nearer to God.
Where is the Life we have lost in living?
Where is the wisdom we have lost in knowledge?
Where is the knowledge we have lost in information?
The cycles of Heaven in twenty centuries
Bring us farther from God and nearer to the Dust."

T.S. Eliot

Abstract

The food contaminants consist in chemical substances in food products. The contaminants include for example, pesticides, antibiotics, and toxins. Recently there has been an increasing concern in detection of such contaminants not only for the prevention of public health, but also of the environment.

The currently available methods for detection of chemicals in foods are time consuming, expensive and complex to operate. Hence, is necessary to development other methods to overcome the aforementioned disadvantages.

The main objective of this work was to explore the feasibility of surface-enhanced Raman spectroscopy (SERS) as a sensitive, robust, simple and fast technique for the detection of food contaminants. Therefore, two different types of SERS substrate were developed. One of the substrates had paper as solid support matrix, with wells enclosed by hydrophobic barriers (two paper types were studied, chromatography and office). Nanoparticles (NPs) of silver, spherical and star-shaped, were chemically synthesized and deposited in the wells by *drop-casting*. The SERS efficiency study highlighted the office paper as the most appropriate support, due to the greater retention of NPs in star-shape on its surface. The detection limit values (LOD) and quantitation (LOQ) for rhodamine 6G (R6G) were 0.17±0.04 and 2.5±0.5 ppb, respectively. This substrate has proven reproducible and stable over time (5 weeks) with relative standard deviations (RSD) of 1.7 % and 7.3 %, respectively.

The second substrate was made by physical vapor deposition (PVD) allowing a layer of spherical NPs. The LOD and LOQ values for R6G were 0.015±0.002 and 1.1±0.2 ppb, respectively. The proof-of-concept study was conducted with malathion and domoic acid (DA) and was not possible to detect DA. However, the LOD and LOQ for malathion in paper SERS substrate were ≈3944 and ≈1652 ppm respectively, and for the PVD substrate were, ≈925 and ≈5644 ppm, respectively. Both SERS substrates and their production method, were sensitive, robust, and inexpensive, allowing the rapid detection of analytes.

Keywords: Analysis; Food contaminants; Paper; Physical vapour deposition (PVD); Surface-enhanced Raman spectroscopy (SERS);

Resumo

Os contaminantes alimentares consistem em substâncias químicas presentes em produtos alimentares. Como contaminantes alimentares inserem-se por exemplo, os pesticidas, antibióticos e toxinas. Recentemente tem existido uma crescente preocupação na detecção deste tipo de contaminantes não só para prevenção da saúde pública, mas também no meio ambiente.

Os métodos actualmente disponíveis para detecção de substâncias químicas em produtos alimentares são morosos, dispendiosos e complexos de operar. Sendo necessário o desenvolvimento de outros métodos que ultrapassem as desvantagens mencionadas.

Assim, o presente trabalho tinha como objectivo principal explorar a viabilidade da espectroscopia de Raman aumentada pela superfície (SERS) como técnica sensível, robusta, simples e rápida para a detecção de contaminantes alimentares. Deste modo, foram desenvolvidos dois tipos de substratos para aplicação em SERS. Um dos substratos possuía como suporte papel, com poços delimitados por barreiras hidrofóbicas (dois tipos de papel foram estudados, de fotocópia e de cromatografia). Nanopartículas (NPs) de prata, esféricas e em forma de estrela, foram sintetizadas quimicamente e depositadas nos poços por *drop-casting*. Através da sua performance em SERS determinou-se o papel de fotocópia como sendo o mais apropriado, devido à maior retenção de NPs em forma de estrela na sua superfície. Os valores de limite de detecção (LOD) e de quantificação (LOQ) foram 0,17±0,04 e 2,5±0,5 ppb, respectivamente. Este substrato revelou-se reprodutível e estável ao longo do tempo (5 semanas) com desvios-padrão relativo (RSD) de 1,7 % e 7,3 %, respectivamente.

O segundo substrato foi fabricado por deposição física de vapor (PVD) permitindo formar uma camada de NPs de prata esféricas. Os valores de LOD e LOQ foram, 0,015±0,002 e 1,1±0,2 ppb, respectivamente. O estudo de prova-de-conceito foi realizado com malatião e ácido domóico (DA), não tendo sido possível detectar DA. No entanto, os valores de LOD e LOQ para malatião no substrato de SERS em papel foram ~3944 e ~1652 ppm respectivamente, e no substrato de PVD foram, ~925 e ~5644 ppm, respectivamente. Os substratos e respectivo método de produção, revelaram ser sensíveis, robustos e pouco dispendiosos permitindo a rápida detecção de analitos.

Palavras-chave: Análise; Contaminantes alimentares; Deposição física de vapor (PVD); Espectroscopia de Raman aumentada pela superfície (SERS); Papel.

Contents

Index of Figures

Chapter 1. Introduction

Chapter 2. Materials and Methods

Chapter 3. Characterization Techniques

Chapter 4. Presentation and Discussion of Results

Appendix

Index of Tables

Chapter 1. Introduction

Chapter 2. Materials and Methods

Chapter 3. Characterization Techniques

Chapter 4. Presentation and Discussion of Results

Abbreviations

AChE	Acetylcholinesterase
AEF	Analytical enhancement factor
$AgNO_3$	Silver nitrate
AgNPs	Citrate capped-spherical silver nanoparticles
AgNSs	Silver nanostars
$Al_2Si_2O_5(OH)_4$	Hydrated silicate aluminium
ASP	Amnesic shellfish poisoning
$CaCO_3$	Calcium carbonate
cAMP	Cyclic Adenosine Monophosphate
CCC	Critical coagulation concentration
CCD	Charge-couple device
CE	Chemical enhancement
CIPAC	Collaborative international pesticides analytical council
Cl^-	Chloride anion
DA	Domoic acid
DCDR	Drop coating deposition Raman
DLVO	Derjaquian, Landau, Verwery, Overbeek
DNT	Dinitrotoluene
DT	Decanethiol
EBL	Electron beam lithography
EDS	Energy dispersive X-ray spectroscopy
EF	Enhancement factor
ELISA	Enzyme-linked immunosorbent assay
EM	Electromagnetic enhancement
EPA	Environmental Protection Agency
EU	European Union
FDA	Food and Drugs Administration
$FeCl_2$	Iron chloride
FIB	Focused ion beam
FON	Film over nanospheres
GC-FID	Gas chromatography with flame ionisation detection
H_2O_2	Hydrogen peroxide
H_2O	Water
HA	Neutral hydroxylamine
HAB	Harmful algal bloom
HCl	Hydrochloric acid
HPLC	High performance liquid chromatography
IR	Infrared
LC/GC.MS	Liquid or gas chromatography - mass spectrometry
LOD	Limit of detection
LOQ	Limit of quantification
LSPR	Localized surface plasmon resonance
min	Minute
MRL	Maximum residue limit

MW	Molecular weight
NaCl	Sodium chloride
NaOH	Sodium hydroxide
NIBR	National Institute for Biological Resources
NMDA	N-methyl-D-aspartate
NP	Nanoparticle
NSL	Nanosphere lithography
NSP	Neurologic shellfish poisoning
OP	Organophosphate
POC	Point-of-care
PSP	Paralytic shellfish poisoning
PVD	Physical vapour deposition
R6G	Rhodamine 6G
ROS	Reactive oxygen species
SC	Sodium citrate
SEM	Scanning electron microscopy
SERS	Surface-enhanced Raman spectroscopy
SERRS	Surface-enhanced resonance Raman spectroscopy
SM-SERS	Single molecule observation in SERS
STX	Saxitoxin
TA	Tanic acid
TaO	Tantalum oxide
TEM	Transmission electron microscopy
TERS	Tips enhancement Raman spectroscopy
UV/UV-Vis	Ultraviolet/Ultraviolet-Visible

Symbols

A	Absorbance
Al	Aluminium
Ag	Silver
Au	Gold
b	Path length of light
c	Molar concentration
C	Carbon
Ca	Calcium
cm	Centimetres
d	Diameter
E	Energy
Ɛ	Extinct coefficient
$Ɛ(M^{-1}cm^{-1})$	Molar extinction coefficient value
E_{inc}	Incident electric field strength
E_{loc}	Local electric field
g	Grams
h	Hour
Ir	Iridium
I_{SERS}	SERS intensity
KeV	Kilo-electron-Volt
M	Molar
mbar	Milibar
min	Minute
mL	Militers
mM	Milimolar
nm	Nanometres
nM	Nanomolar
O	Oxygen
°C	Celsius degrees
Si	Silicon
s	Second
$\omega_{inc} - \omega_{vib}$	Stokes Raman shifted radiation
ω_{inc}	Incident radiation
µL	Microliter

Chapter 1. Introduction

1.1 Surface-enhanced Raman Spectroscopy for the chemical analysis of food

Recent food safety incidents of chemical residues in food have driven an increasing attention about food safety and human health protection. These concerns led toward the development of methods to detect those food hazards.[1]

The detection of food contaminants (*e.g.* toxins and pesticides) in real-food matrices usually involve analysis methods that may be generally divided into:

1. Biological techniques (*i.e.* bioassays and immunological);
2. Analytical methods (*i.e.* high performance liquid chromatography, HPLC).

Biological techniques such as bioassays require the use of expensive reagents, are laborious (requires a large number of cells/animals to obtain statistical significance) and, time and sample consuming making them impractical for on-site applications.[2] Moreover, these methods have poor repeatability and the animal welfare concerns have encouraged researchers to search for alternative methods of detection.[3] As a possible alternative to the mouse bioassay, the immunological analysis provides high sensitivity inherent to the affinity interactions accomplished between antibodies-antigens (*e.g.* Enzyme-linked immunosorbent assay, ELISA). Although ELISA allow robustness and rapid results without requiring sophisticated equipment nor skilled personnel, it is not easy to detect several types of toxins within the same group or derivative-pesticides. In spite of all these efforts, a need still remains in terms of fast, on-site quantitative analysis procedure for food contaminants.[3–5]

Analytical techniques include chromatographic techniques, such as, HPLC, liquid or gas chromatography-mass spectrometry (LC/GC-MS) and others couple techniques. These methods allow high sensitive detection and quantification limits below the levels concern in food and strong specificity. GC and HPLC are the gold standard analytical tools that are extensively used in food analysis. Nevertheless, these well-established methods are known as non-environmentally friendly methodologies requiring expensive equipment, expert technicians, laboratory-based processing, and the lack of suitability for large-scale screening.[3,6]

Seafood and crops in general have to be marketed promptly after harvesting and the tests results should be available before the shellfish and fruit are sold to public. The several limitations in detecting and properly response, only emphasize the importance of implementing innovative and reliable detection methods. Consequently, the detection tests are not routinely performed on these products sold to market.

An alternative promising technique in chemical quantitative detection is the surface-enhanced Raman spectroscopy (SERS). This methodology has been recently applied in food analysis due the need for a rapid sensitive tool for the detection of food contaminants. The potential of SERS can be readily seen by a comparison between SERS and HPLC, where SERS achieved a higher sensitivity. Moreover, most used chemical methods for food hazards detection require prior separation from proteins and many other potential interfering substances, which tends to increase the cost and time of analysis.[2,7] Furthermore, although progress is needed to obtain reproducible results, SERS is capable of providing analysis in food matrices. Due to the advantages of the mentioned technique, it will be used in the present work and discussed in more detail.

1.2 Surface-Enhanced Raman Spectroscopy

In the early 20th century two vibrational spectroscopy methods appear, infrared (IR) and Raman. Both techniques developed as rapid and nondestructive tools in material identification. IR spectroscopy is based on vibrational transitions induced by absorption of light in the IR spectral region. Raman spectroscopy consists in the scattering of photons by molecules rather than on the absorption of photons. More precisely, in an inelastic scattering of a photon from a molecule in which the frequency changes precisely matching the difference in vibrational energy levels (Figure 1. 1).[8]

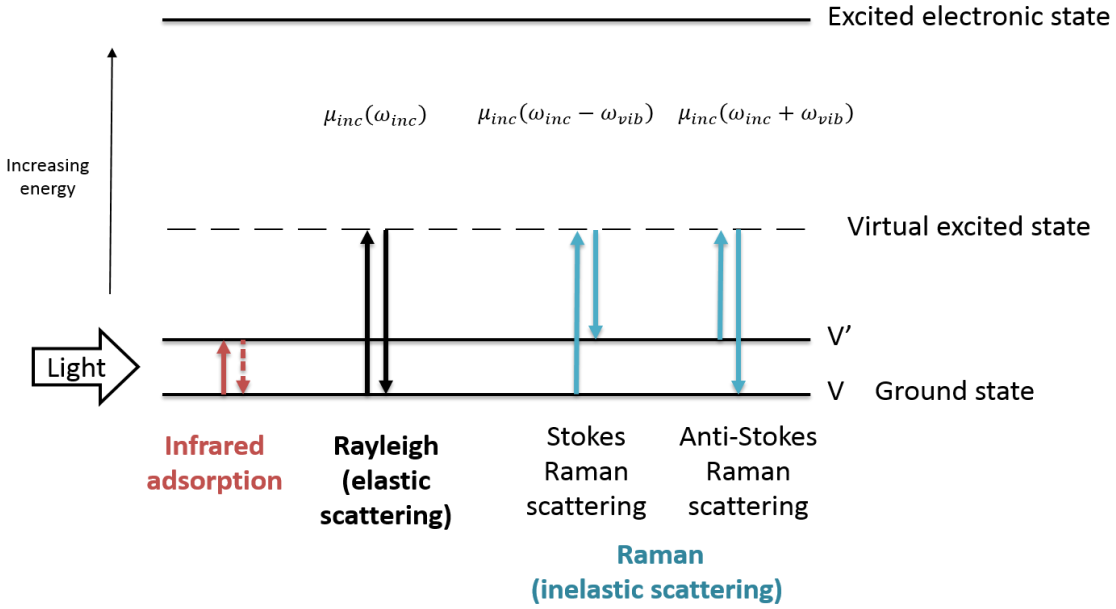

Figure 1. 1|Energy diagram representing the (*from left to right*) IR absorption, elastic Rayleigh scattering and the inelastic anti-Stokes (*left*) and Stokes (*right*) Raman scattering with ω_{inc} , $\omega_{inc} \pm \omega_{vib}$ and ω_{vib} reffering to the frequencies of the incident light, the Raman scattered light, and the molecular vibration, respectively (*adapted from*[8,9]).

Raman spectroscopy has less interference from water[10] making it a great approach for biological molecules. However, it yields very weak signals, where only 1 in 10^6–10^{10} photons will be inelastically scattered at frequencies related to the vibrational energies within the analyte molecule.[11] Hence, Raman allows a sensitive qualitative or quasi-quantitative analysis and the structural characterization for trace analyte.[12] Also, Raman spectroscopy has fluorescence interference, and the high cost of equipment makes it less widely used.[1]

The disadvantageous aforementioned were surpassed by the phenomenon of SERS first reported in 1974 by Fleischmann *et al.*.[10] This event was observed in a pyridine adsorbed on a roughened silver (Ag) electrode. The increase in the Raman cross-section of the molecule, was due to an electromagnetic environment in electrochemically roughened surfaces, and not caused by higher surface area for the pyridine adsorb.[13,14] Afterwards, in 1997 the single molecule observation in SERS (SM-SERS) owed to the demonstration of a strong signal of Raman scattering was the most prominence event.[15,16]

The SERS phenomenon consist in a surface-selective effect in which the scattering of molecules near metal nanostructures generate high local electric fields that are responsible for the extensively increased signal strength observed in SERS, presenting an advantage to the normal Raman scattering.[9]

The current models elucidative of the observed signals enhancements in SERS are based on the interactions between light and metal nanostructures, and, metal nanostructures with molecules, known as the electromagnetic (EM) and the chemical (CE) enhancement, respectively (sections 1.2.1 and 1.2.2).

1.2.1 Electromagnetic enhancement effect

The interaction between light and metal nanostructures involves a resonant elastic light scattering of a metal nanostructure leading to an increased local electric field in the vicinity of the metal particle. In more detail, the electromagnetic wave, at a certain angular frequency, excite resonantly the delocalized conduction electrons in a metal - named *plasmas oscillations*. These *plasmons*, are considered a quasiparticle in which the dielectric functions of the metal and the surrounding medium are among the parameters that influences the resonance frequency. Resonant excitation leads to a charge separation or, in other words, to a dipolar localized surface plasmon resonance (LSPR) (Figure 1. 2). The polarizability of the metal sphere and the incident electric field strength can determine the magnitude of the induced dipole, altering periodically the sign in congruence with the angular frequency of the incoming electromagnetic wave. Consequently, the nanostructure can emit radiation at the same frequency, acting as an antenna.[9]

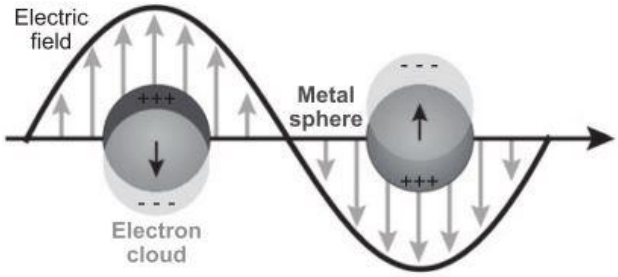

Figure 1. 2|Illustration of the LSPR effect. LSPR consists in a collective oscillation of conduction electrons in a coinage metal nanoparticle (NP) which is in resonance with the frequency of incident light.[9,17]

1.2.2 Chemical Enhancement

CE originates from the direct interaction between the adsorbed molecule and the metal surface, resulting in a charger transfer. It is attributed to the increase in the probability of a Raman transition when the local electric field at the surface of the metal sphere leads to a dipole in the molecule near this surface. The vibrating molecule with angular eigenfrequency has Rayleigh, Stokes and anti-Stokes Raman scattering as dipole components. This mechanism is limited to the first layer of adsorbed molecules due to the required direct adsorbate-surface interaction, therefore the smaller enhancement compared to the EM.[18]

The frequency-shifted radiation at Stokes Raman scattering in the molecule can excite a LSPR of the metal colloid and, in turn, the metal sphere emits radiation by elastic light scattering. To occur the SERS enhancements, the incoming radiation at ω_{inc} and the Stokes Raman shifted radiation at $\omega_{inc} - \omega_{vib}$, have to be in resonance with the plasmon peak of the metal nanostructure.[9]

In short, SERS intensity (I_{SERS}) depends in the incident ($E_{inc}(\omega_{inc})$), and in the outgoing field ($E(\omega_{inc} - \omega_{vib})$):

$$I_{SERS} = I_{inc}(\omega_{inc})I(\omega_{inc} - \omega_{vib}) = |E_{inc}(\omega_{inc})|^2 |E(\omega_{inc} - \omega_{vib})|^2 \approx |E|^4 \quad \textit{(Equation 1.1)}$$

Further, a parameter of utmost importance is that SERS also allows detecting the orientation of the molecule and leads to an elucidation of interaction between the metal and the adsorbate. Distinct SERS signals such as appearance of new bands and shifts, are raised when the molecule is flat, at an angle, or perpendicular orientations due to different enhanced vibrational modes.[9]

1.2.3 SERS enhancement Factor and hot spots

The increased signal strength observed in SERS comparative to normal Raman scattering is a consequence of high local electric fields.

SERS enhancement factor (EF) is used to quantifying the overall signal enhancement by comparing two signals: (1) average SERS signal for the adsorbed molecule on metal surface; (2) normal Raman signal of the same molecule but in solution. The two signals are normalized to the corresponding number of molecules on the surface (1) and in solution (2).[19]

It was verified that when the nanogap between two particles is decreased in a strict control, the SERS signal increases, and it can be observed extremely strong EFs (>10^9) enabling the detection of trace analytes. Hence, SERS is a highly distance-dependent phenomenon, and these intensely localized regions, named *hot spots* can occur not only in the gap of two spheres, but also at sharps and tips (which led to the development of TERS) (Figure 1. 3). However, besides the geometric form of the particles, the probability of finding a molecule in a *hot spot* is very diminutive being more likely to detect a molecule experiencing moderate enhancements (≈10^3) on the surface of one particle. When N spheres are surrounding a single central sphere, the number of *hot spots* is linear with the total number of spheres (*i.e.* N+1).[9]

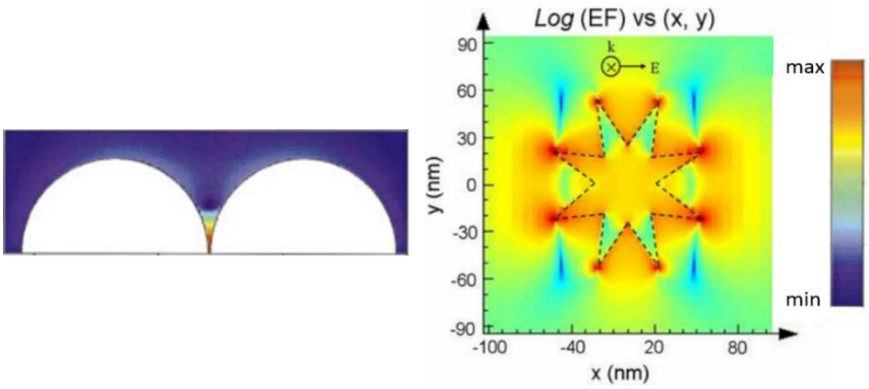

Figure 1. 3|The EM enhancement for dimer configurations of two spheres with a separation of 1 nm (*from the left*). octagonal star (*from the right*). The colour scale from dark blue to dark red is logarithmic (*adopted from*[20,21]).

Notwithstanding the molecules between *hot spots* experiences the highest enhancements, the molecules at colder sites also contribute to the overall signal. Through plasma etching it was possible to isolate the SERS signal contribution arising from molecules located in an individual *hot spot* from the ones that are not. The EF value could then be estimate with accuracy. Consequently, a slight reduction in SERS intensity was observed. Thus, the major contribution to the overall SERS signal emerges from the molecules located in the *hot spots*. Fang and colleagues estimated that 61% of 1 million molecules at sites with moderate EF contribute to 4% to the overall SERS intensity, while 63 molecules of the total at *hot spots* leads to 24% of SERS signal.[9]

The SERS signal also show polarization dependency, being much more intense when the laser polarization is aligned parallel to the dimer axis. As the laser polarization takes others orientations, the SERS intensity decreases. The minimal intensity is when a perpendicular orientation is established. In this case the molecules in the *hot spots* do not contribute to the overall SERS signal.[9]

1.2.4 SERS substrates: Production methods and features

A SERS substrate consists in a coinage metal surface that has nanoscale features. The fundamental requirement for SERS is a substrate that supports a LSPR able to provide the largest amount of SERS active sites with the greatest enhancement for each site.[9]

A good substrate for SERS on-site application requires the following characteristics[9]:

1. Chemical stability (*e.g.* oxidation and large thermal amplitudes resistance);
2. High and spatially uniform EF;
3. Simple fabrication using equipment and environment-friendly reagents commonly found in laboratories;
4. Reproducibility;
5. Simple integration into analytical systems.
6. Simple transportation to the point of sampling;

These features determine the breadth of substrate application in SERS and ultimately compromise the successful detection of an analyte.

SERS-active surfaces can be fabricated through an overwhelming number of techniques. Electrochemically roughened electrodes, the original substrates for SERS, were simple and exhibited a good performance. Highly variable surface roughness depending on the roughening procedure used, and irreproducibility problems led to abandon these substrates.[17,22,23]

Other methods using nanolithography allowed the development of nanostructures with a fine control over the geometric parameters directly on solid substrates, such as electron beam lithography (EBL) and focused ion beam (FIB).[24] Usually those methods need highly specialized equipment, or require expertise in nanoparticle (NP) synthesis. In general, nanolithography tends to have high SERS enhancement factors and superior uniformity, but they suffer from complexity and are expensive to produce.[22]

Template technique is another example of method that offers nanostructures well-defined size and shape under the assistance of designed patterns with a given morphology (*e.g.* Nanosphere lithography, NSL).[24] Generally, when using templates there are two possibilities, deposition of metal materials on the top of the template or, metal materials depositing on the interspaces of the template, which results in nanocaps (film over nanospheres, FON), and hexagonal arrays. Varying the deposition time, different nanopatterns with different spacing are generated, showing different LSPR intensity, thus tuning the SERS intensity.[22,24–27]

The techniques herein emphasized involve the synthesis of colloidal nanoparticles (NPs) and physical vapour deposition (PVD).

1.2.4.1 Colloidal nanoparticles

The synthesis of noble metal NPs has been a class of SERS substrates fabrication method exhaustively studied. Methods involving colloidal materials are advantageous due to their stability, simple fabrication without specialized equipment and high yield of synthesized NPs. The NPs are formed primarily by the reduction of salt solutions in diameters between 10-200 nm.[22]

The optical properties of NPs are mainly governed by the LSPR in the visible electromagnetic range. LSPR promotes a generation of very high electromagnetic fields at the nanoparticles' surface. The specific frequency of these resonances varies as a function of, the type of metal, the dielectric properties of the surrounding medium as aforementioned, but also, due NPs morphology. The shape of patterns and the size of gaps between particles may influence the interparticle coupling generating enhanced signals. The localization and intensity of such fields can be modulated through the morphology of the NPs providing increased SERS enhancements (Figure 1. 4).[4,22,25]

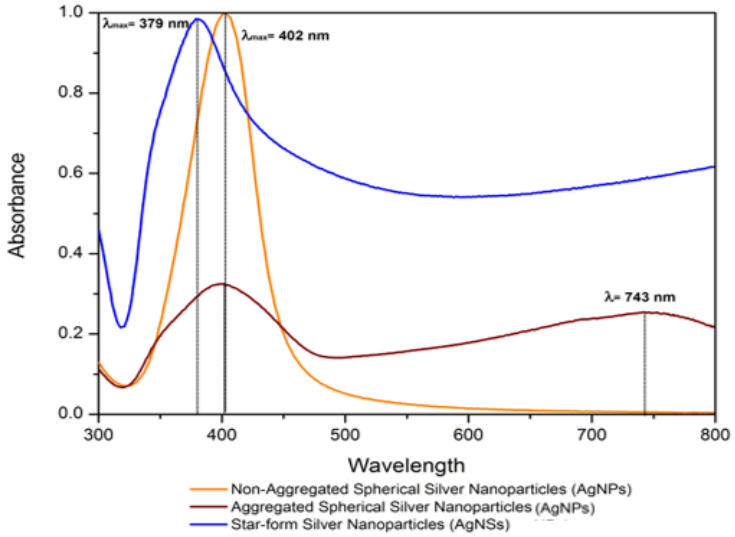

Figure 1. 4|Ultraviolet-Visible (UV-Vis) absorption spectra from non-aggregated and aggregated (*represented in yellow and red colour, respectively*) spherical silver nanoparticles (AgNPs) and star-form silver nanoparticles (AgNSs).

Consequently, a wide range of procedures optimized the production of a wide range of nanostructures varying in size and shape. Controlling the geometry of the NPs is a complex process due to the reaction conditions adjustment to energetically favour the crystal growth in a desired plane. Etchants and surfactants can be added to the reaction, directing growth to a preferred crystal face.[28]

In certain cases, the concentration of the analyte is mixed with the colloid solution. Silver and gold (Au) are the metals most used for SERS, being generally applied as nanospheres highly symmetric and isotropic colloidal particles. Though, they only exhibit moderate EFs and aggregation is sometimes required to increase signal of SERS, cause by the intensification of the field induced in interparticle gaps. The lack of reproducibility associated with aggregation events is the main drawback of the technique. Thus, it is fundamental to develop an approach for controlled synthesis of plasmonic nanostructures maintaining high yield and purity, in a desired crystal plane with increased field enhancements. (Figure 1. 5).[22]

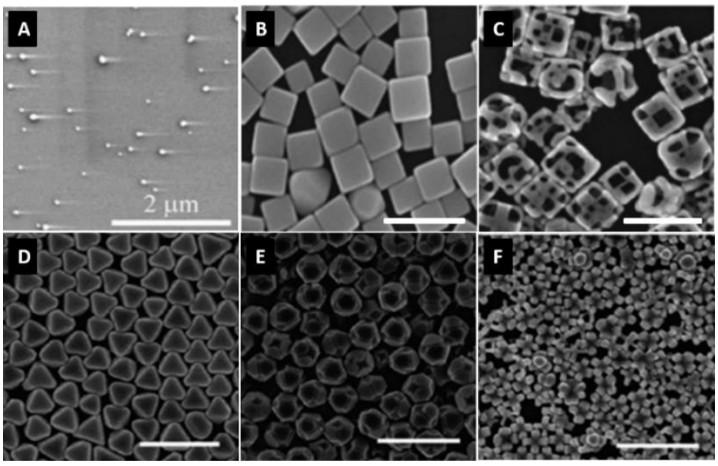

Figure 1. 5|Scanning electron micrographs of NPs with different morphology. Several examples of SERS-active nanostructures: (a) nanospheres; (b) nanocubes (c) etched nanocubes (d) octahedra (e) etched octahedra (f) octapods *(adapted from* [22]*).*

Comparing Ag and Au, Ag is plasmonically more active in visible and near IR regions, and consequently is frequently used in SM-SERS.[9] However, Ag is air sensitive and is not biocompatible, therefore Au is preferred in applications where this features are crucial.[22]

1.2.4.2 Physical vapour deposition

SERS substrates can also be obtained by forming self-assembled metal NPs through physical vapour deposition (PVD). When the evaporated metal at temperatures above 150 °C is deposited in thin layers of metals (~10 nm in case of Ag) on solid supports, it tends to form clusters instead of a flat film.[24]

This technique can offer individual NPs with good control of their size, shape and distance between the particles (Figure 1. 6). These parameters depend on the initial film thickness, the surface tension between materials, annealing atmosphere (vacuum or inert gas), temperature, heating profile and time. Worm-like structures should be avoided, so substrate heating should be performed to favour material surface diffusion during deposition. This method can also be applicable to several supports from solid (glass or crystalline silicon (Si)) to flexible (cardboard packaging or polyethylene) substrates.[24,29] These inexpensive SERS substrates revealed a good homogeneity and stability. A case of success was published by Araújo *et al.* using thermal evaporation assisted by an electron beam to form AgNPs *in situ* during the thermal evaporation of Ag thin films by minimization of the surface tension on cardboard packaging where an 10^6 EF was achieved.[29]

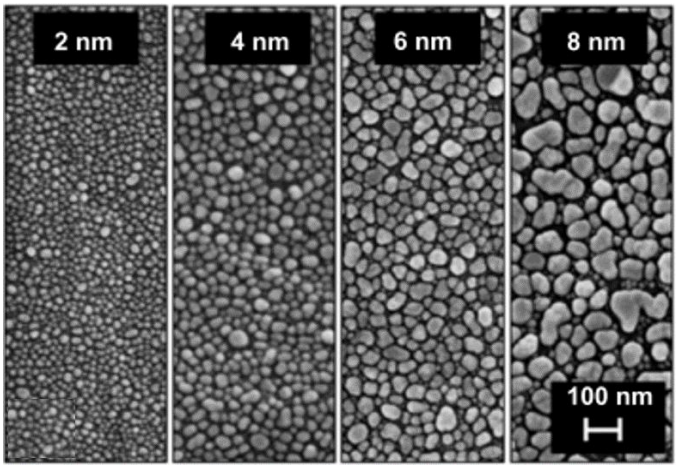

Figure 1. 6|SEM images showing silver nanoparticles (AgNPs) obtained from different Ag mass thicknesses on the surface of cardboard substrates (*adopted from*[29]).

1.2.5 Solid support matrix

The surface onto which the NPs are deposited can vary from glass, Si, polymers and paper. A table with the summary of the principal features is presented in Table 1. 1.

Table 1. 1|Examples of solid support matrix for SERS substrates with associated advantages and disadvantages.[22]

Surfaces	Advantageous	Disadvantageous
Silicon	• Low background within the Raman fingerprint region (only the characteristic peaks associated with the Si crystal vibrations appear).	• Fragile (need to be handled with care); • Rigid; • Si wafers are not easily transported to the point of use without immobilization on another support.
Glass	• Very low SERS background; • Readily integrated into other analytical systems; • Less expensive than Si substrates.	• Fragile; • Rigid.
Paper	• Available; • Inexpensive; • Made of renewable resources; • Flexible (wipe over a surface to collect the analyte);[30] • Hydrophilic (drive the flow of samples without relying on any mechanical components - useful for lateral flow concentration); • Cellulose fibers are compatible with biomolecules (important for biosensing applications).	• Sample spreads out over a large area due the wicking ability of cellulose, so the paper needs to be modified to have vary degrees of hydrophobicity; • Dispersion of the NPs not controlled.

The most common NPs deposition processes include inkjet and screen printing and micropipetting. Paper-based SERS substrates have been developed and are several examples through literature.[26,30–36] The Whatman no.1 paper was chosen due to being the most used substrate in *Lab-on-Paper* technology with applications in several fields such as clinic diagnosis, chemical detection and others.[33,37–39] The office paper was also chosen due a new interesting characteristic for serving as SERS substrate, it has less porosity. Because of the treatments in process fabrication that the paper is submitted, the hydrophilicity of the paper is diminished allowing better ink retaining for writing and printing works.[40]

The *Lab-on-paper* technology consist in the design of hydrophilic wells to support the metal nanostructures in an eco-friendly way generating less printing waste and the solid ink is a non-toxic resin-based polymer being safe to handle.[39]

1.2.6 Surface functionalization

For robust SERS measurements the analyte must be effectively adsorbed on a SERS substrate. Thus, is essential to ensure that a specific analyte adsorbs strongly onto it, and have a high retention time during the measurements. This is especially true for nonresonant molecules, due to Raman scattering cross-section of these molecules being 10^3 times lower than ones form resonant molecules. Therefore, surface functionalization is performed with very thin affinity coatings that are analyte specific onto the surface for SERS detection (*e.g.* thiol-containing molecules).[9,22]

1.2.7 Rhodamine 6G as Raman label

The rhodamine 6G (R6G) has been selected for subsequent investigations in this work because this cationic dye easily yields very large Raman signals. The strong visible absorption of R6G in aqueous solution has a maximum around 530 nm and a vibronic shoulder around 470 nm (Figure 1. 7).[41] When a R6G-NP system is excited with visible light at 532 nm, it leads to the large enhancements observed due to a combination of the SERS effect that originates from surface plasmon excitation, and to a molecular resonance Raman effect (often referred to as surface-enhanced resonance Raman scattering - SERRS). These enhancement mechanisms give a large effective cross-section and result in a strong SERS signal. However, it can generate a high fluorescence yield of R6G which would prevent observation of the Raman spectrum.[42,43]

Although the R6G signal is higher when the excitation wavelength is resonant with the absorption band of R6G, still represents an excellent model analyte due to a large preresonant Raman cross-section of R6G (10^{-26} cm^2 at 633 nm) while avoiding fluorescence. Furthermore, this dye requires no further modification to allow good absorption to the negatively charged colloid Ag surface.[19,44]

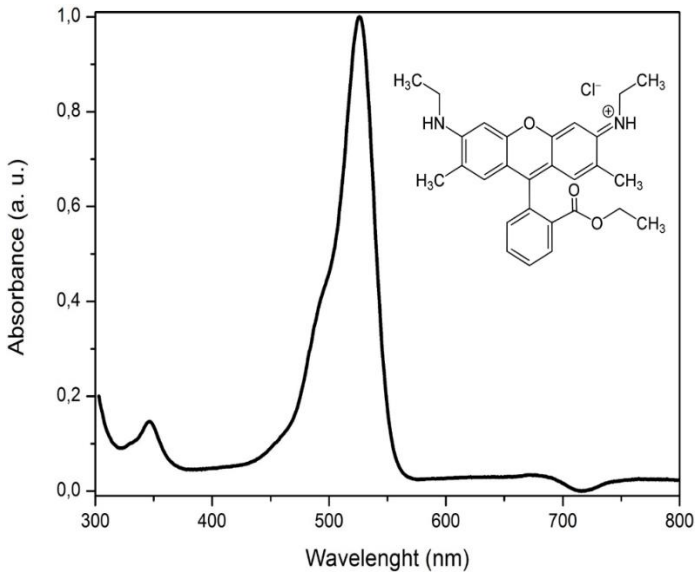

Figure 1. 7|UV-Vis absorption spectrum of R6G with its molecular structure in the inset. The strong absorption of R6G in aqueous solution has a maximum around 530 nm and a vibronic shoulder around 470 nm. The molecular structure was *adapted from*[45].

1.3 Chemical contaminants in food

Chemical contaminants in food are mainly agricultural and environmental chemicals that may exist as food components, such as toxins, pesticides, antibiotics and illegal food colorants.[1] The two examples of food contaminants herein discussed are phycotoxins and organophosphate pesticides.

1.3.1 Shellfish Toxins as food contaminants

Phycotoxins are non-proteinaceous toxic compounds of low molecular weight produced by several species of dinoflagellates, diatoms (*i.e.* marine microalgae) and cyanobacteria. These toxins are able to enter into the food chain as components of phytoplankton.[46,47] These phycotoxins are ingested by shellfish and are accumulated in their digestive glands without causing any poisonous effect.[48] Instead, shellfish act as vectors, transmitting the toxins to humans in an unsafe manner of food consumption.

The overabundance of toxin-producing algae result in most of pathological episodes and are termed as harmful algal blooms (HABs), or more commonly, "red tides".[49] They occur globally, but their incidence is usually sudden and unpredictable.[3,50] Consequently, shellfish toxins are held responsible for approximately 60 000 yearly human intoxications, threatening marine living resources of coastal communities by exclusion from the market place.[51]

Today, seven different types of poisoning have been identified and named according to different symptoms manifestation.[3] The different intoxication symptoms arise from several molecular mechanisms of action due to the wide variety of chemical structures and physical properties. Additionally, shellfish toxins are generally heat resistant – not being remove or degraded during culinary treatment. Furthermore, these are also resistant to the acidic content of the stomach after injection.[3,50,51] In Figure 1. 8 are represented the molecular structure of the most characteristic marine toxins known to cause shellfish poisoning.

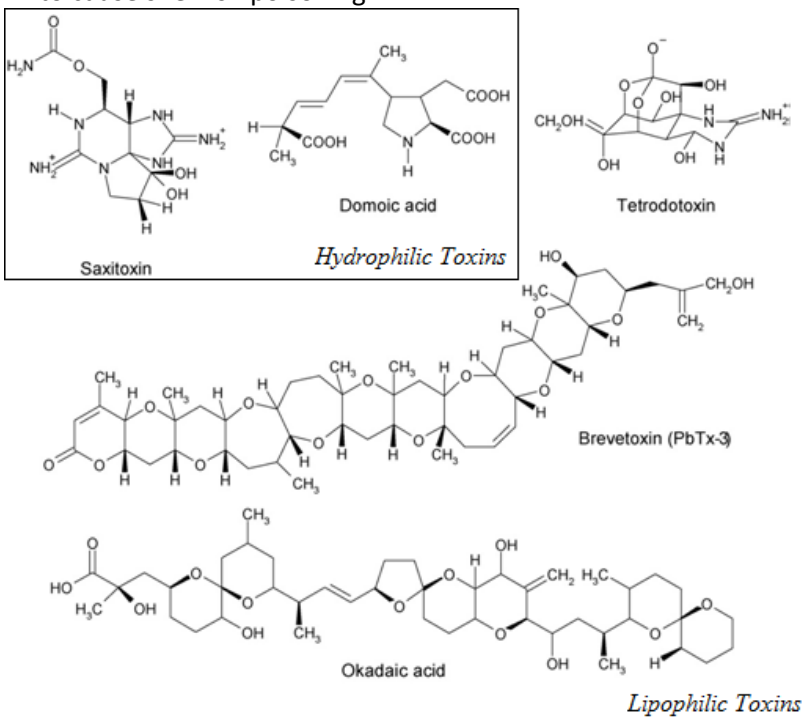

Figure 1. 8|Chemical structure of the most characteristic shellfish toxins. Marine shellfish toxins can be divided in two different classes: hydrophilic and lipophilic toxins. Toxins associated with the syndromes amnesic shellfish poisoning (ASP) and paralytic shellfish poisoning (PSP) are hydrophilic and have a molecular weight (MW) below 500 Da. Toxins responsible for neurologic shellfish poisoning (NSP), diarrhetic shellfish poisoning (DSP), have a MW above 600 Da. These toxins are generally called lipophilic marine toxins *(adapted from[3]).*

In Portugal there is evidence of several shellfish poisonings, and is one of many countries that have taken action to monitor and assess phycotoxins risks in shellfish.[3] Likewise to many other regulatory agencies worldwide, Portugal has established a biotoxin monitoring program named National Institute for Biological Resources (NIBR) since 1997.[52] Similar active phycotoxins monitoring programs throughout the world allowed a decrease in shellfish toxins episodes on humans.

The European Union (EU) regulations established the maximum concentrations to consumption complemented by the main features of shellfish poisonings (Table 1.2).[53]

Table 1. 2|Syndromes of shellfish poisoning principal features with concentration levels allowed in shellfish, define by EU regulations. Toxicity values for DSP and NSP, both concentrations are referred to intraperitoneal administration. List of official detection methods for the most characteristic toxins (*adapted from*[3,53–55]).

Abbreviations: Syndromes: PSP= Paralytic Shellfish Poisoning; ASP= Amnesic Shellfish Poisoning; DSP= Diarrheic Shellfish Poisoning; NSP= Neurologic Shellfish Poisoning; Toxins: STX= Saxitoxin; DA= Domoic Acid; OA= Okadaic Acid; DTX= Dinophysistoxins; BTX= Brevetoxins;

Shellfish Poisoning Syndrome	Toxin Class	Toxin Group	Principal Symptoms	Toxicity to animals (LD_{50})	Maximum levels permitted by regulations	Official Method for toxins detection
PSP	Hydrophilic toxins	STX	• Gastrointestinal distress; • Muscular incoordination; • Respiratory distress	≈6 μg kg^{-1}	80 μg STX/100 g shellfish flesh	*Mouse bioassay* *LC*
ASP		DA	• Gastrointestinal distress; • Dizziness; • Short-term memory loss; • Difficulty in breathing; • Coma, and fatal brain damage.	3.6 mg kg^{-1}	20 mg/kg	*HPLC* *HPLC-UVD*
DSP	Lipophilic toxins	OA	•Diarrhoea; •Nausea; •Abdominal pain.	192–225 μg kg^{-1}	160 μg OA/kg	*Mouse bioassay*
NSP		BTX	•Numbness; •Arrhythmias; •Seizures; •Paralysis and coma	200 μg kg^{-1}	80 μg brevetoxin/100 g shellfish flesh	*Mouse bioassay*

1.3.1.1 Domoic acid as factor for amnesic shellfish poisoning

Domoic acid (DA) is a neuroexcitatory aminoacid produced by marine organisms such as planktonic diatoms (genus *Pseudonitzschia*).[47,52] The first outbreak associated to DA, the causative agent of Amnesic Shellfish Poisoning (ASP), occurred in Prince Edward Island, Canada in 1987.[56] Consumption of contaminated blue mussels (*Mytilus edulis*) resulted 3 deaths and illness of approximately 150 people.[57] Throughout the years several deaths and hundreds of hospitalizations were attributed to ASP.[2,56]

The occurrence of DA in the genus *Pseudonitzschia* has widely distributed incidents from New Zealand to European North Atlantic coast.[3,7,16]

Structurally, DA ($C_{15}H_{21}NO_6$, MW: 311.3303 g.mol^{-1}) is a water-soluble tricarboxylic aminoacid, containing a proline ring and is structurally related to glutamic acid, having a side chain with a conjugated double bond moiety and a hind carboxylic acid (Figure 1. 9).[50,58]

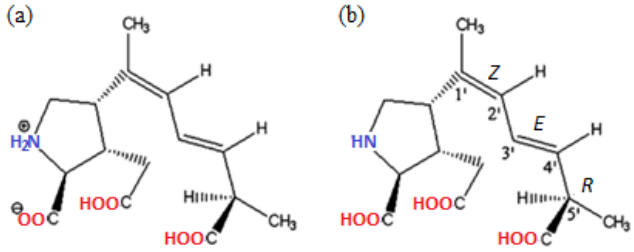

Figure 1. 9|Molecular structure of DA. Crystalline DA in neutral zwitterionic form (a) and DA with stereochemistry in the side chain (b). This toxin is denoted as 1'-Z,3'-E,5'-R(-)-domoic acid due to the double bonds at C-1' and C-3' are Z and E isomers, and this molecule has R-configuration at C-5' centre (*adapted from* [58]).

The structural similarity of DA with the excitatory neurotransmitters glutamic and kainic acids, explains the origin of toxicity from the DA, residing in the geometry of the double bonds. The selective action of DA on glutamic and kainic acid receptors is related to the geometry of the π-electrons in the double bond in the side chain of DA. In fact, the receptor affinity of DA molecules is 3 and 100 fold higher than glutamic and kainic acids, respectively. Consequently, DA binds predominately to N-methyl-D-aspartate (NMDA) receptors, triggering the depolarization of neurons which increases the intracellular Ca^{2+} concentration (Figure 1. 10). The results are a continuous activation of calcium sensitive enzymes, neuronal swelling and finally, cell death. The affected neurons from this interaction are mainly located in the hippocampus, areas responsible for learning and memory processing, hence the name of ASP.[52]

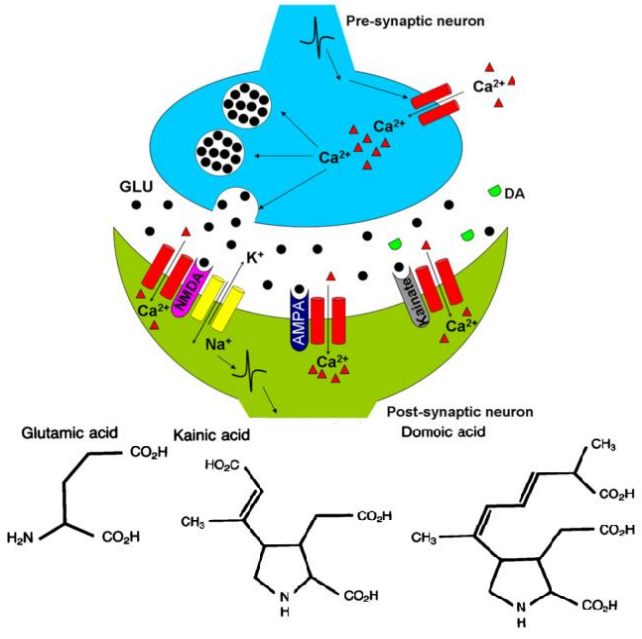

Figure 1. 10|Molecular mechanism of action from DA. DA can act as an excitatory neurotransmitter binding to the same specific receptors of glutamic and kainic acid (*at the top*). The molecular structure of the evolved molecules are represented *at the bottom* (*adopted from* [52]).

1.3.2 Pesticides as food contaminants

Modern agriculture depends on pesticides in order to protect crops and to produce enough quantity and quality of food demanded by today's society. A pesticide is a substance or mixture intended to kill or control any undesired pest including insects, weeds, rodents, fungi, among others.[59] Due to their potential toxicity to humans, animals, and the environment, the regulatory agencies have set tolerance levels in several food products.

Most chemical pesticides are grouped based on their chemical structures, for example, organochlorines and organophosphates. One of the most common used pesticides are the organophosphates (*e.g.* malathion).[57]

1.3.2.1 Malathion

Malathion, *i.e.* diethyl (dimethoxy thiophosphorylthio) succinate ($C_{10}H_{19}O_6PS_2$, MW: 330.358 g/mol), is a wide-spectrum organophosphate (OPs) insecticide (Figure 1. 11). This insecticide was developed in 1950 and is nowadays widely used domestic and agriculturally, being one of the largest selling products for eradication and control of pests.[60–62]

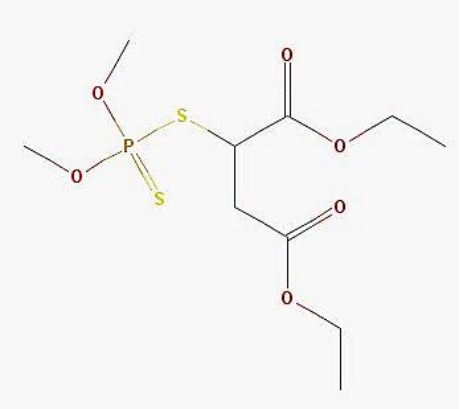

Figure 1. 11|Molecular Structure of malathion (*adopted from*[63]).

Because of its widespread use, excessive concentrations of malathion and malathion-breakdown products, pose a threat to human and animal health through residual contamination of food consisting on a critical concern to the food industry. However, the exposition can also occur in the workplace or home environments. Furthermore, the Environmental Protection Agency (EPA) classified this pesticide as a putative carcinogenic agent. The Food and Drug Administration (FDA) has set the maximum residue limit (MRL) of this pesticide at 8 $mg.L^{-1}$ in food. However, there are nations exporting foods while ignoring the safety regulations, as farmers use pesticides at illegal concentrations with surprisingly high rates of adjacent-field contamination.[64]

The current analysis methods for determining the residual pesticides in fresh fruits are based on chemical analysis and Collaborative International Pesticides Analytical Council (CIPAC) recommended gas chromatography with flame ionisation detection (GC–FID) for the determination of malathion in pesticide formulations.[59]

The mechanisms of action of malathion have not been fully elucidated. However, works have been postulated where it has an inhibitory effect over acetylcholinesterase (AChE) activity in the target tissues. The AChE enzyme hydrolyses acetylcholine after its release by the presynaptic terminal. Acetylcholine is concentrated in synaptic vesicles and, upon terminal depolarization, synaptic vesicles fuse with the plasma membrane and release acetylcholine into the cleft. Then, acetylcholine molecules interact with postsynaptic cholinergic receptors to alter cellular function. When AChE is inhibited by OPs, acetylcholine accumulates in the synapse leading to a persistent stimulation of postsynaptic cells, altering signalling pathways, *e.g.* alteration of intracellular cAMP

levels. Besides this effect, OPs seems to have a role in pancreatic dysfunction by inducing a change in the activity of critical enzymes in metabolic pathways that affect glucose homeostasis. β-cells of the Langerhans islets are essentially vulnerable to oxidative-induced damage and an overload of reactive oxygen species (ROS) that exceeds the capacity of the antioxidant system provokes stress and subsequently can cause diabetes (Figure 1. 12).[60,65]

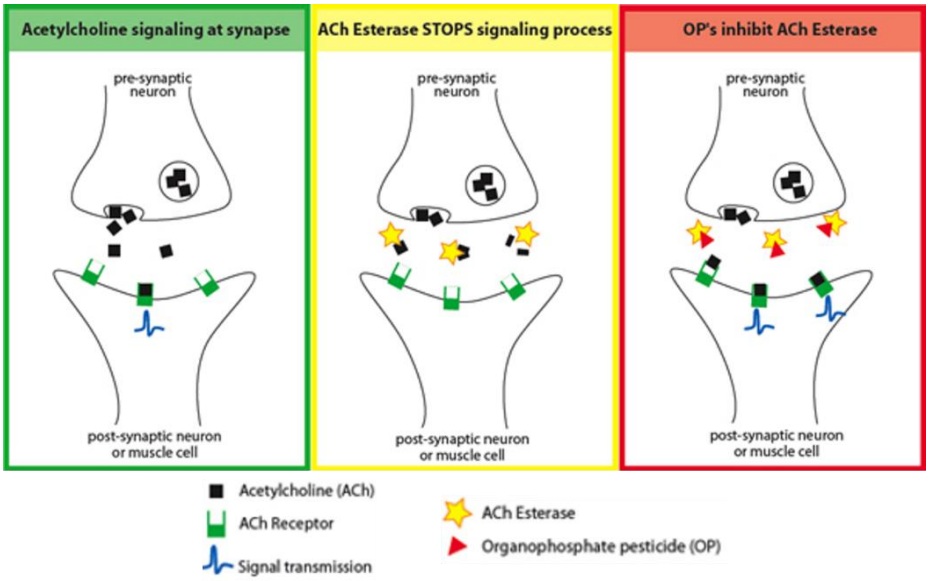

Figure 1. 12|The cholinergic synapse and cholinesterase inhibitors. Normally (*from the left and centre*), AChE efficiently hydrolyses acetylcholine released by the presynaptic terminal. Upon terminal depolarization, synaptic vesicles containing acetylcholine, release the neurotransmitter into the cleft. When sufficient cholinesterase inhibitors bind to AChE (*from the right*), ACh accumulates in the synaptic cleft. This leads to persistent stimulation of cholinergic receptors on the postsynaptic cell (*adopted from*[65,66]).

Common signs of intoxication of cholinesterase inhibitors include seizures and convulsions, hypothermia, excessive stimulation of secretory organs among others. Respiratory failure, paralysis of muscles of ventilation is generally considered the primary cause of death following lethal exposures.[65]

Thus, it is necessary to develop efficient detection methods to monitor and quantify the levels of malathion in different environmental compartments (*e.g.*, surface and ground waters, soil, etc.) and also at distributors and ports of entry.

1.4 Practical applications of SERS

SERS combines the molecular fingerprinting ability inherent to vibrational Raman spectroscopy, with high sensitivity due to plasmon assisted scattering. Since the Raman bands feature narrow spectral widths, the overlap between multiple analytes is minimized and allows for multiplexed biosensing. Other advantage is the rate associated with sample preparation, outrunning other methods.[9,11]

SERS has greatly increased in diversity of applications branching out into detect analyte in very low concentration such as chemical detection[16], reaction dynamics[67], biosensing[68], explosives detection[69,70], and art conservation[71], to name a few of the many striking application areas.

To prove the wide application of SERS, a few examples are following presented.

The detection of explosives is important to homeland security, military issues, and land mine detection. Piorek *et al.* reported a free-surface microfluidic and SERS chemical detection system and 1 ppb of 2,4-dinitrotoluene (2,4-DNT) was successfully real-time monitored.[25,69]

Inducing plasmonic coupling through molecular conformational changes is an interesting idea where stimuli-responsive polymers can exhibit reversible conformational change due to environmental factors (*e.g.* pH).[9]

SERS also play an important role in the life science for health care or therapeutic treatment. It has been widely used for detecting biomolecules, pathogens sensing, cancer diagnosis, and *in vivo* molecular probing in live cells. It has been envisioned SERS in theranostics (combination of diagnostics and therapeutics) through intracellular monitoring of drug effect. Biosensing can present an approach of label-free intrinsic SERS - signal enhancement originates from the compact adjacency of the analyte and the metal surface. Or the metal surface is functionalised with a Raman reporter and target-specific ligands, *i.e.* antibodies - extrinsic SERS labels. The amplified signal from the Raman reporter is obtained upon the recognition of target analyte.[11]

For glucose sensing owing to its connection with *diabetes mellitus*, van Duyne's group established AgFON functionalised with 1-decanethiol (DT). Afterwards, *in vivo* transcutaneous glucose monitoring was achieved by the same authors. DNA/RNA detection using NPs with Raman spectroscopy fingerprints, quantitative and multiplex DNA detection were also reported.[9,11]

1.4.1 Applications of SERS in the Chemical Analysis of Food: DA and malathion

The detection of trace-level hazardous chemicals is also in high demand because of the increasing threat from harmful environments and unreliable food safety.[25] In trace chemical detection most common examples are illicitly sold narcotics[30], food additives[1,72,73], and residual pesticide detection[64,74].

Food safety industry has envied SERS emerging as a tool for detection of food contaminants such as chemical and microbial hazards. However, the number of publications on HPLC and GC is much higher than those of SERS.[1] In addition, pesticide residues have also been detected through SERS in fruit crops and surface and ground waters.

1.4.1.1 DA detection methods based on SERS

To date, there are a few reports on the detection of shellfish toxins using SERS.[4,12,50,75–78]

DA detection was firstly detected by UV Raman with samples prepared by simple homogenization of the clam tissue without any other modification, achieving a limit of detection (LOD) of 0.48 ppm.[7] The ability to quantify DA from several samples without prior extraction or separation steps was a remarkable finding. Djaoued *et al.* reported a drop coating deposition Raman (DCDR) method where a LOD of 0.25 ppm of DA was achieved.[58]

The potential for SERS as marine toxin sensor, was demonstrated for the first time by Olson *et al.* using AgNPs colloid for detecting DA and STX. The SERS spectra displaying enhancements of nearly 70 times over the normal Raman signal. They examine the binding and orientation of DA to a metal surface that indicate an elongation or weaknesses of the bonds. The LOD achieved was 7.8 ppm.[4] The most recent work on DA detection was performed by Muller and colleagues. The authors investigated DA detection using both pure and amino-functionalized AgNPs. Researchers reported the presence of Ag-O assigned to 223 cm^{-1} SERS band. This result was supported by the absence of the C=O mode at 1717 cm^{-1} in the SERS signal. The achieved LOD was of 0.01 ppm in seawater solution, much lower than the admitted level by current regulations.[50] The capability of the DA toxin in seawater could be detected by SERS with highly sensitivity, open possibilities to real-time monitoring allowing to act in point-of-care (POC).

The literature has also reported several other methods in order to detect and quantify others marine toxins.[12,75,76] Pearman and Hall demonstrated that SERS and multivariate statistical analysis can be applied to discriminate in the same family of toxins, the molecule itself.[12,78] This is a significant breakthrough since the qualitative ability of SERS to discriminate different toxins

belonging to the same family is essential to establish SERS as a technique for monitoring shellfish toxins.[77]

To date, any reference paper reporting a mixture analysis on ASP, PSP or DSP based on SERS providing detection results from water is absent in literature.[50]

1.4.1.2 Malathion detection methods based on SERS

Yu and White to illustrate the use of the filter membranes, create a SERS-active surface by trapping and concentrating NPs from a colloid solution. Then, the membranes concentrate the analytes into the immobilized matrix of NPs allowing their detection (61.5 ppb for malathion). The authors found that the measured SERS intensity by filter SERS exhibits low variation relative to traditional SERS techniques.[35]

The same authors also developed an extremely simple and inexpensive, but highly sensitive method of performing SERS. The work was in a paper-based surface swab and lateral-flow dipstick that includes an inkjet-printed SERS substrate for analyte detection. Using lateral-flow paper SERS devices, detection limits as low as 413 pg of malathion were achieved. It is also worthwhile to note that this surface exhibit a high noise hindering the detection of analytes.[30] Nevertheless both SERS substrates provide potential methods to rapidly detect pesticide residues on the fruits and vegetables, which is crucial to diet safety.

Fathi and colleagues investigate the interaction of nanostructured Ag surfaces with OPs by electrochemical methods and SERS. The addition of OPs, results in significant changes in the electrochemical behaviour and the surface morphology of Ag nanostructured surfaces. Consequently, these *in situ* electrochemically fabricated SERS substrate was able to detect malathion as low as 10 pM.[79]

Barahona *et al.* developed a new format of apta-sensing composite particles for SERS detection of malathion. The thiolated aptamer targeting malathion was attached to the metal surface by thiol-gold interaction, resulting in polymer-AuNP-aptamer composite microspheres. The proposed apta-sensing SERS substrate successfully allowed the direct detection of the target molecule at 0.033 ppm.[80]

Recently, the direct detection of malathion in the peels of tomatoes and Damson plums was stablished by couple SERS imaging with multivariate curve resolution methods. This methodology enabled detection on the order of 0.123 ppm, which is below the MRL permitted for this pesticide. The strike evidence is that this technique function without prior knowledge of the analyte spectrum and possible interferences. Thus, it is feasible for other fruits and pesticides as well.[81]

The works herein describe that SERS is advantageous for low resource settings, in particular, for on-site environmental monitoring and food analysis.

In sum, if DA or malathion is to be detected with high sensitivity from food, the detection needs to be very selective. This implies that the multitude of other biochemical components of the algal, shellfish cells and fruit, most not interfere strongly.

Besides the little sample preparation, the lower number of experimental steps, amount of reagents used, time of analysis and the suitably for conducting measurements *in situ*, also large economic benefits can be predicted. Estimates of cost *per* test prowl several hundreds euros and several of work days to perform a chromatography analysis, while the price of SERS analysis was estimated to be 0.21 € for 200 mL colloidal Ag, sufficient for about 400 measurements.[77] Together with nanofabrication approaches, SERS-based methods in monitoring food contaminants are likely to become a powerful analytical tool. The SERS method, has the possibility to automation, and will be relatively inexpensive to apply since the labour involved in testing will be little. Although some successful efforts have been being made, SERS sensing equipment are still in the beginning with the potential underused.[50]

1.5 Work Proposal

In food analysis, HPLC and GC are the gold standard analytical tools. These techniques provide specific, highly sensitive and robust detections. However, these techniques are known to be expensive and time-consuming. Hence, typical tests are not performed routinely on food products for consumption.

Given the short shelf-life of live shellfish or fruit crop, is mandatory that the results are available in a manner timely enough in order to remove the potential threat to public health. Therefore, it would be advantageous for many applications within the food industry to develop simple, rapid, portable, and sensitive method.

SERS combines the molecular specificity of vibrational Raman spectroscopy with high sensitivity due to plasmon assisted scattering provide by a metal nanostructure.

There has been a great development due to the nanofabrication of SERS that increased the availability of suitable nanostructured SERS substrates. Achieving metal nanostructures by lithographic procedures is challenging, given fabrication limitations in the size of interest (10–100 nm). Colloidal chemistry, on the other hand, has demonstrated that specific shapes of AuNPs or AgNPs can be synthesized relatively easily in the laboratory with high SERS-performance and uniformity. Ag was used as metal because is plasmonically more active.

Thermal evaporation assisted by an electron beam can also be used for obtain a SERS substrate by forming self-assembled metal NPs. This process promotes a good homogeneity and stability, and can be simple and inexpensive. The vapour deposition can be applicable to several supports from solid to flexible substrates, such as cardboard packaging.

Paper is a cheap organic material, biocompatible and disposable, what leads to numerous applications. Paper-based SERS has the potential to become a simple, yet highly sensitive detection platform that can rival with traditional trace analysis techniques and compete with recent advancements such as lab-on-a-chip devices.

The main goal of the present work was the development of a SERS substrate able to detect and quantify low concentration levels of DA and malathion in an aqueous environment.

Therefore, two strategies were purpose:

1. Paper SERS substrate: where Whatman no.1 and office paper were used as solid support matrices. Then, aggregated and non-aggregated AgNPs, and AgNSs were *drop-casted* (Figure 1. 13-A).
2. PVD SERS substrate: the solid support matrices were glass, Si and cardboard packaging. Several approaches were attained and are represented in Figure 1. 13-B.

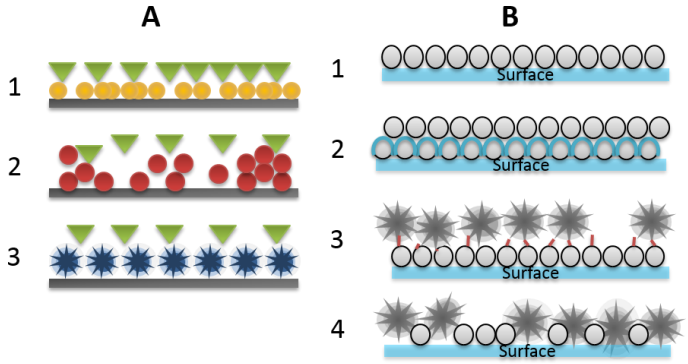

Figure 1. 13|Strategies employed in this work. (A) Paper-SERS substrate: (1) non-aggregated AgNPs; (2) aggregated AgNPs and (3) AgNSs; and (B) PVD SERS substrate: (1) monolayer of AgNPs; (2) double layers of AgNPs; (3) monolayer of AgNPs with AgNSs linked; (4) growing AgNSs onto a monolayer of AgNPs.

The simplicity of obtaining results and ease of mass production can be useful for POC applications and will certainly open up a wide variety of new avenues for research.

Chapter 2. Materials and methods

In this section, an experimental description is made of the synthesis of silver NPs. These silver NPs were used to impregnate the wells producing paper SERS substrates. Additionally, SERS substrates fabricated by PVD and subsequently submitted to physical or chemical modifications were produced. SERS performance for all the paper and PVD SERS substrates was investigated.

2.1 Chemicals, materials and instrumentations

A detail list of all the chemicals, materials and instrumentations and suppliers are presented in Appendix I.

2.1.1 Chemical synthesis of citrate capped spherical silver nanoparticles

The typical procedure for the production of citrate capped spherical silver nanoparticles (AgNPs)[1], was based on the method of Lee and Miesel[82], later optimized by Bastús *et al.* which is given below.[83]

All glassware was rinsed with acetone, followed by Milli-Q water before use. An aqueous solution containing sodium citrate (SC) (5 mM) and tannic acid (TA) (0.1 mM) in 100 mL volume was prepared. The concentration of TA (0.1 mM) was chosen as intended to produce AgNPs with ≈20 nm of diameter. This is a very important factor since TA is responsible for the final AgNPs size and monodispersity. TA in smaller concentrations is responsible for a strong complexation that stabilize intermediate forms of Ag^+ ions narrowing the AgNPs size. A condenser was adapted to the roundbottomed flask to prevent the evaporation of the solvent, and the solution was subjected to heat under reflux using an aluminium plate under vigorously stirring. When the solution began to boil (≈15 min), 1 mL of silver nitrate ($AgNO_3$) was rapidly added to the solution that became bright yellow immediately. The solution was kept under heating and stirring for 5 min and then cooled with ice to finish the reaction. In order to remove the excess of TA from the resultant coated AgNPs, the solution was purified by centrifugation at 12 000 g for 25 min and with a temperature of 4°C, and redispersed in SC (2.2 mM) before sample characterization by UV-Vis absorption spectroscopy. After synthesis, the colloidal solution was stored at 4°C in the dark, until used.[83]

Using the Bastús *et al.* method, the final colloidal solution of AgNPs presents a LSPR band centred at approximately 400 nm.

2.1.2 Chemical synthesis of citrate capped star-shaped silver nanoparticles

A reproducible chemical synthesis method for citrate capped star-shaped silver nanoparticles, or silver nanostars (AgNSs) was recently reported by Garcia-Leis *et al*..[84] This work was seminal in the chemical synthesis of anisotropic NPs intended for SERS application. In fact, for the first time, it does not use strong surfactants and other compounds that remain adsorbed on the surface of the synthesized anisotropic NPs, limiting the access of analytes to the NP surface and hence, their applications on SERS-based detection methods.

Colloidal suspensions of AgNSs were prepared by chemical reduction of Ag^+ in two steps: in a first stage using as reducing agent neutral hydroxylamine (HA) in aqueous solution to induce the

[1] From this section, for simpler purposes the citrate capped, spherical and star-form, silver nanoparticles (AgNPs and AgNSs, respectively), as well as aggregated AgNPs are going to be named as NPs when referring the three of them.

growth of spiked NPs; and SC in a second step which accelerates and completes the reduction process.

A solution containing 2.5 mL of HA ($60x10^{-2}$ M) and 2.5 mL of NaOH ($50x10^{-2}$ M) was prepared and placed under stirring, followed by the dropwise addition of 45 mL of $AgNO_3$ (10^{-3} M). At this stage there is a colour change of the suspension from transparent to brown. After 2 min, 500 µL of SC (1.5 %) was added to the mixture. The final suspension was stirred for 3 h showing a dark grey colour. The solution was concentrated by centrifugation at 1500 g for 15 min and ressuspended in Milli-Q water. After synthesis, the colloidal solution was stored at 4 °C, in the dark, until use.[84]

This synthesis, size and concentration determination (in *NanoSight*[2]) was performed by Dr Pedro Quaresma from the research group of Professor Eulália Pereira from UCIBIO, REQUIMTE, Faculdade de Ciências da Universidade do Porto, Portugal.

2.2 Fabrication of paper and PVD SERS substrates

Throughout this study several SERS substrates were fabricated that can be divided into two major groups: (1) paper substrates impregnated with NPs; and (2) produced by the PVD technique on a glass, Si or cardboard packaging (*e.g.* "TetraPak") substrate, and that may also have undergone an additional physical or chemical modifications.

2.2.1 Fabrication of paper SERS substrates

The *Lab-on-paper* technology was chosen to construct a surface for SERS substrates because it allows the definition of hydrophilic regions in the paper via patterning with hydrophobic wax.[85] The fabrication process of SERS substrates can be divided in the following main points: (1) Paper surfaces preparation; (2) Patterning of the surface for the SERS substrates and hydrophobic barriers formation; (3) Deposition of NPs in the paper surfaces.

2.2.1.1Paper surfaces preparation

In order to determine the most adequate paper surface for SERS substrates, two types of paper were used: (1) Whatman no.1 paper; (2) officer paper.

The Whatman no.1 paper is acquired in sheets of 460 x 570 mm and then cut into standard A5 dimensions (148 x 210 mm). Office paper was used as acquired in A4 sheets (210 x 297 mm). All papers were stored at room temperature without any additional treatment before use.

2.2.1.2 Patterning of the paper surface for the SERS substrates

The patterning of the paper used in this work had the assistance of vector drawing software - Adobe Illustrator (Adobe Systems Software, Ireland). Wells were drawn with a line width 0.5 mm and 10 mm was set as the interval between them. Patterns were draw with the configuration depicted in Figure 2.1-A and B, whose diameter in A was 5 mm, and in B was 3 mm. The pattern in Figure 2. 1-A was printed in the two types of paper and B was only in office paper.

[2] Consists in a particle-by-particle methodology where each particle is individually and simultaneously analysed by direct observation and measurement of diffusion events. *Nanosight* produces high resolution results for particle size distribution and concentration.

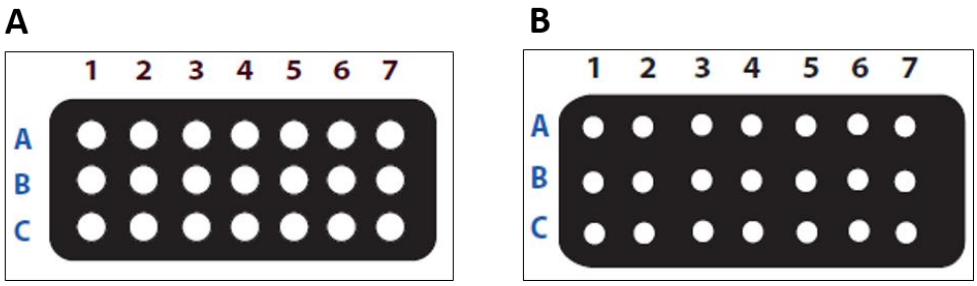

Figure 2. 1|Patterns design in paper. Scheme of several layers to fabricate the paper surface that supports the SERS substrates. Front view of the paper surface with diameters wells of (A) 5 mm and (B) 3 mm.

The wax-printing technology is possible due to solid ink printer. The printer uses solid wax ink cartridges instead of the liquid paint cartridges of conventional printers and it is through diffusion of wax that the previously designed patterns are transferred to the paper's surface (Figure 2. 2).

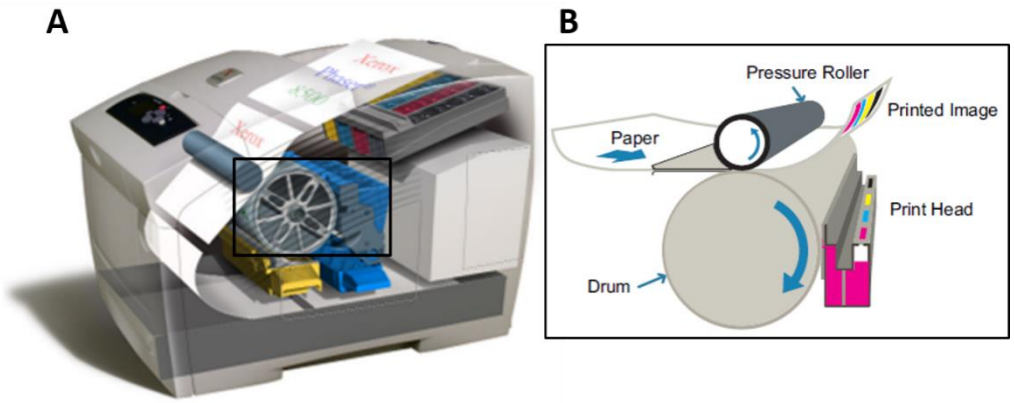

Figure 2. 2|Scheme of the solid ink printer used to produce the hydrophobic barriers to fabricate SERS substrates. (A) Printer's transversal scheme to demonstrate the printer's operation. (B) Inset of the major components of the solid ink printer. The solid wax is melted before being ejected from the print head and solidifies immediately on the paper surface.

After printing, the wax is only at the surface of the paper and to create the hydrophilic wells it was necessary to diffuse vertically the wax through the paper, resulting in hydrophobic barriers (Figure 2. 3). As previously reported, the diffusion was done in a heating plate at 140 °C during 2 min.[39] After this process the paper surfaces were ready to deposit the AgNPs and AgNSs in the wells, forming the paper SERS substrates. The wells diameters after diffusion became 4 and 2 mm, respectively and will be considered throughout this work.

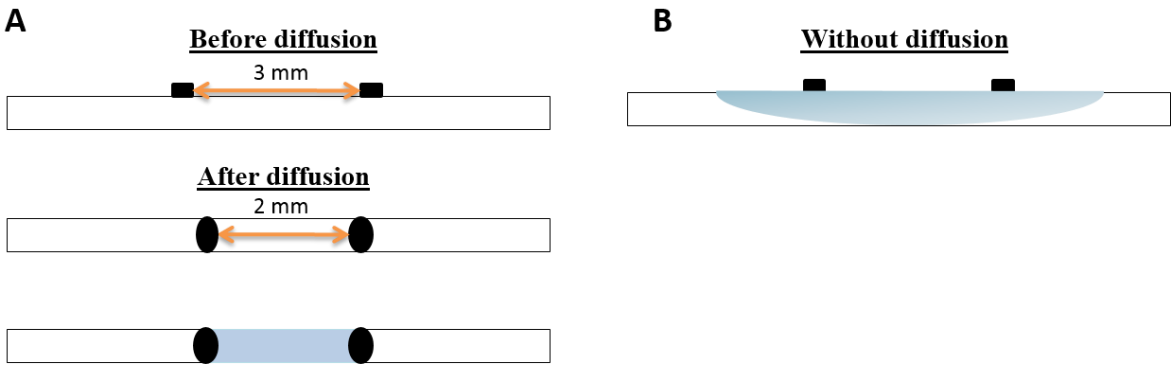

Figure 2. 3|Process diffusion of the wax – producing the hydrophobic barriers. (A) The printing is only at the surface of the paper and to create the wells to hold the NPs, the diffusion as to be promoted by a heating plate. The result is a well with a diameter lower than the original pattern due to diffusion of the wax in all directions ≈0.5 mm (*i.e.*, not only in the thickness of the paper but also laterally) and the liquid (represented in *blue*) is trapped in the well. (B) Without diffusion, the liquid spreads.

2.2.1.3 Deposition of silver nanoparticles in the paper surfaces

After patterning the paper surfaces, NPs were deposited in order to produce a SERS substrate and perform Raman measurements. The method used to deposit was *drop-casting,* consisting in dropping the solution, followed by spontaneous solvent evaporation. When the final volume of colloidal solution to be added was too large to be contained in the well, smaller volumes were added (Table 2. 1). With a heating plate (Agimatic-N, Selecta) at a temperature below the wax melting point (*i.e.*, <80°C), various depositions were made until the final volume was complete in the minimum time required. The volumes added to the paper surfaces are presented in Table 2. 1.

Table 2. 1|Volumes added to each well depending on well diameter.

Pattern	Volume in each deposition (µL)	Final Volume added (µL)
Well diameter of 4 mm	50	100 300 500
Well diameter of 2 mm	10 2.5	62.5

The volume of 62.5 µL in a well with 4 mm corresponds to 500 µL in the well of 2 mm. The colloidal solution of AgNSs was always sonicated before used to allow the resuspension of the colloidal solution. The final paper SERS substrates were stored at 4 °C in a desiccator, wrapped in aluminium foil (Figure 2. 4).

Figure 2. 4|*Drop-casting* method. (A) Silver NPs deposition with the volume of 50 µL in the well. (B) The volume of 100 µL was to demonstrate that the well cannot sustain that volume.

2.2.2 Treatments of the paper SERS substrates

Several steps were carried out to reduce the amount of citrate that coated the NPs. These treatments had the intention of decreasing the SERS signal from the citrate that compromises the SERS spectra correct interpretation. The processes carried out are summarized in Table 2. 2.

Table 2. 2|Summary of the treatments performed on the paper SERS substrates to remove or oxide the citrate, the capping agent of the silver NPs used in this type of substrate.
Abbreviations: $FeCl_2$: iron chloride; H_2O_2: hydrogen peroxide; HCl: hydrochloric acid.

Treatment	Repetitions	Parameters					Washes (Milli-Q H_2O)	
		Concentration (M)	Volume (µL)	Velocity (rpm)	Time (min)	Temperature (°C)	Volume (µL)	Time (min)
Centrifugation	3	-	1000	1500	5	4	-	
Basic H_2O*	1	-	10	-	5	room	-	-
Basic H_2O*	2	-	10	-	5	room	-	-
$FeCl_2$*	1	$1x10^{-2}$	10	-	overnight	room	10	5
$FeCl_2$*	1	$1x10^{-3}$	10	-	overnight	room	10	5
H_2O_2*	1	3 %	10	-	overnight	room	10	5
H_2O_2*	1	$1x10^{-1}$	10	-	overnight	room	10	5
H_2O_2 + $FeCl_2$*	1	$1x10^{-1}$+ $1x10^{-3}$	10	-	overnight	room	10	5
HCl*	2	2	10	-	10	room	-	-

Treatments highlighted with * were executed by Dr. Pedro Quaresma from the research group of Professor Eulália Pereira from UCIBIO, REQUIMTE, Faculdade de Ciências da Universidade do Porto, Portugal.

2.2.3 Fabrication of SERS substrates by physical vapour deposition

Ag films were deposited on three types of surfaces: (1) crystalline Si; (2) glass; (3) cardboard packaging substrate; (2.5×2.5 cm^2) by e-beam evaporation at a surface temperature of 150 °C. The deposition was carried out with a working pressure of 10^{-5} mbar and a deposition rate of 0.07 nms^{-1}. The layer thickness was controlled by a calibrated quartz crystal detector.[29] The Ag mass film thicknesses could be 4 or 6 nm resulting in a monodispersed layer of spherical AgNPs[3] with 40 or 60 nm respectively. For the remainder of this paper these surfaces with a monolayer of AgNPs deposited will be referred to as the PVD SERS substrates.

Other assays were made to allow double layers of spherical silver nanoparticles deposited that could be separated or not by a thin layer of tantalum oxide (TaO). The thickness of the dielectric layers ranged from 0-12 nm.

This fabrication of PVD SERS substrates was performed by the Master Andreia Araújo under orientation of Professor Hugo Águas from CENIMAT|iN3 (Centro de Investigação de Materiais, Faculdade de Ciências e Tecnologia da Universidade do Nova de Lisboa FCT/UNL, Portugal).

2.2.3.1 Star-form silver nanoparticles on the PVD SERS substrate

Others approaches were attained to improve the SERS performance of the aforementioned PVD SERS substrates defined by adding AgNSs[3] by two distinct strategies (Figure 2. 5):

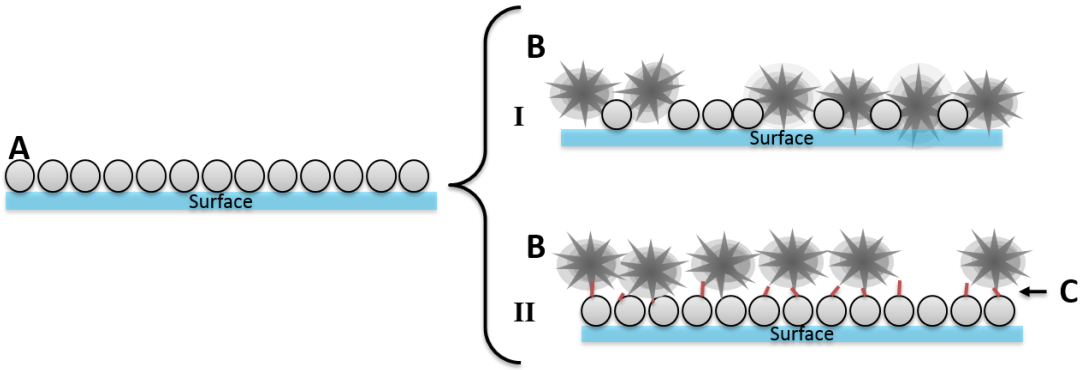

Figure 2. 5|AgNSs on the PVD SERS substrate. (A) NPs fabricated by the PVD method. (B) AgNSs that can be chemically synthesized or chemically grown as describe in the sections 2.1.2 and 2.2.3.2, respectively; Two different strategies were employed to add chemically synthesized AgNSs to the PVD SERS substrate: (I) use the PVD AgNPs as seeds for the growth of AgNSs; (II) linkage of AgNSs to the original PVD SERS substrates; and (C) linker.

Both AgNSs deposition strategies on the original PVD SERS substrate, were executed by Dr. Pedro Quaresma from the research group of Professor Eulália Pereira from UCIBIO, REQUIMTE, Faculdade de Ciências da Universidade do Porto, Portugal.

2.2.3.2 Growth of star-form silver nanoparticles on the PVD SERS substrate

The growth of AgNSs was achieved in the presence of the AgNPs already on the surface promoting their conversion to nanostars by serving as a silver nuclei precursor. The PVD SERS substrate was vertically dipped in a mixture of HA and NaOH followed by $AgNO_3$ addition as describe in section 2.1.2. The mixture was left under stirring for 30 min, and the substrate was left undisturbed for 24 h. Later, the substrate was removed from the reaction solution, washed with Milli-Q water and absolute ethanol. Finally, the substrate was dried in a desiccator. The synthesis conditions evaluated were the concentration of HA and immersion time. The substrates were stored in the dark until

[3] It should be pointed out that the AgNPs and AgNSs produced herein do not have citrate as capping agent.

used. Samples were prepared with varying HA concentrations and different immersion times (Table 2. 3).

Table 2. 3|Samples analysed produced by growing AgNSs onto a monolayer of AgNPs – PVD SERS substrate.

Nomenclature Series	HA		Surface	Thickness of the AgNPs layer
	Concentration (mM)	Immersion Time (min)		
A1	3	120	Si	4
A2	60	120	Si	4
B1	3	10	Si	4
B2	30	10	Si	4
B3	60	10	Si	4

2.2.3.3 Deposition of star-form silver nanoparticles on the PVD SERS substrate

The deposition of AgNSs to the PVD SERS substrates was proceeded by dipping the substrate in an ethanolic solution with the linker (Figure 2.6). The substrate was then washed with absolute ethanol followed by Milli-Q water and immediately dipped in a colloidal dispersion of AgNSs (same synthesis as describe in the section 2.1.2). As in the previous section, the substrates were washed with abundant Milli-Q water, absolute ethanol and dried in a desiccator. The substrates were stored in the dark until used.

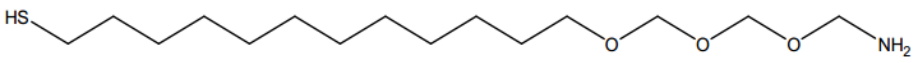

Figure 2. 6|Chemical structures of the functional linker.

Samples were prepared with varying linker and AgNSs concentrations (Table 2. 4).

Table 2. 4|Samples analysed produced by depositing AgNSs onto a monolayer of AgNPs – PVD SERS substrate.

Nomenclature Series	Surface	Thickness of the AgNPs layer	Linker		AgNSs	
			Concentration (µM)	Immersion Time (min)	Concentration (nM)	Immersion Time (min)
A	Si	6	1	30	0.1	30
	Si	6	10	30	0.1	30
B	Si	6	1	30	0.4	30
	Si	6	10	30	0.4	30
C	Cardboard	6	1	30	0.4	30
	Cardboard	6	10	30	0.4	30

2.3 Preparation of samples for SERS measurements

The samples are prepared in aqueous solution and then applied over the surface of the silver NPs.

2.3.1 Rhodamine 6G

R6G was employed as a non-resonant analyte (at 632.8 nm wavelength excitation) to evaluate SERS activity in the substrates. This molecule has been applied in SERS analysis, due to its extremely elevated Raman cross-section.[30,86,87] SERS substrates were prepared by dropping 2 µL of R6G solution. Concentrations of the R6G solution were from 10^{-3} to 10^{-12} M and a 10^{-3} M R6G solution was used in glass as the reference control. The R6G solution concentration scheme represented in Figure 2. 7 was applied in the assays of the paper SERS substrates.

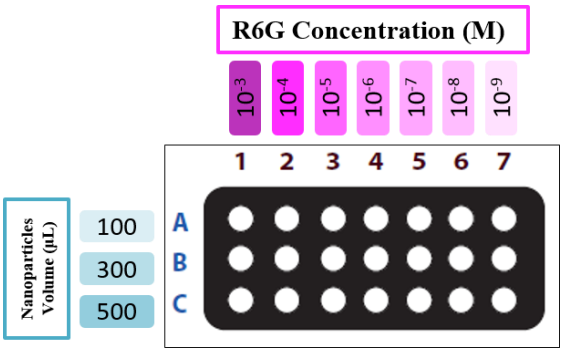

Figure 2. 7|Configuration of the scheme used in the SERS assays performed in the paper SERS substrates. *On the left* the letters A, B and C represents the volume added of the NPs and the numbers 1-7 *on the top* corresponds to the concentration of R6G dropped in the well.

2.3.2 Domoic acid

A DA stock solution was prepared by dissolving DA powder in Milli-Q water. The concentration range was from 10^{-2} to 10^{-12} M and the solutions were deposited as for R6G.

2.3.3 Malathion

The malathion solutions were deposited as for R6G and the range of concentrations was from 3.72 M to $1x10^{-2}$ M.

2.4 Laser power influence in SERS measurements and measure parameters optimization

In the Raman spectrometer the energy of the laser that reaches the sample can be modulated by a suitable filter. The spectrometer used in this work had six filters and the higher its identification number, the lower the laser power reaching the sample (Table II. 1 in Appendix II). The filters prevent the analyte from undergoing degradation by the laser and avoid the saturation point of the CCD observations. The former phenomenon is very common in photosensitive analytes.[88,89] Furthermore, in the case of calculating the analytical enhancement factor (AEF) from different SERS substrates, sometimes the filter had to be changed (for example when saturated signals were observed) because of the distinct SERS efficiencies. However, this parameter requires to be taken into account in the calculation of the AEF. Therefore, a study of the laser power influence was performed. Through applying different filters, it was possible, not only to decide on the filter most suitable to prevent photobleaching of the sample, but also if the vibrational bands areas would be proportional to the power of the laser.

A R6G drop of 2 µL was deposited in the well and was subjected to SERS measurement starting with the highest density filter, *i.e.*, with lower laser power, and proceeding to remove the

filter density thereby allowing the total power of the laser to reach the sample – upward direction. Then, a drop was deposited in the same manner into a second well, and also subjected to SERS measurement, however, in this second case, the readings began with the laser total power and proceeding to the use of stronger filters - downward direction. The SERS substrates consisted in wells (diameter of 4 mm) with 500 µL of AgNSs deposited onto office paper. The R6G concentration used was 10^{-5} M in order to ensure the detection of the analyte. The time of laser exposure toward the sample was timed to guarantee that the exposure times were the same. The paper was always protected from the surrounding light. The assay was performed 7 times.

2.5 Reproducibility between different synthesis batches

Variation in measured signal across various locations has always been a concern for SERS, especially when the substrate has random features. Hence, replicates of the optimized wells were made to ascertain the reproducibility between different batches of AgNSs (n=4). The batches were analysed by depositing 62.5 µL of AgNSs at the same concentration and these substrates were tested with 3 different concentrations of R6G (10^{-7}, 10^{-8} and 10^{-9} M).

2.6 Time stability study of the paper SERS substrate

After the determination of the best qualified paper SERS substrate in terms of performance, replicates of the wells were made to perform a time stability study. The SERS signal was evaluated along 5 weeks. The concentrations of R6G used were, 10^{-6}, 10^{-8} and 10^{-9} M. Between measurements, the paper SERS substrate was kept in the dark and stored at 4 ºC in a desiccator.

2.7 Results treatment

All the raw data were collected digitally and imported into the commercially available software PeakFit v4.12 (Seasolve Software Inc.) for processing. Spectra were analysed using a deconvolution in Lorentzian bands. The adjustments to the spectra were carried out with all parameters allowed to vary: width, centre, and Lorentzian amplitude of each band. A linear baseline subtraction was also performed. The different equations, and display sets of spectra were performed at OriginPro 8.5 software (OriginLab).

2.7.1 Analytical Enhancement Factor calculation

The enhancement factor can be used to compare the average SERS enhancements across different substrates reported by literature.

An analyte solution with concentration (C_{Raman}), produces an average Raman signal (AA_{Raman}), under non-SERS conditions. Then, this signal is compared to the same analyte on a SERS substrate, under identical experimental conditions (laser power, microscope objective or lenses, etc.), and for the same preparation conditions, with possibly different concentration (C_{SERS}), that results in an average SERS signal (AA_{SERS}).[19] The analytical enhancement factor (AEF) can then be defined (Equation 2.1):

$$AEF = \frac{AA\ at\ 1509\ cm^{-1}{}_{SERS} \times C_{SERS}}{AA\ at\ 1509\ cm^{-1}{}_{Raman} \times C_{Raman}} \qquad \textit{(Equation 2.1)}$$

When different filters were applied a filter factor had to considerer to normalize the areas of the signals.

Chapter 3. Characterization Techniques

The characterization techniques used in this dissertation were selected in order to obtain information on the structure and chemical composition of paper SERS substrates samples. Characterization by UV-Vis absorption spectroscopy of NPs synthesized by chemical reduction was also proceed. The efficiency of all the SERS substrates (paper and PVD) was attained by Raman measurements.

3.1 Scanning Electron Microscopy

Scanning Electron Microscopy (SEM) is a useful, non-destructive and versatile technique allowing to collect information on the morphology of materials and surfaces (Figure 3. 1-A and B).[90]

The physical operating principle is based on scanning a sample surface with a high energy electron beam with a wavelength (λ = 0.012 nm) that is much lower than the wavelength of visible light photons. Consequently, it provides a highly magnified image of the surface of the material (<100 000 times) also providing depth of field. The beam is generated by a tungsten filament by applying a potential ranging from 0.5 to 30 kV, accelerated toward the negative electrode. The condenser system, composed of electromagnetic lenses, aligns the beam towards the opening of the objective lens. The lens focus the beam of electrons before they reach the sample. The beam passes through a pair of scanning beam deflection coils horizontally and vertically over the sample surface (Figure 3. 1-B).[91]

When the primary electron beam is focused on the material, electrons carry significant amounts of kinetic energy, but when they reach the solid sample, the electrons gradually loose energy due to recurrent scattering and absorption inside a tear shaped volume of the material. This electron-sample interaction results in a variety of effects. For imaging samples, the secondary electrons and backscattered electrons take special interest. The backscattered electrons illustrate contrast differences of the elements. Heavier elements appear brighter, and lighter elements darker. The secondary electrons allow the analysis of the topography of the surface. The coefficient associated with the emission of secondary electrons (relative to the number of electrons incident), is not dependent on the atomic number, meaning that different materials do not cause variations in contrast image. The factor that most influences the contrast in SEM is surface topography, since the electron beam interaction with the sample increases with the path length traversed resulting in a pattern of the surface.[90,91]

To characterize the substrates mentioned in this work, the equipment Carl Zeiss AURIGA FIB-SEM Crossbeam was used (Figure 3. 1-A). An electron-accelerating voltage of 2.00 or 5.00 kV, and the aperture, 20.000 and 30.000 µm, were used. The working distance between the sample and the objective lens was about 5 mm. The samples were iridium (Ir) coated by sputter (Quorum).

The purpose of SEM analysis in the course of this work was to determine whether the volume of NPs added to the paper surfaces allowed a homogeneous distribution in different papers. The list of samples studied are presented in Table 3. 1.

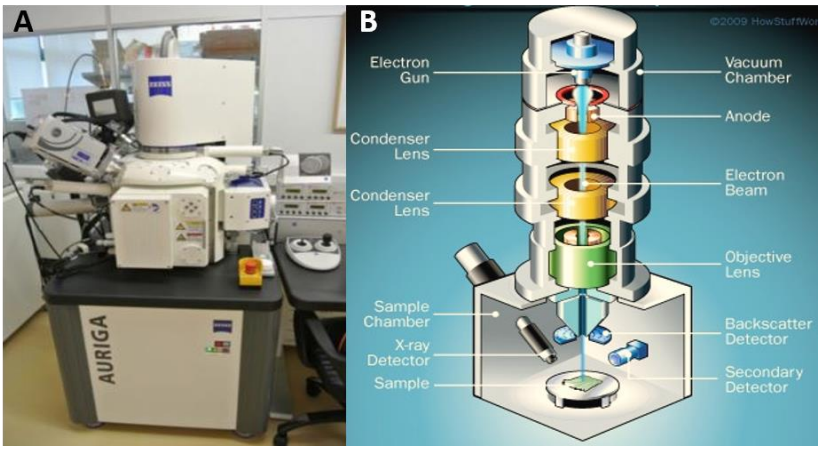

Figure 3. 1|SEM instrument. (A) Apparatus used for SERS measurements; (B) Schematic representation of the functioning of SEM.

Table 3. 1|List of the samples with different conditions studied by SEM.
Abbreviations: AgNPs: citrate capped spherical silver nanoparticles; AgNSs: citrate capped star-shaped silver nanoparticles.

Type of Paper	Type of NPs								
	Non-aggregated AgNPs			Aggregated AgNPs			AgNSs		
	Volume (µL)			Volume (µL)			Volumes (µL)		
Whatman no.1 Paper	**100**	**300**	**500**	**100**	**300**	**500**	**100**	**300**	**500**
Office Paper	**100**	**300**	**500**	**100**	**300**	**500**	**100**	**300**	**500**

3.2 Energy dispersive X-ray spectroscopy

In order to investigate the chemical composition of the materials' surface, energy dispersive X-ray spectroscopy (EDS) analysis was performed. This technique, when coupled with SEM imaging, is especially useful for determining chemical compositions.[92]

Besides the secondary and backscattered electrons, the interaction of the primary beam the sample results in the emission of X-rays. The emitted X-rays has an energy representative of the parent element, providing elemental analysis of the sample. Hence, the elemental composition is given in a spectrum that relates the intensity (number of photons recorded) with the energy of X-rays. This technique also allows producing an elemental image with the distribution of each element in the sample. This technique is limited to identifying elements of atomic number higher than Z = 5 (boron). The detection limit is in the order of 200 ppm for elements with well-defined peaks. The relatively poor energy resolution of the EDS leads to frequent spectral interference problems as well as the inability to separate the members of the X-ray families.[92]

To obtain EDS spectra of the studied materials, an Oxford INCA XACT detector was used with a 15 kV accelerating voltage, and the aperture was 60 µm to maximize the X-ray signal emitted by the samples.

3.3 UV-Vis absorption spectroscopy

All measurements in the UV-Vis spectrophotometer (Spectrophotometer Cary 50 Bio UV-Visible, Varian) were performed in a quartz cell (Hellma, Germany) with 1 cm optical path length, with a wavelength range between 200 and 800 nm at room temperature. With the notable exception of R6G concentration verification at which was used plastic UV-cells.

3.3.1 Characterization of silver nanoparticles

UV-Vis spectroscopy was used to characterize the AgNPs after their synthesis. The evaluation of the explicit LSPR band in the obtained spectra, allows inference about several characteristics of the colloidal solution including the average diameter of the NPs and allows to estimate the molar concentration of AgNPs (according to the previously published work by Paramelle *et al.*)[93], as well as the state of aggregation in solution.

The Paramelle *et al.* method relates the maximum absorption of the colloid solution in LSPR band (approximately 402 nm for AgNPs with ≈20 nm of size) with a diameter of (d) (nm) and therefore it corresponds to a molar extinction coefficient (ε) ($M^{-1}cm^{-1}$). After determining the average size and molar extinction coefficient associated with the AgNPs solution, it is possible to calculate the molar concentration through the Lambert-Beer Law.

The aggregation state of AgNSs was evaluated by UV-Vis spectroscopy by observing a decrease and broadening of the LSPR band (≈379 nm for AgNSs with ≈150 nm of size) which is characteristic of these NPs. Higher the aggregation state of AgNSs, less perceptible is the band, eventually, AgNSs precipitate and become valueless.

3.3.1.1 Stability studies of silver nanoparticles

The stability of the silver NPs solution can be confirmed by comparing the characteristic aggregation band of the particles at ≈745 nm and the LSPR band (at ≈402 nm for AgNPs within the size of ≈20 nm). The stability of the solutions was investigated by varying the ionic strength with the use of sodium chloride (NaCl), and through pH variation, with 1 M HCl and 1 M sodium hydroxide (NaOH).

3.3.1.1.1 At varying ionic strength

Since in the following SERS experiments it will be necessary to aggregate AgNPs, it is important to determine the salt concentration needed to aggregate the citrate-reduced silver colloid. Therefore, different amounts of NaCl were added to a colloidal solution (maintaining a constant concentration of AgNPs) resulting in different ionic strengths (from 0 to 100 mM) allowing to study the stability of the NPs toward salt-induced aggregation.

3.3.1.1.2 At varying pH

Similarly, different pH values were obtained by adding different amounts of acid (HCl) or base (NaOH) 1 M solutions to a colloidal solution of constant concentration. Hence, the stability of the AgNPs could be studied between pH values from 2 to 8. The pH values were measured using a pH meter.

3.4 Raman spectroscopy

The different SERS substrates (paper and PVD substrates) produced throughout the work were characterized by Raman measurements with a Labram 300 Horiba Jobin Yvon spectrometer equipped with an air-cooled CCD detector and a HeNe laser operating at 1750 μW of 632.81 nm laser excitation.

In the micro-Raman configuration, the laser light is both focused and collected through the same objective. The scattered light is passed through a solid edge filter (Horiba) for the removal of Rayleigh-scattered light in the region observed and provided high throughput (90-95 %) for Raman lines. Finally, the light is focused and directed to a spectrometer and detector (Figure 3. 2).[17] The spectral resolution of the spectroscopic system is 4 cm^{-1} and the wavenumber for each point is 0.5 cm^{-1}.

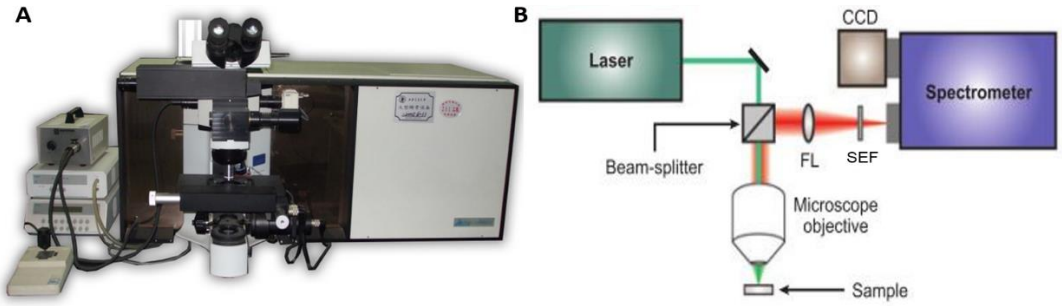

Figure 3. 2|Micro-Raman spectrometer. (A) Apparatus used for SERS experiments; (B) schematic diagram of typical micro-Raman setup, which uses a microscope objective for illumination and collection, increasing the spatial resolution of the instrument (*adopted from*[17]).
Abbreviations: CCD: charge-coupled device; FL: focusing lens; SEF: solid edge filter.

The laser beam was focused with a 50x Olympus objective lens (N10.6 LMPLAN FL N). The white light optical microscopic image of both types of the SERS substrates are shown in Figure 3. 3 to illustrate the locations where the laser was focused. An integration time of 5 scans of 25 s each, was used for all measurements; The long recovery times are expected to be advantageous, but the long irradiation times are usually detrimental, so the 5 scans allows to reduce the random background noise contributed by the detector, without contributing a significant amount of acquisition time.[29,88] In order to avoid the burning of the sample on the paper SERS substrates, the intensity of the incident laser was reduced to 660 µW on the surface of the sample by using suitable filtering. In the case of the PVD substrates and submitted to chemical modifications, the SERS activities could change. In these cases, the laser power was reduced through a neutral density filter in every situation of signal saturation.

Triplicates were taken of all spectra. Between different Raman sessions the spectrograph was calibrated using a Si wafer with the Raman line at 521 cm^{-1} for reducing possible fluctuations of the Raman system. All Raman spectra were recorded at room temperature.

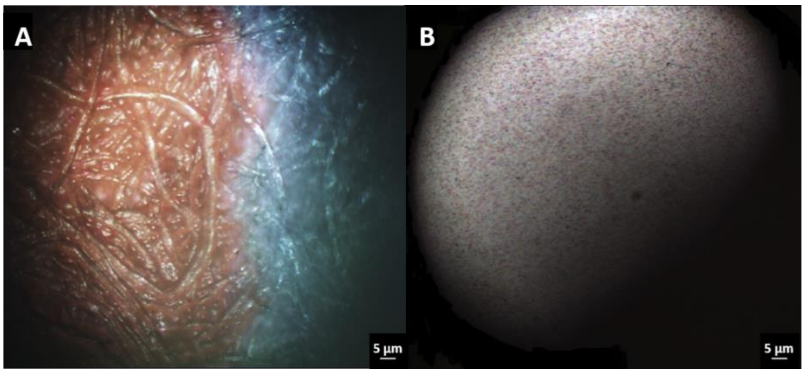

Figure 3. 3|Optical microscopic images of two places where a SERS spectrum were recorded. (A) One on the edge of a dried spot in the paper SERS substrate; (B) one local in the PVD SERS substrate – AgNPs (4 nm of thickness) deposited on Si.

Chapter 4. Presentation and Discussion of Results

This project, as already mentioned before, has the main objective of developing new efficient substrates for SERS application. There were two types of substrates SERS, paper and PVD substrates.

The paper-based SERS substrate is a disposable approach and two types of paper were investigated: Whatman no.1 paper and office paper. Both papers were *drop-casted* with several types of silver NPs with the aim to explore the most suitable alternative for sensitive SERS measurements.

The performance of SERS substrates fabricated by PVD were also investigated. Several modifications were fulfilled with the aim of improve SERS efficiency and accomplishing detection limits in the sub ppb range.

In this chapter the results from the developed work are presented and discussed. The chapter starts with the characterization of the chemically synthesised NPs by UV-Vis spectroscopy studies followed by SEM. Then, the paper SERS substrates were analysed through SEM-EDS and Raman techniques. SERS assays were also performed in order to evaluate the SERS efficiency of the modifications made to the original PVD SERS substrate. The results are presented and the advantages and disadvantages are discussed.

4.1 Synthesis and characterization of silver nanoparticles

In this section the different types of silver NPs will be investigated and compared: non-aggregated and aggregated AgNPs and AgNSs.

4.1.1 Synthesis and Characterization of citrate capped non-aggregated silver nanoparticles by UV-Vis absorption spectroscopy

During the synthesis of AgNPs by the method of Bastús *et al.*, when $AgNO_3$ was added to the reaction mixture, there was a colour change from pale yellow, to strong and bright yellow indicating the forming AgNPs.[83] This method is reproducible since in all syntheses the UV-Vis spectrum obtained was identical, revealing a similar diameter and concentration of AgNPs.

The UV-Vis spectrum after a typical synthesis of spherical non-aggregated AgNPs, according to the Bastús *et al.* method, results on a LSPR band centred at ≈402 nm (Figure 4.1).[83] The width and position of this band can be used to determine the average size and molar concentration of NPs because their optical properties depend on its size and morphology, verifying the *red-shift* phenomenon. This phenomenon consist in a shift to longer wavelengths with increasing diameter average of NPs, related to a decrease in the plasmonic frequency.[93,94]

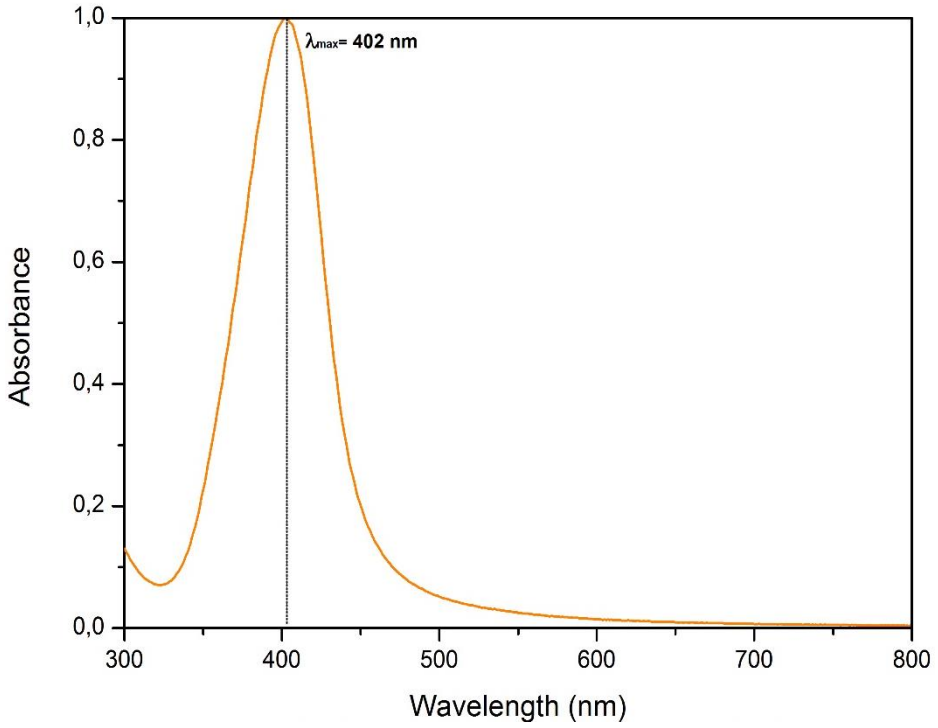

Figure 4. 1|UV-Vis spectrum after a synthesis of AgNPs according to the Bastús *et al.* method. The AgNPs present a LSPR band centred approximately at 402 nm.

To calculate the average diameter and the molar concentration of AgNPs the Paramelle *et al.*[93] method was used. This method is based on previous work of Haiss *et al.*[94], reporting a method of calculating these parameters for spherical AuNPs coated with citrate using the respective absorption spectrum (Figure 4. 1). First, the average diameter of AgNPs is determined by relating this parameter (x) with maximum absorbance (y) by the following equation (the corresponding function can be seen in Appendix III):

$$y = 397 + 9.58 \times 10^{-2} x^2 \qquad \textit{(Equation 4.1)}$$

After inferring the average diameter of the AgNPs (≈23 nm), it is possible to estimate the molar extinction coefficient thereof by Equation 4.2 (the corresponding function can be seen in Appendix III):

$$y = -1.493 \times 10^{9} + 6.984 \times 10^{8} e^{0.104x} \qquad \textit{(Equation 4.2)}$$

Achieving $\varepsilon_{402\,nm}$ value of $\approx 6.21 \times 10^{9}\ \mathrm{M^{-1}cm^{-1}}$. Finally, using Lambert-Beer's law (Equation 4.3), where b, is the optical path length, and c is the molar concentration, the concentration of the AgNPs solution is approximately 0.66 nM.

$$A = \varepsilon_{402\,nm} bc \qquad \textit{(Equation 4.3)}$$

The width and symmetry of LSPR band in UV-Vis spectrum is representative of the high monodispersivity of the AgNPs in colloidal solution. This result is due to the use of TA that lower the size distribution by a process explained in the La Mer model. A rapid reduction leads to a nucleation burst, producing smaller cores. In homogeneous conditions these cores grow to yield, well distributed NPs. Conversely, if the reduction is slower, the nucleation overtakes the growth process, leading to the formation of heterogeneous particles. Subsequently, it is difficult to control the size distribution.[28] The rapid reduction occurs, at smaller TA concentrations due to the strong complexation capacity of TA achieving stabilized intermediate forms of Ag^{+} ions. These

intermediates are dissolved, acting as a source of atoms for the nucleation and growth of AgNPs.[83] Thus, TA acts as the primary reducer of the reaction, while SC has the function of a secondary reducer and stabilizer, leading the growth process since the catalytic core is formed. A detailed reaction scheme is described in Appendix IV.

It is important to mention that this method of diameter and concentration calculation and analysis of UV-Vis spectra, is an average of the size of AgNPs. Although it has not revealed disparities between theoretical and experimental values, a more detailed and statistically accurate analysis could be confirmed with appropriate techniques. Transmission Electron Microscopy (TEM) allows to characterize NPs with high resolution since the image is created from an interaction of the sample with a beam of electrons.[28,83,84,93,94]

Nevertheless, the Bastús *et al.* method provides an improved procedure for the AgNPs synthesis over the method of Lee and Meisel. Well distributed AgNPs with a desired diameter were obtained. Moreover, the lack of use of strong surfactants promotes the accessibility of the surface of the NPs, a crucial factor in SERS field.[28,83]

4.1.1.1 Stability studies of silver nanoparticles

4.1.1.1.1 At varying ionic strength

The other type of NPs used in this work was the aggregated AgNPs. They are known to be very advantageous for SERS substrates due to an extension of the LSPR into the red and IR, and to the several *hot spots* which leads to higher surface enhancements.[33]

The aggregation of the different colloidal NPs, proceeds by increasing the interactions between colloid particles and is triggered by an aggregating agent.[28] In general, AgNPs aggregation is induced by using aggregation agents such as electrolytes (*e.g.* nitric acid, metal halide or sulfate salts). The aggregating agent chosen was NaCl since Cl^- Raman spectrum does not have intense lines on the energy region of interest. The presence of Cl^- is only observed at about 244 cm^{-1} via the v(Ag-Cl) stretching motion.[95,96] Hence, this anion does not interfere with the adsorbate SERS spectra.[97] The concentration of the aggregating agent that is added to the colloidal particles is a prominent factor. In fact, if too much aggregating agent is added, the solution undergoes extended aggregation. The particles will quickly precipitate out of solution and no SERS intensity will be observed as the *hot spots* are occluded within larger structures.[96,98]

For this reason, different amounts of NaCl were added to a colloidal solution resulting in different ionic strengths allowing to study the stability of the AgNPs toward salt-induced aggregation (Appendix V.A). An UV-Vis spectrum of an AgNPs solution after addition of a 50 mM NaCl added is represented in Figure 4. 2.

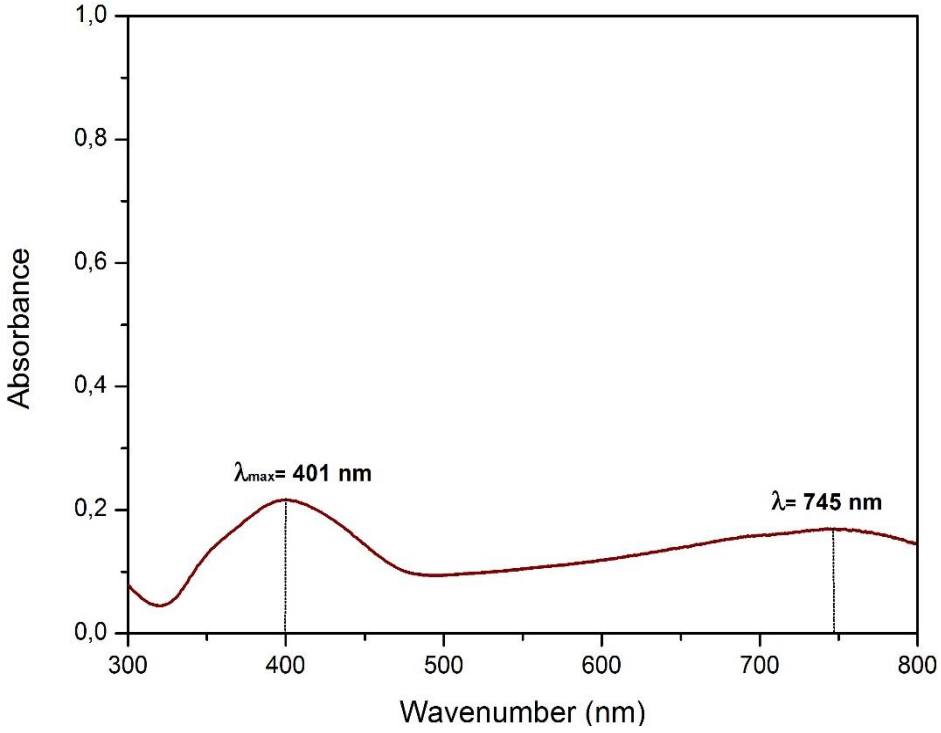

Figure 4. 2|UV-Vis spectrum after an aggregation with NaCl (50 mM) of AgNPs. The aggregated AgNPs present two main LSPR bands centred approximately at 401 nm (corresponding to non-aggregated species) and ≈745 nm (a very wide and broad band).

Over the course of the addition of NaCl, a short lived (<1 s) colour change to blue before becoming colourless due to the aggregation of the AgNPs. A formation of clusters was perceived by UV-Vis spectrum. The LSPR band at ≈401 nm decreased and a shift of the absorption profile of the colloids to longer wavelengths (≈745 nm) was also observed. This band (≈745 nm) presumably indicates NP dimers and higher aggregates (Figure 4. 2).[98]

The aggregation behaviour of AgNPs in NaCl solutions is supported by the DLVO theory[4]. According to DLVO theory the NP-NP distance is an effective sum of attractive (*e.g.*, van der Waals) and repulsive (*e.g.*, electrical double layer) forces. Thus, provides an explanation of the stability and aggregation of colloidal solutions as a function of the ionic strength.[98] With increasing NaCl concentration, the citrate-coated AgNPs became less negative due to an increase in charge screening. At low concentrations of NaCl, the growth in concentration will promote a charge screening leading to a reduction in the thickness of the diffuse double layer. At high concentrations, the charge of citrate in AgNPs is completely screened and the energy barrier between the particles is eliminated. Hence, NaCl fulfilled properly its role, promoting the aggregation by increasing the ionic strength of the solution.[99,100]

The critical coagulation concentration (CCC), *i.e.*, the minimum amount of electrolyte needed to completely destabilize the suspension, obtained was 50 mM. This value is in remarkable agreement with other reports where the concentration achieved was 47.6 mM.[99] Thus, the CCC determined by this assay was added to produce the aggregated AgNPs used throughout this work.

4.1.1.1.2 At varying pH value

As already mentioned, the AgNPs are coated by charged molecules, capping agents (*e.g.* citrate) which are able to prevent their aggregation through electrostatic repulsion. The citrate-reduced

[4] Acronym is derived from the authors of the theory, Derjaquian, Landau, Verwery, and Overbeek honouring the co-discovery of the theory.

AgNPs are stabilized by a surface layer of silver citrates, with pendant negative carboxylic acid groups since the pK_a values of citrate are 3.13, 4.72 and 6.33. The stability of the AgNPs was studied between pH values from 2 to 8 (Appendix V.B). [96]

When the pH of the surrounding medium equals the pK_a=3.13 of these charged molecules, the citrate charge becomes null and allows for a greater degree of NP-NP interaction resulting in an increase in the level of aggregation (Figure 4. 3).[99,100]

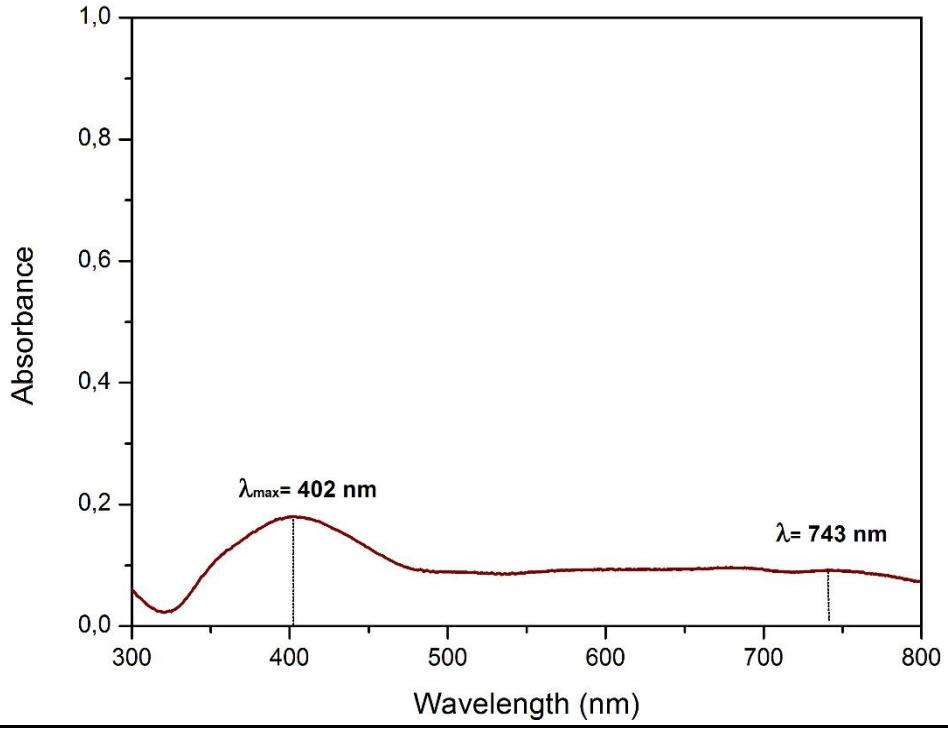

Figure 4. 3|UV-Vis spectrum of aggregated AgNPs when the pH value reaches 3 through HCl addition. AgNPs become aggregated due to the neutralization citrate resulting in a spectrum with two main LSPR bands. One, centred at ≈402 nm (corresponding to non-aggregated species) and a new band at ≈743 nm (a very wide and broad band).

4.1.2 Characterization of citrate capped star-shaped silver nanoparticles by UV-Vis absorption spectroscopy

Each batch of newly synthesized AgNSs was analysed by UV-Vis spectroscopy. As can be seen, AgNSs gives rise to a spectrum displaying one strong peak at 379 nm and at longer wavelengths an extinction background (Figure 4. 4).

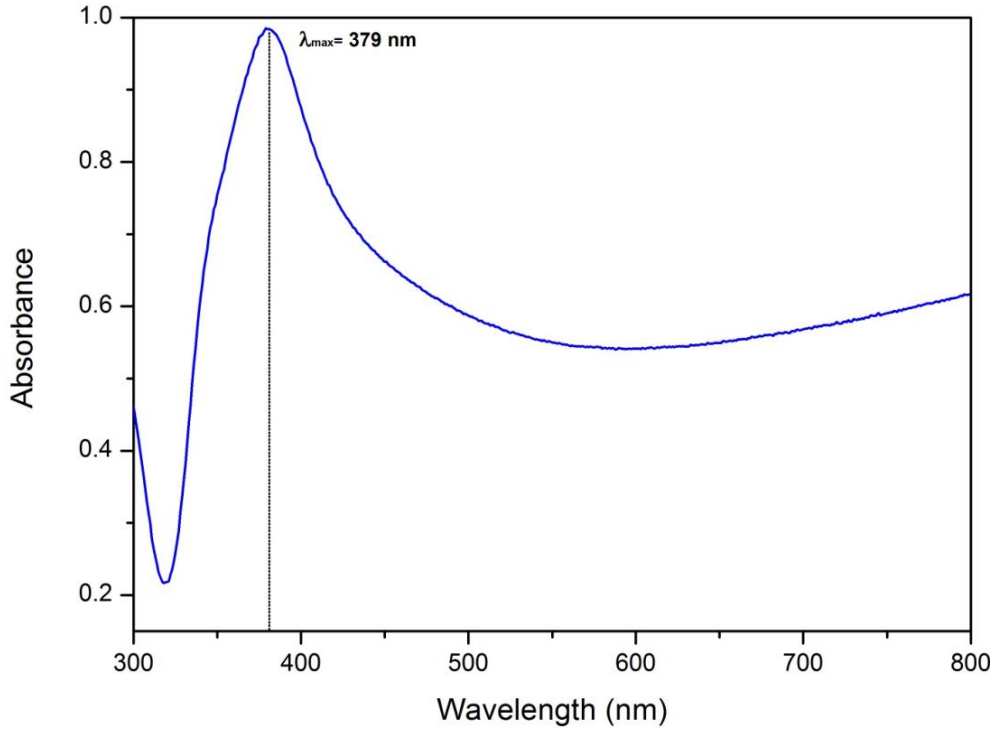

Figure 4. 4|UV-Vis spectrum after a synthesis of AgNSs. The AgNSs present a LSPR band centred approximately at 379 nm and an extinction background at longer wavelengths.

The large extinction background arises from the very different LSPR bands in the suspension giving a wide range of wavelengths in the visible and near-IR. The wavelengths at near-IR region with a broad width are characteristic in the structures with sharper vertices that lead to a greater enhancement. These effects are due to the increasing confinement of the surface charge density at the sharp edge. The several distinct LSPR bands are derivate of the several morphologies of all the existing NPs with different number of arms and tip sharpness (see section 4.1.3). The AgNSs with larger vertex angles or a higher number of arms, probably are involved in the more modest multi-pole resonance peak and narrower bandwidth at lower wavelengths (*blue-shift* of resonant wavelength).[20,21,84] Therefore, the method presented by Garcia-Leis *et al.* have opened a new branch for shape-controlled metal nanocrystals without using strong surfactants that would compromise their use on SERS-based detection methods.[84]

4.1.3 Scanning electron microscopy

The morphology of the synthesized NPs was characterized by SEM and Figure 4.5 shows the obtained results and the relation between the different UV-Vis spectra.

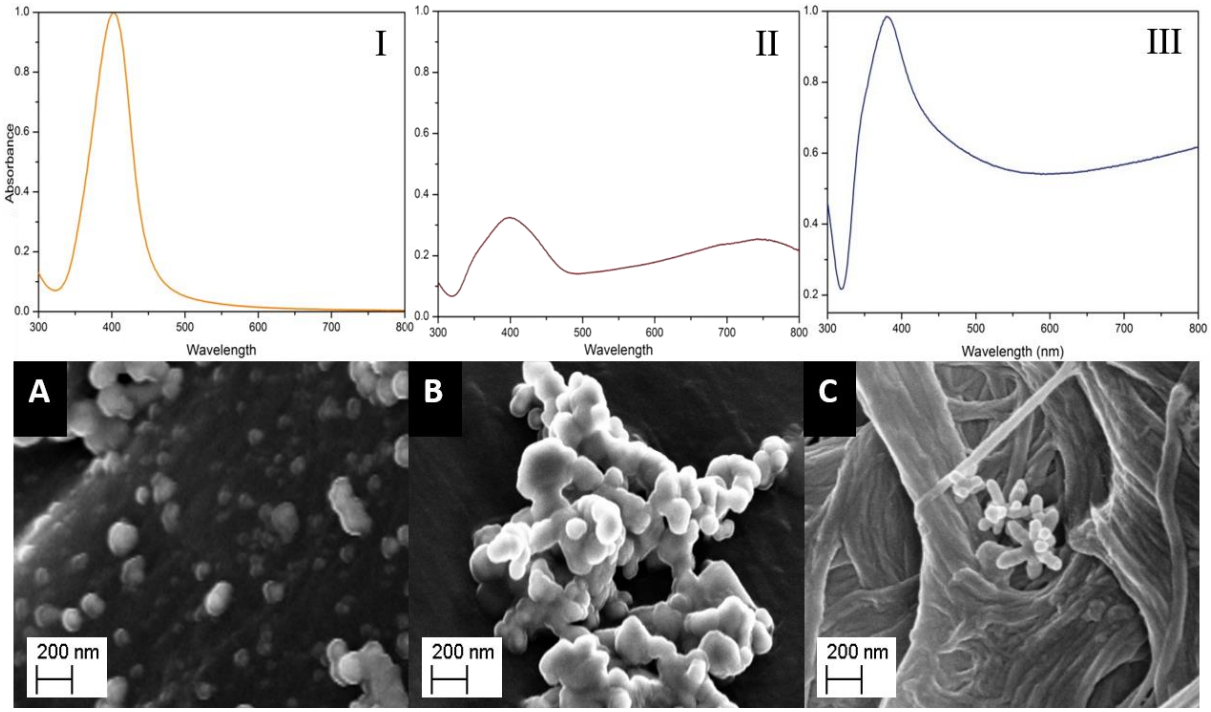

Figure 4. 5|SEM images of the NPs synthesized for SERS substrates and the corresponding UV-Vis spectrum above each image. (I) UV-Vis spectrum of non-aggregated AgNPs and (A) is the corresponding SEM image; (II) the UV-Vis spectrum and (B) SEM image of aggregated AgNPs; (III) UV-Vis spectrum and (C) SEM image of AgNSs.

The results show that the NPs have the desired shape depending on the synthesis process (Figure 4. 5). The presence of spherical AgNPs is confirmed by the Figure 4. 5-A displaying clear spherical structures on the surface of the paper with various dimensions. Interestingly, while the chemical synthesis of AgNPs allows an average size of ≈20 nm (it is important to note that due to the SEM sample treatment, the NPs appear to be larger), there is some non-homogeneous size distribution corroborating the fact that the diameter calculation method from the UV-Vis spectrum only represents the average dimension of the NPs. Moreover, there is some aggregation of the colloidal NPs after the solution deposition in the paper, which is not verified when measuring the UV-Vis spectrum (Figure 4. 5-A).[33]

In the case of aggregated AgNPs (Figure 4. 5-B), highly disorganized structures are observed with different sized ridges and significantly higher dimension than the non-aggregated AgNPs. This change also confirms the absorbance spectrum measured after adding salt, causing a LSPR band *red-shift*.[98]

In Figure 4. 5-C it is noted that the structure of star-shaped NPs was achieved by observing NPs with various arms of different sizes spiking from a core. Hence, the two step colloidal synthesis of AgNSs employed was successful. The number of arms *per* particle can also vary which is in agreement with the results published by Garcia-Leis *et al.*.[84] Overall, the tips of the observed arms display a low sharpness.

The sharp protrusions and the junction between the two spherical surfaces are locations which should be favourable sites for molecular adsorption and yield the required electromagnetic field enhancement.[20,101] These NPs were subsequently used to produce paper SERS substrates.

4.2 Raman and SERS signal of Rhodamine 6G

The spectra given in Figure 4. 6 corresponds to the Raman spectrum of 10^{-3} M R6G aqueous solution and the SERS spectrum of 10^{-6} M R6G adsorbed onto AgNSs in office paper using 632.8 nm

excitation. These spectra are in good agreement with respect to both the frequencies and the relative intensities with those reported in the literature.

The vibrational bands energies are highly conserved between normal Raman and SERS, what is indicative that there is an electrostatic interaction between R6G and the Ag surface.[102]

In both Raman and SERS spectra, the two strongest bands correspond to the aromatic C-C stretching modes at 1361 and 1509 cm^{-1}. The bands positions at 1575 and 1649 cm^{-1} are also associated with the same vibrational modes. The spectral features characteristic of R6G at 1127 and 1182 cm^{-1} are assigned to the C-H stretching and C-H and N-H bending. The region with the band positions at 1310 cm^{-1} is due to N-H bending and CH_2 wagging. The corresponding vibrational band assignments are summarized in Table 4.1.[42,103]

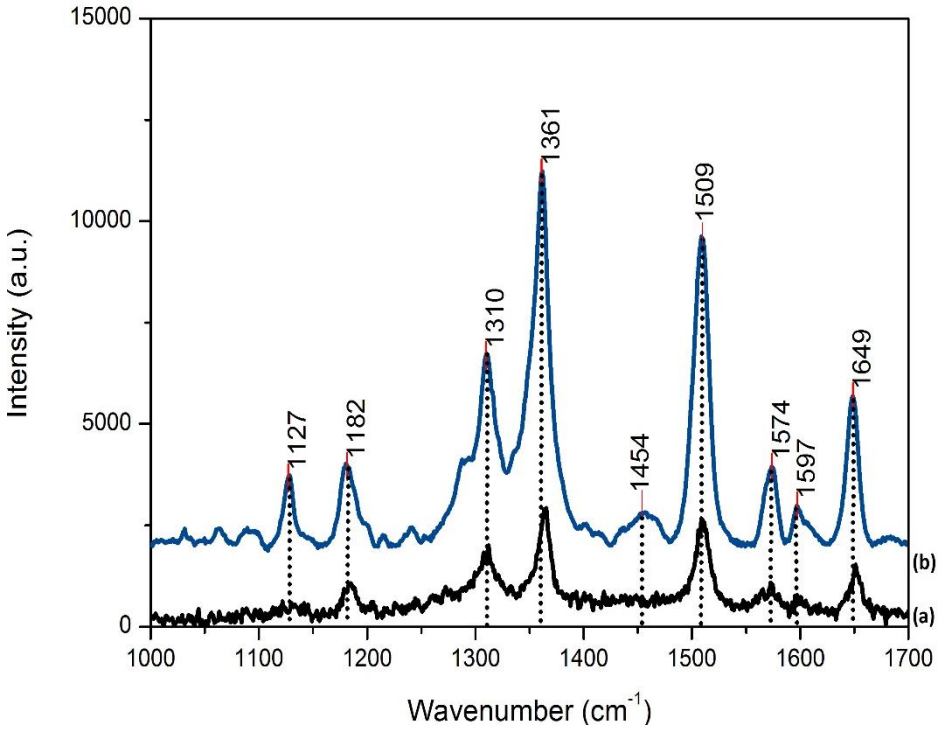

Figure 4. 6|Raman and SERS spectrum of R6G. (a) Raman spectrum of 10^{-3} M R6G aqueous solution (x10 magnified) and (b) SERS spectrum of 10^{-6} M R6G adsorbed on AgNSs on office paper under 632.8 nm laser excitation. Since there was not vibration shifts from the others SERS substrates (*e.g.* PVD SERS substrates), there were not represented.

The 1361 and 1509 cm^{-1} bands intensity are more enhanced probably because these vibrational modes of the adsorbed sample have a large polarizability constituent perpendicular to the metal surface.[96] Firstly, the band at 1361 cm^{-1} was chosen to the subsequent analysis, however, due to some interferences observed from the paper SERS substrates (see section 4.6), the band 1509 cm^{-1} was preferred.

Table 4.1|Vibrational bands assignments for R6G.[42,103]
Abbreviations: vw: very weak; w: weak; m: medium; s: strong; vs: very strong.

Experimentally observed bands (cm^{-1})		Strength	Assignment
Raman	**SERS**		
	1030	vw	
	1127	m	in plane C–H bending
1183	1182	m	C–H bending, N–H bending, in plane xanthene ring deformation
1310	1310	s	In plane xanthene ring breathing, N–H bending, CH2 waggling
1362	1361	s	Xanthene ring stretching, in plane C–H bending
	1454	w	COH bending
1509	1509	vs	Aromatic C–C stretching, xanthene ring stretching, C–N stretching, C–H bending, N–H bending
1574	1574	m	Xanthene ring stretching, in plane N–H bending
1597	1597	w	
1649	1649	s	Xanthene ring stretching, in plane C–H bending

4.3 Development of paper SERS substrate

The main stages for the development of paper SERS substrate include: (1) formation of hydrophobic barriers; (2) deposition of the NPs previously synthesised in the well; and (3) final assay in Raman spectroscopy for the detection of analytes.

4.3.1 Hydrophobic barriers production

As mentioned above, hydrophobic barriers are needed to contain the NPs preventing the solution diffusion that would result in a weaker SERS signal. At the same time, the barriers prevent contamination of adjacent samples, even in the office paper that is more hydrophobic than Whatman no.1 paper (Figure 4. 7). Therefore, the printed patterns were heated at 140 °C for 2 min, allowing the wax to melt and spread through the paper thickness, creating the desired hydrophobic pattern.[39]

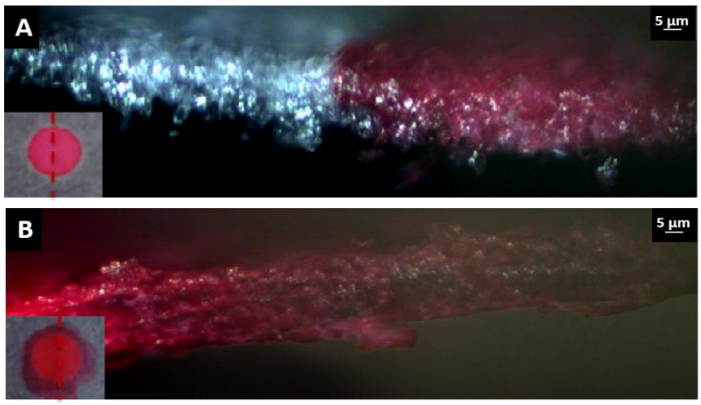

Figure 4. 7|Optical microscopic images illustrating the consequences of not proceeding to the wax diffusion (paper cross sections). The printing is only at the surface of the paper and to create the wells to control the NPs solution the wax diffusion needs to be promoted by a heating plate. Paper with (a), and without (b) wax diffusion.

4.3.2 Well Impregnation by *drop-casting* with NPs

The final step for the SERS substrates fabrication is the impregnation of the NPs by *drop-casting* method. The method consists in spreading the NPs solution over a substrate and allowing it to dry under controlled conditions, *i.e.* pressure and temperature.[39] With each successive *drop-casting* cycle the wells appear gradually darker which is attributed to the formation of NPs clusters.[33]

To validate the deposition of NPs onto the paper surfaces and their distribution, the paper SERS substrates were submitted to SEM-EDS technique (see sections 4.5.1 and 4.5.2).

4.4 Laser power influence in SERS measurements and optimization of the measurement parameters

An important parameter in SERS is the influence of the laser beam and the sensibility to thermal and photolytic processes inherent to SERS systems. For highly photosensitive compounds the irradiation time is even more prominent due to the decomposition or the chemical reaction of the analyte (*e.g.* R6G).[88,89] Additionally, several different chemical and morphological changes can be found in SERS substrates. [28]

When the laser beam is focused to a spot size such as in micro-Raman experiments, this is particularly true, and the type of damage is not always noticeable. Sometimes is very obvious (hole burned in the sample) or it can be more subtle, resulting in spectra not representative of the original sample. Thus, the laser power can have an adverse impact on the quantitative and qualitative aspects of SERS due to a misinterpretation of the analytical data, compromising the experimental results.[104]

To surpass these problems a neutral density filter can be used to reduce the power of the incident beam at the surface of the SERS-active substrate. However, it is worthwhile to mention that this method, although improving the spectral quality of Raman bands, also causes diminished sensitivity. Other methods involve, a rotating stage in contact with the laser beam (moving platforms can sometimes disturb the systems that are being studied resulting in band changes), or defocusing the laser beam (Raman microscopes are incapable of reproducible defocusing conditions).[88,89,105]

The study with 10^{-5} M solution of R6G under stationary conditions showed considerable changes in their spectral features as a function of the irradiation laser power. The evolution of the spectra with stepwise decrease and increase in laser power is shown in Figure 4. 8-A and B.

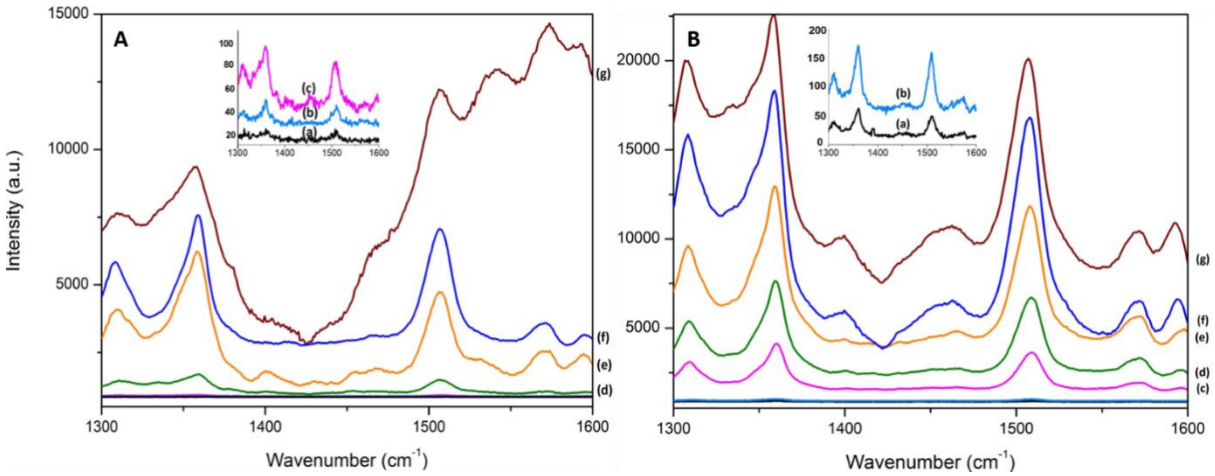

Figure 4. 8|Spectral features of 10^{-5} M R6G as function of the irradiation laser power under stationary conditions. The evolution of the spectra with stepwise decrease (A) and increase (B) in laser power with the following intensities: (a) 1.44 µW (b) 11.8 µW (c) 86.6 µW (d) 660 µW (e) 1750 µW (f) 4020 µW (g) 7870 µW. The time of laser exposure toward the sample was timed to guarantee that the exposure times were the same.

The appearance and band resolution of SERS spectra can be significantly altered even under conditions of modest power intensity. At the highest laser power tested (7870 µW), the intensity increase of bands is so fast that occasionally the saturation point of the CCD was reached in a few seconds but the continuous irradiation of the sample broadened the bands.[88] Subsequently, the laser beam over the SERS substrate leaded to a significant broadening of the bands in the 1300–1600 cm^{-1} region indicating the rapid decomposition of the dye.[89] This broadening was observed with laser powers as low as 1750 µW Figure 4. 8-A *(e)*.

The evolution of the spectra with stepwise decrease in laser power caused a more visible decline in band areas (Figure 4. 8-A) than the evolution of the spectra with the growing of the laser power (Figure 4. 8-B).

It should be pointed out that in the Figure 4. 8-B, it is perceived a broadening as the laser power increased (mostly in 1300-1400 cm^{-1}). Thus, although the stepwise growing power mitigates the deleterious effects, it did not eliminate entirely, inducing permanent damage to the substrate surface.

An incident power of the laser beam of 86 µW resulted in a minimal change in bandwidth of the SERS signals. Conversely, the spectra still exhibit an intense noise. The 660 µW is considered a very low laser power for a conventional Raman measurement.[105] Moreover, it is effective in the collection of SERS spectra because it resemble the signals observed by conventional Raman spectrometry at high analyte concentrations. Therefore, the laser power 660 µW with the 5 cycles of 25 s has proven to minimize the laser irradiation effects within a minimal residency time of the laser beam on the sample.

4.5 Characterization of paper SERS substrates

Comparison between different NPs: non-aggregated and aggregated AgNPs, and AgNSs; in different supports papers (Whatman no.1 and office papers) was performed by applying different techniques: SEM, EDS and Raman spectroscopy.

4.5.1 Scanning electron microscopy

Given that paper is the solid support matrix for the SERS substrates, it is important to know their chemical and structural properties and their behaviour as SERS substrates. Two types of paper were studied: Whatman no.1 and office.

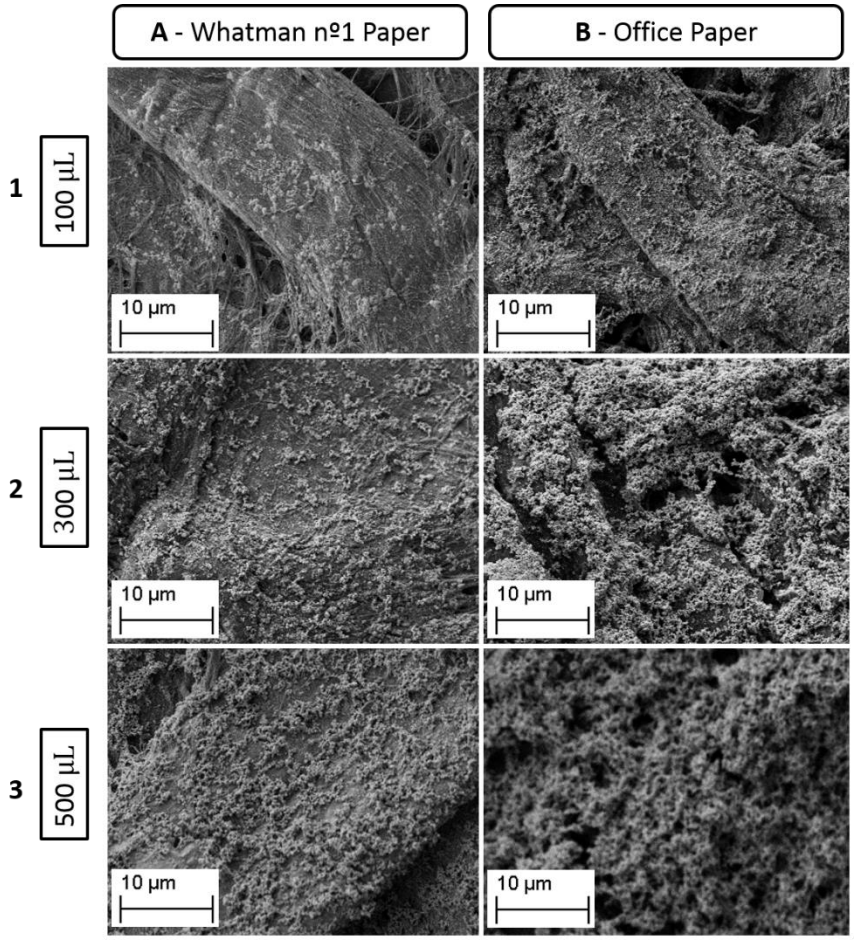

Figure 4. 9|SEM images of AgNPs in the two types of papers: (A) Whatman no.1 and (B) office. From the top to the bottom of the figure, the volume added onto the paper well increases from (1) 100 µL, (2) 300 µL and (3) 500 µL. For higher volumes added, more NPs are observed in the paper surface regardless of the type of paper. However, for office paper, the necessary amount to cover the same area of the paper surface is much lower than for Whatman no.1 paper.

SEM was performed to compare the NPs distribution in the Whatman no.1 and office papers. Thus, several volumes (100, 300, and 500 µL) of NPs were added to wells (4 mm of diameter). As expected, a larger addition of volume, corresponded to a higher number of NPs covering the paper surfaces (Figure 4. 9*(1-3)*). The *drop-casting* is a procedure where the NPs are randomly distributed and as the water evaporates, the NPs form aggregates in both papers. This event is also reported elsewhere.[33,36] The observed results for the non-aggregated AgNPs (Figure 4. 9) and AgNSs (Appendix VI) were congruent, however, for the aggregated AgNPs there was no possible comparison since the salt prevented a reliable analysis (Figure 4. 10).

For the Whatman no.1 paper the volume of 500 µL allowed a closely-packed NPs assembled on the surface of the paper. Considering the office paper, the volume of just 300 µL was sufficient.

This event relates to a macroscopic feature that distinguishes both considered papers, the porosity, being ≈49 and ≈68 % for office and Whatman no.1 papers, respectively.[106] Due to the higher density of the office paper, the NPs are found more at the surface of the paper leading to a less heterogeneous layer than in the Whatman no.1 paper for the same added volume. The latter, due to the greater inherent porosity of the paper, the permeability to NPs is superior, preventing the formation of a cohesive layer on the surface of the paper.

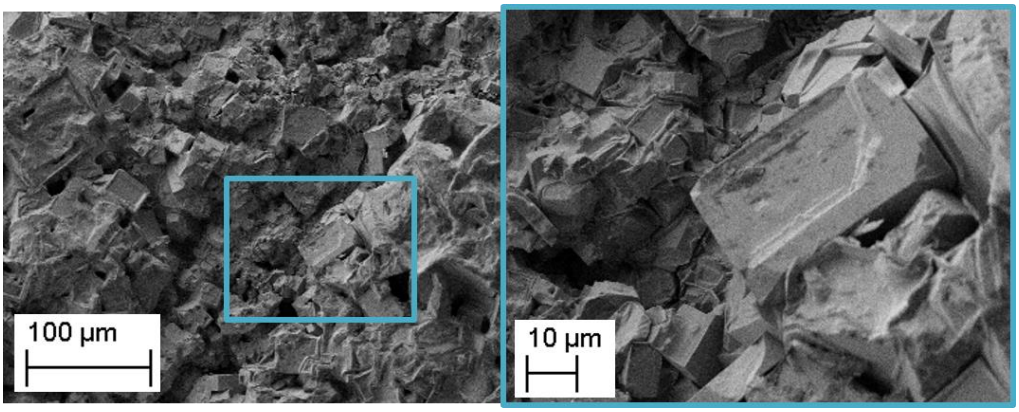

Figure 4. 10|SEM image of a well with aggregated AgNPs. It shows several salt crystals preventing their visualization.

4.5.2 Energy-dispersive X-ray spectroscopy

To prove and consolidate the previously established assertions, it was mandatory verified if the permeability of the papers influences the distribution of NPs at their surfaces. Thus an analysis of EDS in the cross section of both papers was performed. In Figure 4. 11 is represented the cumulative spectra provide by EDS analysis.

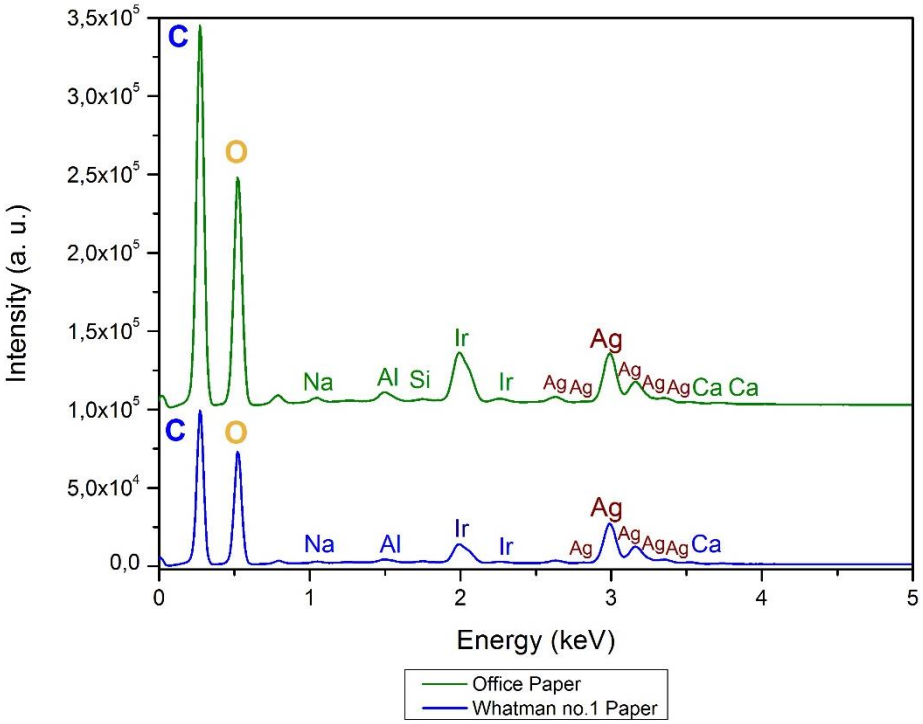

Figure 4. 11|EDS analysis of the paper SERS substrates. Cumulative spectra of the EDS analysis of the Whatman no.1 paper (represented in *green*) and office paper (represented in *blue*) after deposition of AgNSs. The chemical symbols *on the top* of each peak represent the corresponding element identified by the EDS technique and the intensity is indicative of the relative quantity of the elements.

Since the EDS spectrum is a semi-quantitative analysis of chemical composition of the sample, it becomes liable to confirm the presence of the chemical elements expected as well as their relative amounts on paper. The peaks corresponding to carbon (C) ($\mathrm{E} = 0.277\ \mathrm{keV}$) and oxygen (O) ($\mathrm{E} = 0.525\ \mathrm{keV}$) atoms are the most prominent. This occurs on both papers since C and O are the constituents of cellulose, the main component of paper (Figure 4. 11).

The presence of a common initial peak to all papers, corresponding to $\mathrm{E} = 0\ \mathrm{keV}$, is characteristic of the equipment. The Ir peaks at $\mathrm{E} = 1.991$ and $\mathrm{E} = 2.254\ \mathrm{keV}$ are due to the samples coating surface and do not provide any information about the samples.

Comparing to Whatman no.1 paper (98 % of cellulose), office paper is composed by more elements.[107]

The detection of calcium (Ca) may indicate the presence of the mineral additive calcium carbonate ($CaCO_3$). $CaCO_3$ is widely used in papermaking to improve the brightness and opacity of papers and increases the better ink reception.[108] This element identified by energy peaks of $\mathrm{E} = 3.692$ and $\mathrm{E} = 4.013\ \mathrm{keV}$ is also present in Whatman no. 1 paper ($\mathrm{E} = 3.692\ \mathrm{keV}$), although in trace amounts (Figure 4. 11).[107,109]

The aluminium (Al) ($\mathrm{E} = 1.494\ \mathrm{keV}$) and Si ($\mathrm{E} = 1.746\ \mathrm{keV}$) elements were also identified indicating the presence of kaolinite ($Al_2Si_2O_5(OH)_4$) (hydrated silicate aluminium).[40]

The presence of AgNSs was confirmed by the represent peaks of Ag, namely $\mathrm{E} = 2.990;\ 3.150;\ 3.363;\ 3.528\ \mathrm{keV}$ (Figure 4. 11). The presence of elements sodium (Na) ($\mathrm{E} = 1046\ \mathrm{keV}$) and Cl ($\mathrm{E} = 2628\ \mathrm{keV}$) was vestigial, being ubiquitous in such substrates.[106,110]

EDS technique has to be complemented with other methodologies because EDS provides information on the elements in the sample and not the compounds formed by the detected elements. So Raman spectroscopy analysis was proceeded in both papers.

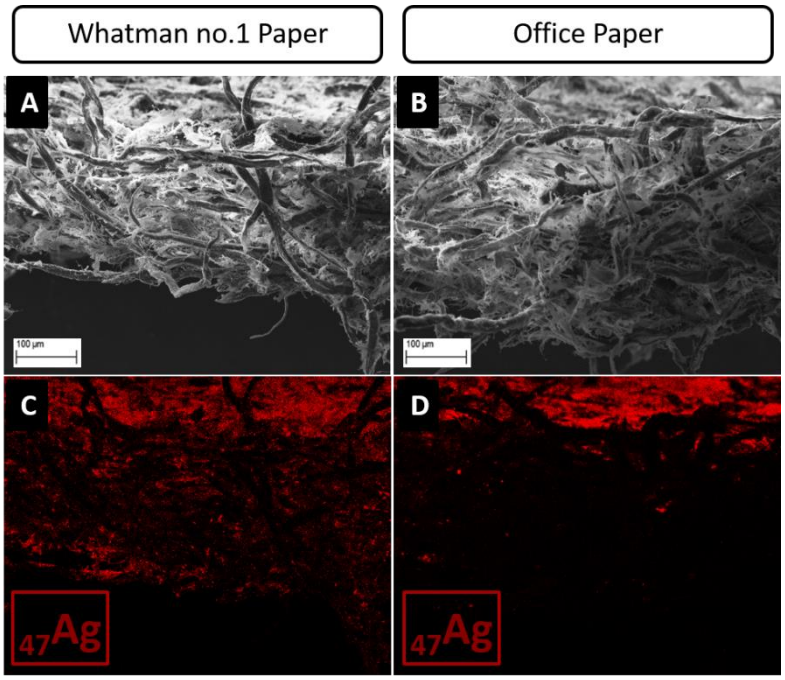

Figure 4. 12|SEM image of the cross section of paper SERS substrate in both papers: (A) Whatman no.1 paper and (B) office paper; and EDS analysis showing the presence of the Ag element along the thickness of the papers: (C) The Ag can be seen through all the thickness of the Whatman no.1 paper although more concentrate at the surface. (D) Conversely, the Ag is observed nearly only the surface of the office paper.

Performing an EDS analysis, allows to obtain a distribution map of the detected elements. As aforementioned, the C and O elements are the main constituents of this paper substrate, so the images display the fibers in the image of SEM (Appendix VIII.A and B). However, the Ag distribution map in the cross sections of both papers, is remarkably different (Figure 4. 12-C and D). The AgNSs are distributed through the entire thickness of Whatman no.1 paper, with a superior concentration on the paper surface's. Conversely, the AgNSs added to the office paper were observed practically only on the surface. As previously reported, the porosity of the papers is distinct being smaller for the office paper. Thus, the decreased permeability leads the AgNSs to be more retained on the surface and distributed more evenly in this paper than in Whatman no.1 paper (as seen in section 4.5.1).

4.5.3 Raman Spectroscopy of different types of paper

Although cellulose is known to be a poor Raman scattering material, it is an organic material and so, it is important to verify if the scattered light from the paper SERS substrate can overwhelm the signal from the analyte. Besides the low scattering, the main features of the cellulose fibers spectra were possible to obtain and agree well with the band positions reported earlier (Figure 4. 13).[111,112]

The different papers were measure by Raman at the spectral range of interest for SERS detection (500-3100 cm^{-1}).

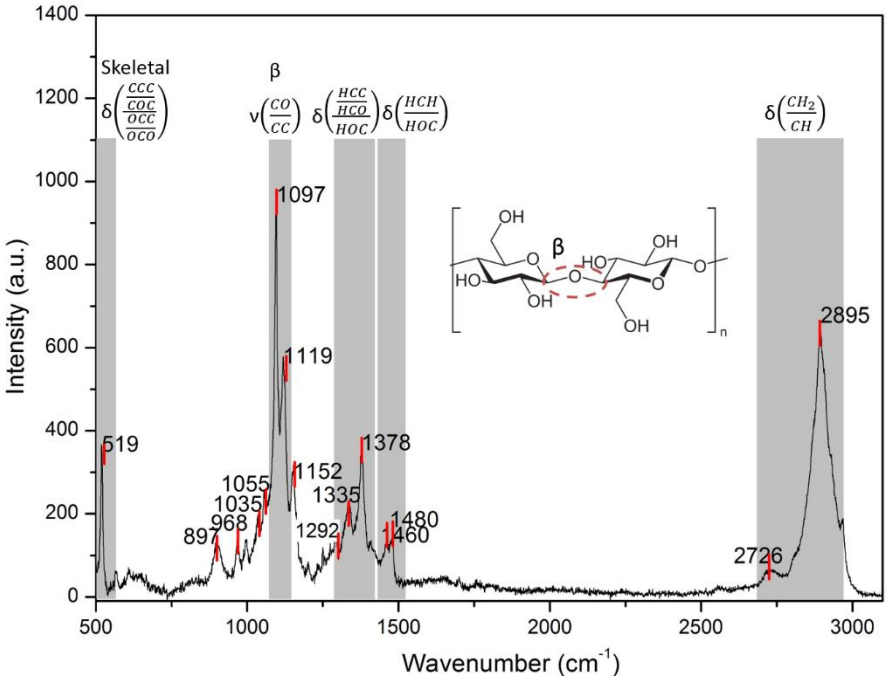

Figure 4. 13|Whatman no.1 Raman spectrum. The regions that represent cellulose bonding vibrations are in *grey* colour. *On the top* of the *grey* area are indicated the type of vibrational modes. The chemical structure (chain conformation) of two unit of cellulose is display in the inset (*adapted from*[39]).

The corresponding vibrational band assignments are summarized in Table 4. 2. The presented bands in Whatman spectrum are from cellulose and any other material as for example lignin (*c.a.* 1600 cm^{-1}) is not observed (Figure 4. 13). This is not surprising because Whatman paper is manufactured from high quality cotton linters to guarantee quality and reproducibility. This is congruent with the finding of highly crystalline cellulose fibers originated from cotton cellulose that have a higher degree of polymerization and crystallinity than wood cellulose (being classified as having a semi-crystalline cellulose structure).[39,107]

Table 4. 2|Vibrational bands assignments for Whatman no.1 paper.[107,111,112]
[1]there are differences in the assignments among literature.[107,111,112]

Experimentally observed bands (cm^{-1})	Strength	Assignment
519	vw	skeletal-bending modes involving the CCC, COC, OCC, and OCO internal coordinates
890 1060	m m	highly-crystalline cellulose II fibres[1]
1097	vs	stretching modes of C-C and C-O, C–O–C of β-glycosidic linkage of cellulose
1119	m	stretching modes of C-C and C-O
1335 1378	w m	HCC, HCO and HOC bending modes
1460 1480	w w	HCH and HOC bending modes
2700 3000	w s	CH and CH_2 bending modes

In the office paper, to ensure that all chemical components in the sample were observed and to test if the background signal was uniform along its surface ($CaCO_3$ agglomerations between the fibers), an enlarged area of its surface area was analysed by Raman. However, these spectra were not easy to obtain due fluorescence effect from the chemical additive $CaCO_3$ and also due to clays such as silicate layers that yield weak Raman spectra (Figure 4. 14).[108,113]

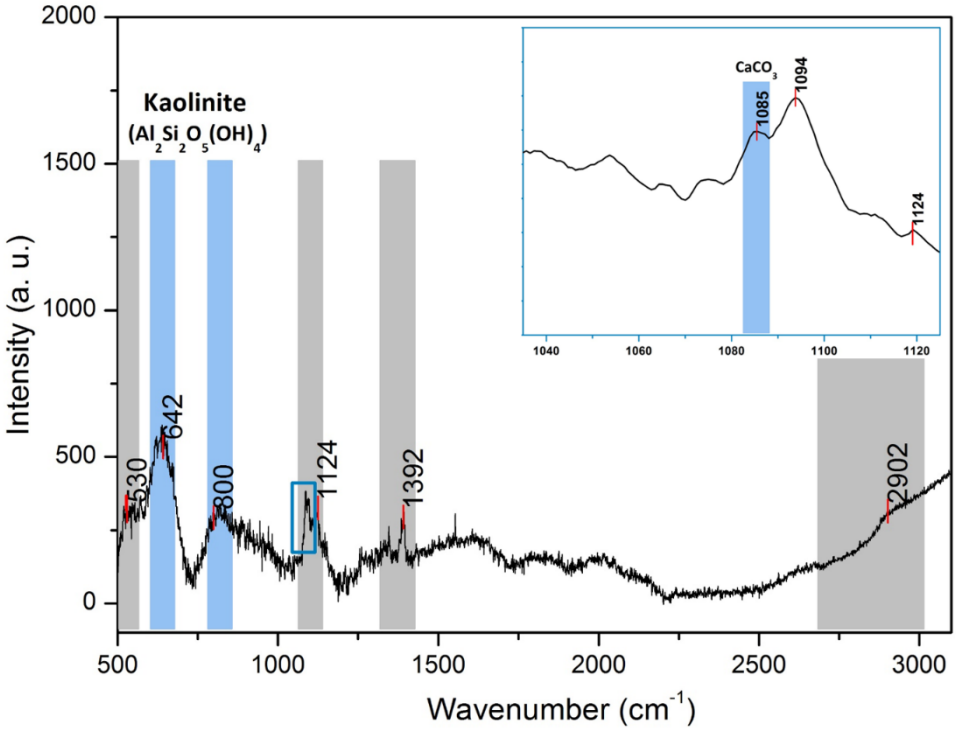

Figure 4. 14|Office paper Raman spectrum. The regions that represent cellulose bonding vibrations are represented in *grey* colour and in *blue* colour are the chemical additives added during paper making process. The *inset* display the $CaCO_3$ band.

Similarly, with what was observed in the Whatman no.1 paper, the office paper also showed some features of cellulose linkage vibrations. Furthermore, it proved the presence of additives from the papermaking process to improve the quality of the product, such as $CaCO_3$ and kaolinite (Figure 4. 14). $CaCO_3$ is only evident at 1085 cm^{-1} band position created by a symmetric stretching vibration of carbonate group, and this band is partially overlapped by a band at 1094 cm^{-1} corresponding to the stretching vibration of β-glycosidic linkage of cellulose (*inset* of Figure 4. 14).[107]

The presence of kaolinite was perceived at 642 and at 800 cm^{-1} that represents mixed SiO deformations, and, octahedral sheet vibrations and Si-O-Al group-vibrations, respectively.[113]

A less distinct band between 1600-1630 cm^{-1} could be from lignin (aromatic ring stretching vibrations and lignin's C=C and C=O stretching modes are observed). The presence of this organic polymer is normally due to the feedstock of office paper, wood cellulose. Therefore, is possible that a residual amount remains after the chemical process used to withdraw amorphous materials.[39,40,108] These analyses of paper surfaces are in agreement with previous reports in the literature.[107,113]

The presence of Ca, Al and Si with the C and O elements from the EDS spectrum (Figure 4. 11), and the occurrence of vibrational bands at 1085 cm^{-1} from $CaCO_3$, and at 642 and 800 cm^{-1} from kaolinite, in the office Raman spectrum, and their absence in Whatman paper analysis, confirms that these components are present in the office paper contributing for a more compacted surface. The fluorescence problem was mitigated by the addition of the metal NPs, resulting in a promising SERS substrate surface. For characterization purposes the weak signal from paper surfaces is a

disadvantage, yet for paper-based SERS substrates the low background in Raman measurements represents another advantage.

4.6 Paper SERS substrates assays by Raman spectroscopy

After the characterization of the paper-based SERS substrates, the detection performance was evaluated with 2 µL of R6G at several concentrations by Raman measurements. This section aims to determine the optimal parameters regarding the type of paper, metal NPs morphology, as well as the volume of NPs needed to achieve the maximum enhancement.

4.6.1 Paper SERS substrates produced with Whatman no.1 Paper

For a given set of SERS spectra in specific experimental conditions (shape and volume of NPs) it was possible to detect the R6G at several concentrations. This assay resulted in nine sets of R6G spectra. Due to the results extension only the best set is herein. Figure 4. 15 represents R6G SERS spectra in the paper SERS substrate produced in Whatman no.1 paper with 500 µL of AgNSs *drop-casted* in wells of 4 mm diameter. The others sets are illustrated in Appendix IX A-C.

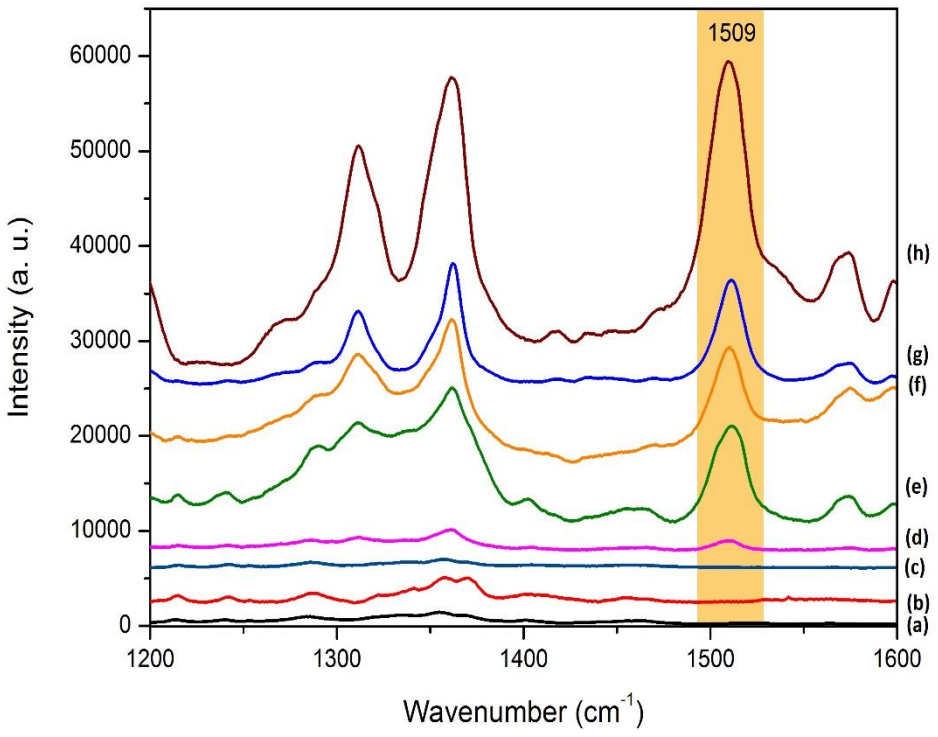

Figure 4. 15|R6G SERS spectra in wells of 4 mm diameter with 500 µL of AgNSs *drop-casted* in Whatman no.1 paper. (a) well without the R6G, *i.e.*, 500 µL AgNSs in Whatman no.1 paper; same well conditions however, with several R6G concentrations added: (b) 10^{-9} M; (c) 10^{-8} M; (d) 10^{-7} M; (e) 10^{-6} M; (f) 10^{-5} M; (g) 10^{-4} M; and (h) 10^{-3} M; signal of R6G appears only starting from wells with the concentration of (d) 10^{-7} M.

Table 4. 3 summarizes the results obtained for 4 mm diameter wells with different NPs volumes (100, 300, and 500 µL), and the three morphology types of NPs studied (aggregated and non-aggregated AgNPs, and, AgNSs). The plus sign (+) represents wells where the signal of R6G was detected, and the minus sign (-), wells where R6G representative bands have not been observed. When both signals are in the same well, it means that although spectra have been displayed

corresponding to R6G, they were not reproducible. Each cell of the table with a sign represents the completion of at least three replicates spectra.

Table 4. 3|Summarized results from paper SERS substrates produced with Whatman no.1 paper (4 mm of well diameter). Results obtained with different NPs volumes: 100, 300 and 500 µL; of the three morphology types of NPs: non-aggregated (*yellow*) and aggregated (*red*) AgNPs, and AgNSs (*blue*). The last table line is the corresponding set of R6G spectra.

R6G		Type of NPs								
Concentration (M)	Amount (ppm)	Non-aggregated AgNPs			Aggregated AgNPs			AgNSs		
		100	300	500	100	300	500	100	300	500
10^{-3}	479	+	+	+	+	+	+	+	+	+
10^{-4}	47,9	+	+	+	+	+	+	+	+	+
10^{-5}	4,79	+	+	+	-	+/-	+	+	+	+
10^{-6}	0,479	-	+/-	+	-	-	-	+/-	+	+
10^{-7}	0,0479	-	+/-	+	-	-	+/-	-	+	+
10^{-8}	0,00479	-	+/-	+/-	-	-	-	-	+	-
10^{-9}	0,000479	-	-	-	-	-	-	-	-	-
Appendix IX (Figure)		A.A	A.B	A.C	B.A	B.B	B.C	C.A	C.B	Figure 4. 15

Firstly, as the volume of added NPs increases, there are several observations to be attained: (1) detection of lower R6G concentrations; (2) higher values of SERS intensity and bands areas (*i.e.* for the same concentration of R6G); (3) reduction of noise and consequently, the spectra are more pronounced (Table 4. 3 and Figure 4. 16). This confirms the previous results (section 4.5.1), which demonstrated a higher density of NPs as the volume of deposition increases. Thus, more NPs at the paper surfaces corresponds to increased sensitivity in the detection of R6G.

For non-aggregated AgNPs (data represented in *yellow*), the R6G concentrations between 10^{-3} and 10^{-5} M were always easily detected. A greater sensitivity was observed when the AgNPs volume increased from 100 to 300 µL, however, the increase of 300 to 500 µL allowed a detection of R6G at 10^{-7} M in a more reproducible manner.

The resulted R6G spectra from aggregated AgNPs (data represented in *red*) did not exhibited any features of R6G to concentrations lower than 10^{-5} M. Instead, the spectra evidenced band deviations and new vibrational bands appeared. Even at higher volumes of aggregated AgNPs the spectra showed weaker intensities compared to the non-aggregated AgNPs (Figure 4. 16).

Regarding the AgNSs (data represented in *blue*), the results obtained were similar to the previously stated for the aggregated and non-aggregated AgNPs. Namely, an increase in AgNSs volume reflected an improved R6G sensitivity, reaching a detection limit of 10^{-7} M with 500 µL of AgNSs added to the Whatman no.1 paper. More importantly, the R6G spectra with AgNSs revealed very high, and reproducible, SERS intensities with minimal noise (Figure 4. 16).

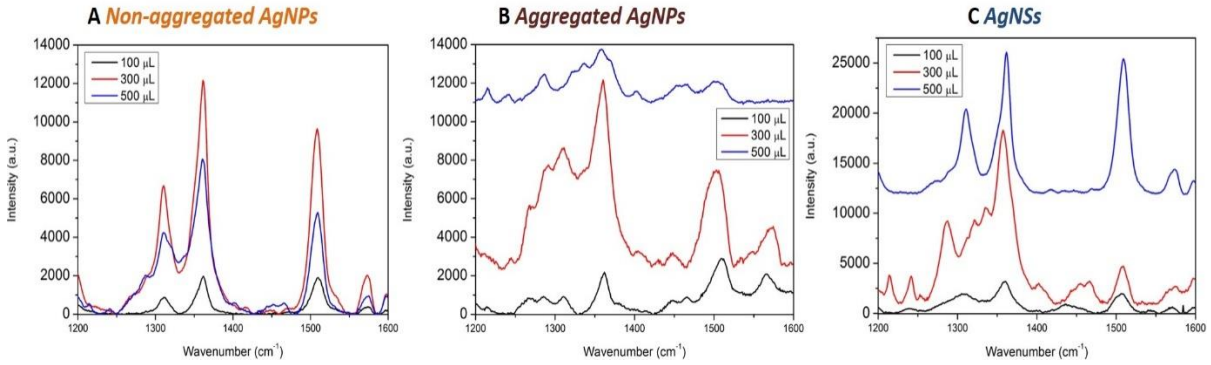

Figure 4. 16|Increase of Raman intensity and area of the R6G bands as the amount of NPs deposited in the well increases. The concentration 10^{-5} M of R6G was chosen to represent. (A) are represented the spectra of non-aggregated AgNPs and (B) the spectra obtained from aggregated AgNPs and finally (C) are the data of AgNSs. The scale of intensity in (A) and (B) is 0-14 000 a.u. and in (C) is 0-27 500 a.u.

4.6.2 Paper SERS substrates produced with office paper

The procedure for the paper SERS substrates produced with office paper was the same as for Whatman no.1 paper. This assay, also resulted in 9 sets of R6G spectra. Due to the results extension only the best set is herein. Figure 4. 17 represents R6G SERS spectra in the paper SERS substrate produced in office paper with 500 µL of AgNSs *drop-casted* in wells of 4 mm diameter. The others sets are illustrated in Appendix IX A-C.

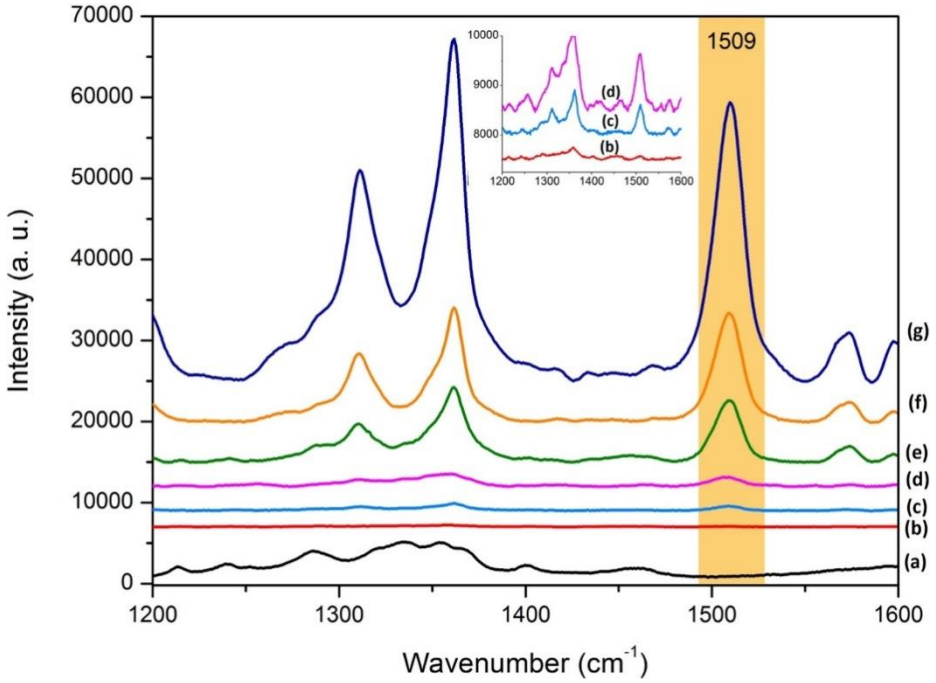

Figure 4. 17|R6G SERS spectra in wells of 4 mm diameter with 500 µL of AgNSs *drop-casted* in office paper: (a) well without the R6G, *i.e.*, 500 µL AgNSs in Whatman no.1 paper; same well parameters and with several R6G concentrations added: (b) 10^{-9} M; (c) 10^{-8} M; (d) 10^{-7} M; (e) 10^{-6} M; (f) 10^{-5} M; and (g) 10^{-4} M; The R6G at concentration of 10^{-3} M could not be observed due signal saturation;

Similarly, to Whatman no.1 paper, the deposited non-aggregated AgNPs and AgNSs on office paper exhibited the same behaviour. Namely, the more the added volume of NPs, the greater the signal of R6G decreasing the value of the minimum detectable concentration (Figure 4. 18).

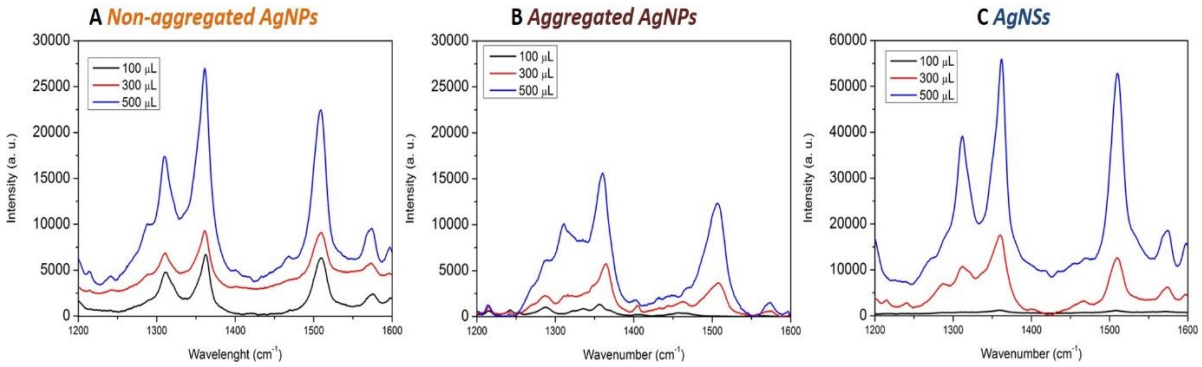

Figure 4. 18|Increase of Raman intensity and area of the R6G bands as the amount of NPs deposited in the well increases. The concentration 10^{-5} M of R6G was chosen to represent. (A) are represented the spectra of non-aggregated AgNPs and (B) the spectra obtained from aggregated AgNPs and finally (C) are the data of AgNSs. The scale of intensity in (A) and (B) is 0-30 000 a.u. and in (C) is 0-60 000 a.u.

Comparing both papers, office and Whatman no.1 papers, the measured spectra for the same experimental conditions had a cleaner signal in office paper, enabling a higher detection sensitivity (Table 4. 4).

Table 4. 4|Summarized results from paper SERS substrates produced with office paper (4 mm of well diameter). Results obtained with different NPs volumes: 100, 300 and 500 µL; of the three morphology types of NPs: non-aggregated (*yellow*) and aggregated (*red*) AgNPs, and AgNSs (*blue*). The last table line indicates the corresponding figure of set of R6G spectra.

R6G		Type of NPs								
Concentration (M)	Amount (ppm)	Non-aggregated AgNPs			Aggregated AgNPs			AgNSs		
		100	300	500	100	300	500	100	300	500
10-3	479	+	+	+	+	+	+	+	+	+
10-4	47,9	+	+	+	+	+	+	+	+	+
10-5	4,79	+	+	+	+	+	+/-	+	+	+
10-6	0,479	+/-	+	+	+	-	-	-	+	+
10-7	0,0479	-	+/-	+	-	-	-	-	+	+
10-8	0,00479	-	-	+	-	-	-	-	-	+
10-9	0,000479	-	-	-	-	-	-	-	-	+
Appendix X (Figure)		A.A	A.B	A.C	B.A	B.B	B.C	C.A	C.B	Figure 4. 17

Considering the non-aggregated AgNPs (data represented in *yellow* in Table 4. 4) a lower detection limit was achieved in office paper compared to Whatman no.1 paper, more precisely, it reached a value 10 times smaller (10^{-8} M) in a completely reproducible manner.

The R6G signal in the SERS substrates with the aggregated AgNPs was only exhibited at high concentrations (>10^{-5} M). At lower concentrations of R6G the spectra showed the same interference as observed previously to the aggregated AgNPs in Whatman no.1 paper. The results in Table 4. 4 suggests that this interference is stronger as the NPs volume increases. This relates to the increased amount of salt onto the surface of the office paper. Due to its lower porosity, retains more NPs impeding an observable R6G signal (section 4.5.1 - Figure 4. 10).

The results for the AgNSs (data represented in *blue*) in office paper were similar to the formerly stated for the Whatman no.1 paper, *i.e.* high and reproducible SERS intensities with minimal noise. However, for low concentrations (10^{-7}-10^{-9} M), R6G spectra occasionally exhibited

interferences likewise the reported for the aggregated AgNPs. Nevertheless, 500 µL of AgNSs in office paper reflected an improved R6G sensitivity, reaching a detection limit of 10^{-9} M.

For lower R6G concentrations (10^{-7}-10^{-9} M) the spectra revealed interference, *i.e.* new bands that do not correspond to R6G. Contaminants even in a lower concentration, may be present in the sample and can be selectively enhanced through a resonance Raman scattering mechanism, overlapping the bands of the adsorbate under study. Therefore, the positions of the vibrational bands were evaluated and confronted with components that were known to be present on the paper SERS substrate: (1) paper; and (2) reagents used in the NPs synthesis, such as HA and SC. The spectra of paper (Figure 4. 13 and Figure 4. 14) and citrate (Figure 4. 19-A) were analysed according to the standard Raman spectrum. The citrate oxidation products (acetonedicarboxylic and acetoacetic acid) and HA were searched in the literature. The SERS signal of the residual nitrate (NO_3^-) from the $AgNO_3$ (the starting material for NPs synthesis) was also compared to the literature. However, the NO_3^- did not shown apparent signal.[114]

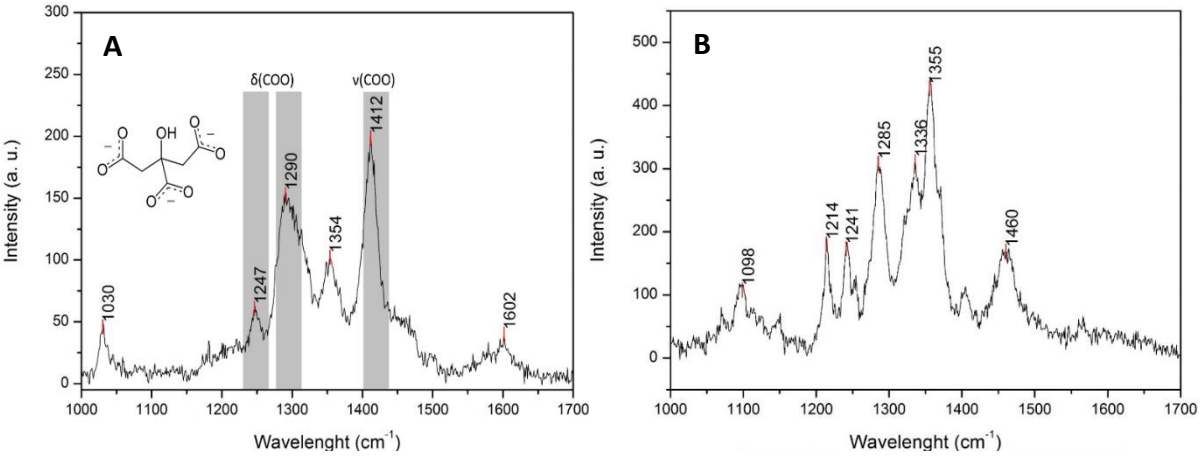

Figure 4. 19|Raman spectrum of citrate and an example of a SERS spectrum with the observed anomalous bands. (A) Raman spectrum of SC (2.2 mM). Regions representative of citrate bonding vibrations are in *grey* colour. *On the top* of the *grey* area are indicated the type of vibrational modes. The chemical structure of citrate is displayed in the inset (*adapted from*[115]). (B) The anomalous bands outlined above are represented and show similar correspondence with Raman spectrum of citrate.

Figure 4. 19 compares the Raman spectrum of citrate and a SERS spectrum with the observed interferences. The corresponding vibrational band assignments are summarized in Table 4.5.

Table 4. 5|Vibrational bands assignments for citrate and correspondences to the observed anomalous bands.[96,116]

Experimentally observed bands (cm^{-1})				Assignment
Citrate	**Strength**	**Anomalous bands**	**Strength**	
1030	w	-	-	
-	-	1098	w	
-	-	1214	m	CO stretching mode from tertiary alcohol
1247	w	1241	m	Carboxylate deformations (COO)
1290	s	1285	s	
-	-	1336	vs	
1354	m	1355	vs	
1412	vs	1414	vw	Carboxylate symmetric stretching mode from citrate (COO)
-	-	1460	s	
1602	vw	-	-	

The bands in Raman spectrum of citrate (Figure 4. 19-A), are consistent with published values.[96,116] The region with band positions at 1336 and 1355 cm^{-1}, are also reported by several authors however, the bands have not been assigned to any vibrational mode. These band regions are displayed at low concentrations of analyte overlapping its signal. The slight deviations between the two spectra may be indicative of interactions between the carboxylates and the Ag surface.[116] Nevertheless, the SERS spectra of the observed anomalous bands can be clearly attributed to citrate, since they correlate very well with the Raman spectrum of citrate in aqueous solution.

The bands related to the appearance of citrate oxidation products were not identifiable hence, is possible that they do not interfere in R6G SERS spectra.[117] Likewise, when comparing the HA spectrum from literature with the spectrum shown in Figure 4.19-B, there were no correspondences.[95] The absence of HA is consistent with the appearance of the same bands for the wells in which aggregated AgNPs and AgNSs were deposited. The synthesis of aggregated AgNPs, conversely to the AgNSs did not needed the presence of HA. Therefore, the anomalous bands can only be from a common molecule, the citrate.

The presence of interferences in paper SERS substrates highlight the importance of the interpretation of the spectra profiles, even before the addition of the analyte.

4.6.3 Enhancement factor between the different paper SERS substrates

The areas of the band at 1509 cm^{-1} (obtained by a peak fitting method) from R6G SERS spectra at several concentrations were used to calculate the AEF values. Two sets of three histograms show the average AEF values with their respective standard-deviations (SD). It is only displayed the calculated values for the cases where reproducible detection R6G could be perceived (Figure 4. 20). The colour code is explained in the legend of the figure.

A greater amount of NPs led to spectra with the most intense bands and with higher areas. Therefore, due to a dependence of the AEF calculation on the band areas, it follows that the value of AEF increases similarly.

It is also worthwhile to note that an increase in the concentration of R6G, leads to a smaller value of AEF (Figure 4. 20). This behaviour may be related to the actual method of calculating the value of AEF. The calculation of AEF assumes that all molecules contribute equally to the Raman signal. However, the observed SERS signal is essentially originated from a small group of molecules

located in *hot spots,* experiencing much larger enhancements (areas where the enhancement >10^9). In terms of proportion, as the concentration increases, the percentage of molecules that experience this type of enhancement is smaller. Consequently, the molecules away from *hot spots* may partly conceal the signal of molecules in these locations thereby decreasing the value of AEF. If it were possible to position all the molecules in these *hot spots*, then a much greater enhancement could be obtained.[19]

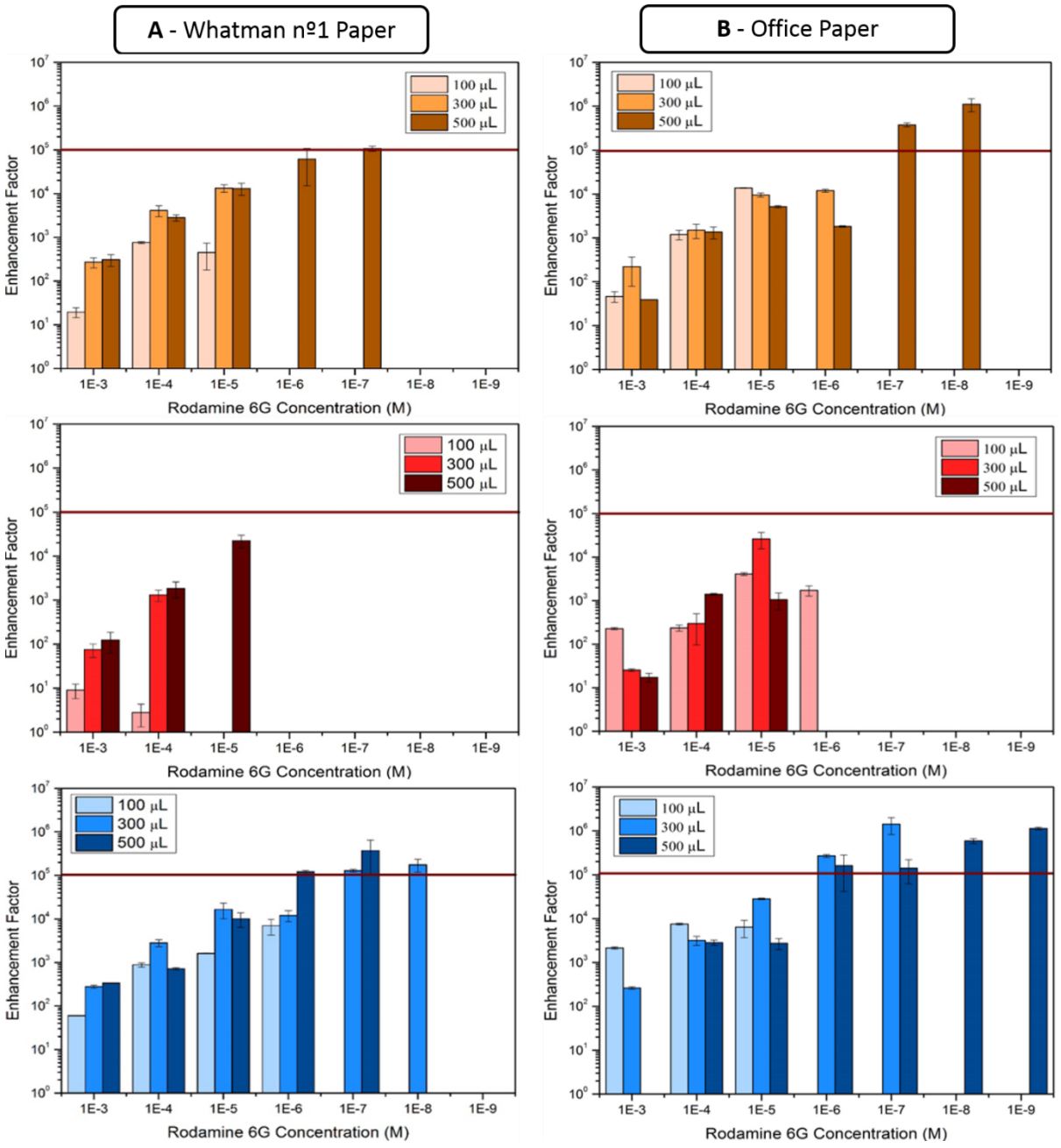

Figure 4. 20|AEF values from the paper SERS substrates produced: (A) in Whatman no.1 paper and (B) office paper. The *yellow* histograms represent the results from non-aggregated AgNPs, in *red* are presented the aggregated AgNPs outcomes and finally, in *blue* are the AEF values from AgNSs. Each AEF value represented in the histogram is an average of three calculated values from three different locations of the SERS substrates with their respective SD.

Aggregated AgNPs under the experimental conditions herein, revealed the NPs as unsuitable for the paper SERS substrates due to the difficulty in obtaining a R6G signal, and the visualization of citrate bands. In order to overcome this problem other aggregating agents could be used. However, the interaction with the aggregating agent and the colloid (for example depending on the presence

and monovalent and divalent anions) and consequently the analyte-NPs interaction may vary, resulting in enhancement discrepancies. In fact, Yaffe *et al.* found that the in an aggregated colloid with NaCl presence, the band patterns for the citrate did not disappear after addition of the analyte, conversely to the other aggregating agents studied.[96] Therefore, while the Cl^- ions do not interfere with the spectrum, NaCl it was found as an inappropriate aggregating agent for the type of SERS substrate used in this project.[97]

There are also aggregation methods by centrifugation processes and ultrasonication.[116] However, although the aggregations may sometimes provide excellent SERS signals, its low reproducibility level of uncontrolled aggregation results in in a discrepancy in the SERS efficiency, which limits their use.[116]

The AEF values with non-aggregated AgNPs were surprisingly higher than expected, reaching an AEF value such as 10^6 and 10^5 in office and Whatman no.1 papers, respectively. When the paper SERS substrates were analysed by SEM, it was observed aggregates of NPs, which assemble as the silver colloid solution dries (section 4.5.1). This aggregation causes small NPs clusters with irregular structures. The decrease gap size among adjacent AgNPs provides huge electric fields. Moreover, the clusters cause the LSPR band to extend into the red and IR.[36] Additionally, the remaining negative charges on the Ag surface facilitated R6G cations to adsorb to the NPs.[116] Therefore, a greater number of *hot spots* leaded to a superior average AEF values and lower detectable concentrations.[20] Thus, the non-aggregated AgNPs may be presented as a possible alternative to obtain easily manageable nanoclusters, rather than aggregation with salt, nevertheless, it is also a method that lacks proper control.

Comparing the three morphologies of NPs, the AgNSs allowed higher AEF values and provided a higher sensitivity (achieving 10^{-8} and 10^{-9} M for the Whatman no.1 and office paper, respectively). Recalling the results obtained with SEM (section 4.1.3), the degree of anisotropy was greater for AgNSs than for the other two NPs morphologies. This degree of anisotropy is intrinsically related to the number of *hot spots* contributing to the overall signal. As aforementioned, the *hot spots* are located in the sharp protrusions of the stars, and between the junctions of two particles.[9] Higher number of *hot* spots *per* particle leads to higher band areas in the SERS spectra, and thus, the AEF values increases.

In addition, the space in the *hot spots* must be considered. The spaces among AgNPs clusters are very small due to its nonuniformity which allows the adherence of small molecules like R6G, but block macromolecules. In opposition, the interstitial gaps between arms of AgNSs may host the large macromolecules allowing their enhanced detection.[101]

Another characteristic that differentiates AgNPs and AgNSs in SERS efficiency is the wavelength excitation dependence. The best spectral location of the LSPR for maximum electromagnetic enhancement according to E^4 enhancement approximation, is coincident with the laser excitation wavelength. Although this is not entirely proved due to several studies that reported systems where LSPR λ_{max} did not coincide with the greatest SERS enhancement.[17,102] The AgNSs with different numbers of arms and tip sharpness leads to very distinct LSPR, in the opposite side there is a single LSPR band with a low broadening for the AgNPs, which can explain the higher enhancement (see Figure 4. 5).[19]

In summary, increasing the concentration of NPs improves the sensitivity toward R6G and provide higher AEF values. The best obtained results were for 500 µL of AgNSs added to office paper. The lack of reproducibility sometimes verified in the paper SERS substrates under particular experimental conditions (volumes <500 µL) might be related to the locations where the NPs concentration do not cover entirely the cellulose fibers. The aggregated AgNPs and sometimes AgNSs demonstrate the citrate bands-profile making difficult or even impossible to detect R6G.

The AgNSs provide larger AEF values and smaller detectable concentrations congruently expected due to the number of *hot spots per* particle as well as the variety of possible LSPR including the excitation laser length region (*vide infra* Figure 4. 4). Because AgNSs have arms of different

lengths, it would be normal for the SERS signal to suffer a great variation. However, SERS measurement includes an average of several AgNSs reducing the variation in plasmonic enhancement, and hence, leads to low SD of the AEF values. As a result, this type of paper SERS substrates reveals intra-well[5] reproducibility.[30,84,88]

The difference between the results obtained from Whatman no.1 paper and office paper relates to the three dimensional structure of cellulose fibers. The lowest porosity of the office paper allows a better surface with more NPs. Thus, the porosity of the paper is a key-factor in the SERS signal obtained by these substrates. In addition, in Raman spectroscopy the relative band intensities of cellulose depend on the polarization of the incident light due to the orientation of microfibers. Due to a more pronounced different orientation of cellulose fibers in Whatman no.1 paper, irreproducible Raman signals were more often observed.[111]

4.6.4 Optimization of paper SERS substrate

One of the factors limiting the production time of the SERS substrate, is the time that the droplets take to dry after deposition (≈8 h). In order to reduce this time, the dimension of the wells was diminished from 4 mm to 2 mm. The decrease in the volume of the sample used was proportional to the reduction in the size of the well, leading to a drying time of ≈4 h. Hence, the optimized paper SERS substrate have wells of 2 mm diameter with 62.5 µL of AgNSs *drop-casted* in office paper.

Subsequently, several treatments were proceeded onto the paper SERS substrates for removing or oxidizing the capping agent citrate from the AgNSs. The following table express the type of procedure executed (Table 4. 6).

Table 4. 6|Summary of the treatments performed on the paper SERS substrates to remove or oxidize the citrate, the capping agent of the AgNSs used in this type of substrate.

Treatment	Function	Reference
Centrifugation	Lower the concentration of citrate	[116]
Basic H_2O	Wash of the citrate	[114,116]
$FeCl_2$	Oxidizing agent	[118]
H_2O_2	Oxidizing agent	[119]
H_2O_2 + $FeCl_2$	Oxidizing agent	[119]
HCl	Wash of the citrate by charge screening	[114]

The procedure for the three cycles of centrifugation and water washing was used for eliminating the excess of surface charges provided by citrate anions. Another approach to wash the citrate passed through applying basic water to the wells with the AgNSs deposited.[114,116]

With the intention of decreasing the SERS signal from the citrate, oxidizing agents were added to the paper SERS substrates, namely, $FeCl_2$, H_2O_2 and HCl. $FeCl_2$ forms complexes with the citrate (for citrate is a known iron chelator).[118] A combination of $FeCl_2$ and H_2O_2 generates the hydroxyl radical ($^{\bullet}OH$), an electrophile and strong oxidizing agent, which reacts with most organic compounds.[119] Finally, HCl was used to undergo in a competitive adsorption with the existing citrate for the Ag surface (even in lower concentrations used for aggregation). Since Cl^- is less soluble than citrate, the surface AgCl has a higher thermodynamic stability, making difficult to displace Cl^- from the Ag surface.[114]

The resulted SERS spectra from the several treatments performed are represented in Figure 4. 21. Except for the spectra with 10 mM of $FeCl_2$ and 2 M of HCl (Figure 4. 21.(c) and (i)), the intent effect was not accomplished, *i.e.,* the treatment was not sufficient for a successful inhibition of citrate signal. For the treatments with $FeCl_2$, the concentration of 10 mM proved to be efficient to

[5] The term "intra-well" refers to different locations within the same well.

prevent the citrate signal, however when $1.5x10^{-2}$ M of malathion was added, it did not reveal the expected spectrum, probably because the iron layer in the paper SERS substrate prevents the access of the malathion molecules. The HCl was relatively efficient with just two washes, however, when $1.5x10^{-2}$ M of malathion was added, it did not reproduce any signal from malathion. In fact, only revealed interferences by citrate (see Appendix XI). Therefore, the treatments performed herein to eliminate or mitigate the citrate SERS signal, were not successful.

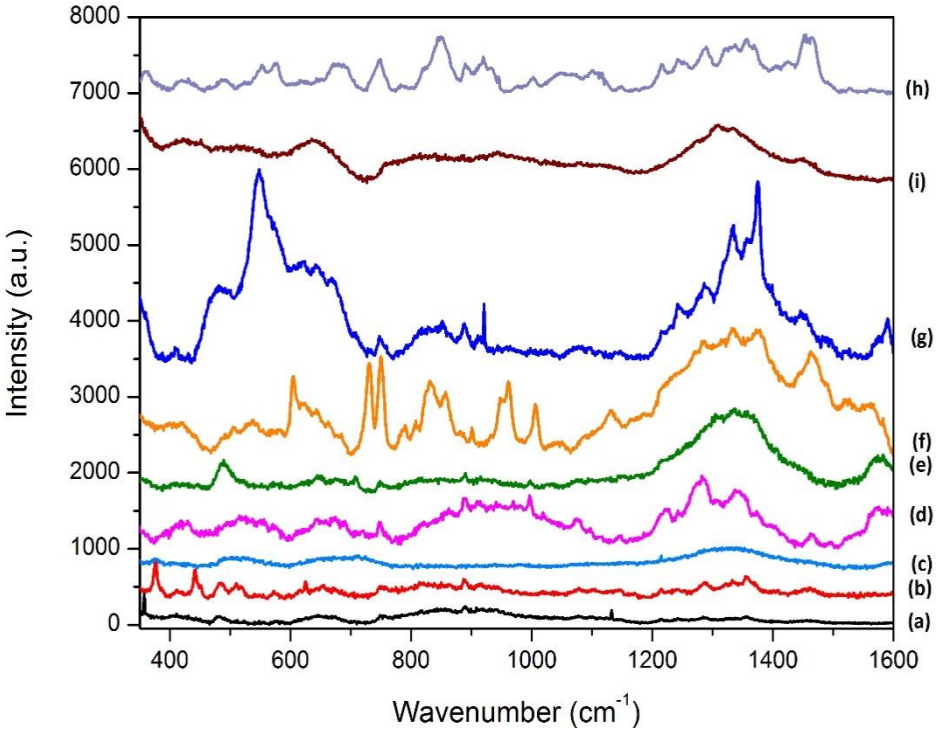

Figure 4. 21|SERS spectra of the wells submitted to several treatments onto the paper SERS substrates with the aim of removing or oxide the capping agent citrate from the AgNSs: (a) one wash with basic water; (b) two wash with basic water; (c) 10 mM of $FeCl_2$; (d) 1 mM of $FeCl_2$; (e) 3% of H_2O_2; (f) 100 mM of H_2O_2; (g) 1 mM of $FeCl_2$ and 100 mM of H_2O_2; (i) wash twice with 2 M of HCl and (h) three cycles of centrifugation. All the treatments show interferences being the (c) and (i) the procedures with less background signal. These interferences show some correspondence with citrate but they also present bands of unknown origin.

4.7 Detection and limits of detection and quantification of several analytes

4.7.1 Rhodamine 6G

The sensitivity and the limit of detection (LOD) are criteria for judging the qualities of a detection method. To evaluate the sensitivity of the paper SERS substrate, different concentrations of R6G from one stock solution were measured. A correlation between SERS band areas and concentration was observed within the concentration range from 10^{-3} to 10^{-9} M. The plot in Figure 4. 22 represents the mean of three measurements for each well and the error bar for each data point is the SD of the area signal. As shown previously in Figure 4. 17, the area of the SERS line at 1509 cm^{-1} due to C-C stretching vibration is highly sensitive to the concentration of R6G.

The data points were fitted with a Langmuir isotherm ($r^2 = 0.998$). The Langmuir isotherm describes the chemical equilibrium of the interaction between R6G and the SERS substrate. Is also based on the assumption that there exist a limit number of potential surface binding sites on the AgNSs. When the analyte is added in high concentrations, the surface of the paper SERS substrate becomes saturated. In this situation the substrates reached its maximum loading capacity, and the SERS signal do not increase and remains approximately constant. Saturation occurs when the R6G

concentration exceed 10^{-4} M. In this area SERS serves only as a qualitative method for recognizing the analyte.[26,120] At low concentrations, the band area increases linearly with concentration (Equation 4.4) where y corresponds to the analytical area from the band at 1509 cm^{-1} ($AA_{1509\,cm^{-1}}$), and x the R6G concentration (C_{R6G}). The linear correlation in the range 10^{-6}-10^{-9} M was used to determine the limit of detection (LOD), sensitivity (slope of the working curve), and the linearity (r^2) from LOD to 10^{-6} M:

$$AA_{1509\,cm^{-1}} = (112 \pm 9) \times 10^{9} C_{R6G} + (176 \pm 4) \times 10^{2} \qquad \textit{(Equation 4.4)}$$

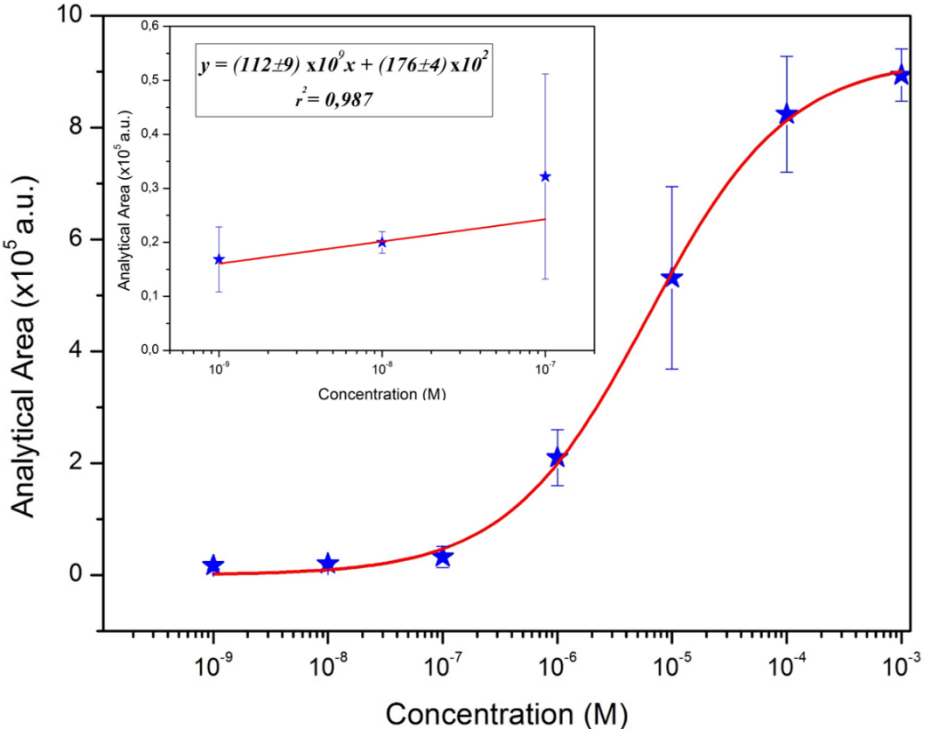

Figure 4. 22|Correlation between SERS band areas and logarithmic R6G concentration. Plots of analytical area *versus* R6G concentration for the band at 1509 cm^{-1}. Data is fitted using the Langmuir isotherm. Each data point represents the average value from three SERS spectra. Error bars show the SD.

The LOD of optimized SERS substrate can be defined as the lowest concentration at which a distinguished R6G SERS spectrum can be obtained.

The LOD can be calculated using Equation 4.5, where σ_b is the SD of the background signal. The background signal refers to the SERS area from a sample with R6G concentration equal to zero, and helps to set the limit for separation of a positive detection from a negative detection. m, is the slope of the calibration curve.

$$LOD = \frac{3\sigma_b}{m} \qquad \textit{(Equation 4.5)}^{75,77}$$

Therefore, the LOD could be determined to be 0.17 ± 0.04 ppb.

The limit of quantification (LOQ) is based on the maximum acceptable relative standard deviation, commonly 10 %, of a reported value. LOQ is calculated using Equation 4.6, where $\mu_b$is the average of the background signal, and σ_b is again the same standard deviation.

$$LOQ = \mu_b + 10\sigma_b \qquad \textit{(Equation 4.6)}^{75,77}$$

Dividing the LOQ by the slope of the calibration curve,m, produces a LOQ of 2.5 ± 0.5 ppb.

4.7.2 Malathion

4.7.2.1 Raman spectrum of malathion

To illustrate the use of this practical and portable SERS substrate for field-based applications, a detection of malathion was performed. Malathion is a commonly used organophosphate pesticide that threat human and animal health through residual contamination of food.[64] Before the malathion detection assay, the Raman spectrum of the pure compound was obtained allowing the tentative assignments of the analyte (Figure 4. 23).

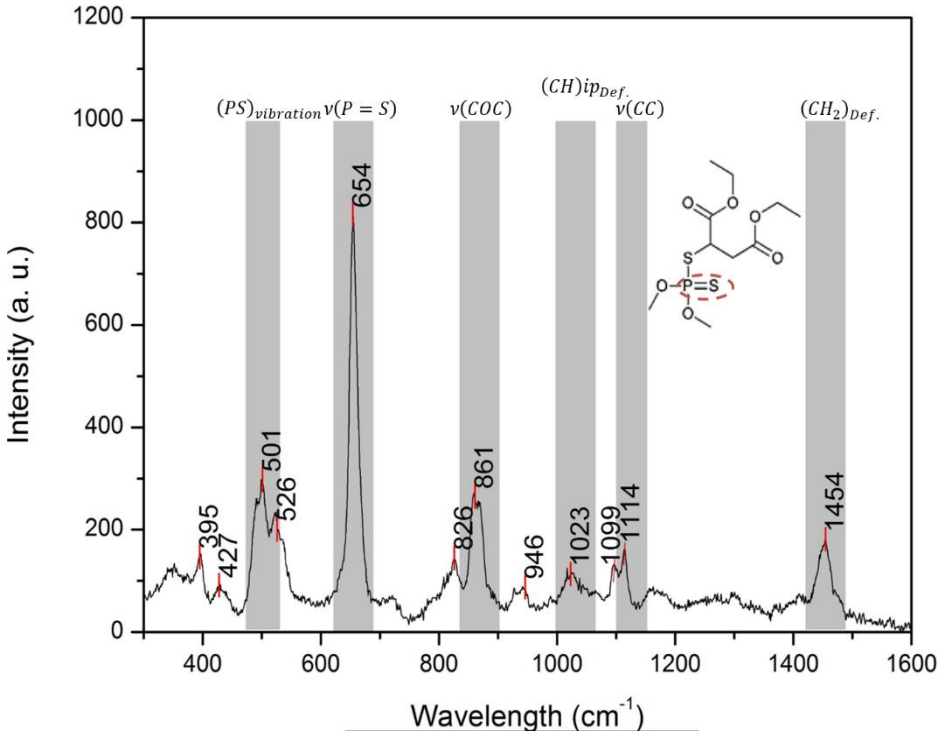

Figure 4. 23|Raman spectrum of malathion. The regions that represent the main malathion vibrations are in *grey* bars. *On the top* of the *grey* area are indicated the type of vibrational modes. The chemical structure of malathion is display in the inset (a*dapted from*[121]).

The corresponding vibrational band assignments are summarized in Table 4. 7. The most important feature in the malathion Raman spectrum is the thiophosphoryl bond (P=S) that displays a strong band at 654 cm^{-1}, therefore, this band can serve to quantify the given compound.

Table 4. 7|Vibrational bands assignments for malathion.[74,122]

Experimentally observed bands (cm^{-1})	Strength	Assignment
501	w	P=S vibration
654	vs	P=S vibration
861	m	C-O-C stretching mode
1023	s	C-H in-plane deformation
1114	w	C-C stretching mode
1454	m	CH_2 deformation

4.7.2.2 SERS assay of malathion

To assess the malathion detection performance, several concentrations of malathion were directly applied to the paper SERS substrate. The detection performance for malathion is presented in Figure 4. 24, and the spectra indicate that the P=S bond is in close proximity to the silver surface, which can be observed from the band at 653 cm^{-1}.[96]

The SERS spectra obtained from the malathion are in good agreement with previous reported spectra from both, conventional Raman and SERS, spectra by other groups.[33,74,81] Nevertheless the unambiguously identification of the pesticide was not straightforward due to the interferences from the citrate originated form the capping of the deposited AgNPs (see section 4.6.2). The malathion molecule is an anion, and consequently, might establish a direct competition with the citrate. The resulting signal will depend on which specie occupy the surface sites and are enhanced. Although Ag has a strong affinity towards sulphur, the concentration of citrate may be too high to the malathion signal, which at lower concentrations does not exceed the citrate signal. The result was an indistinguishable signal of the added analyte at lower concentrations.[114,123]

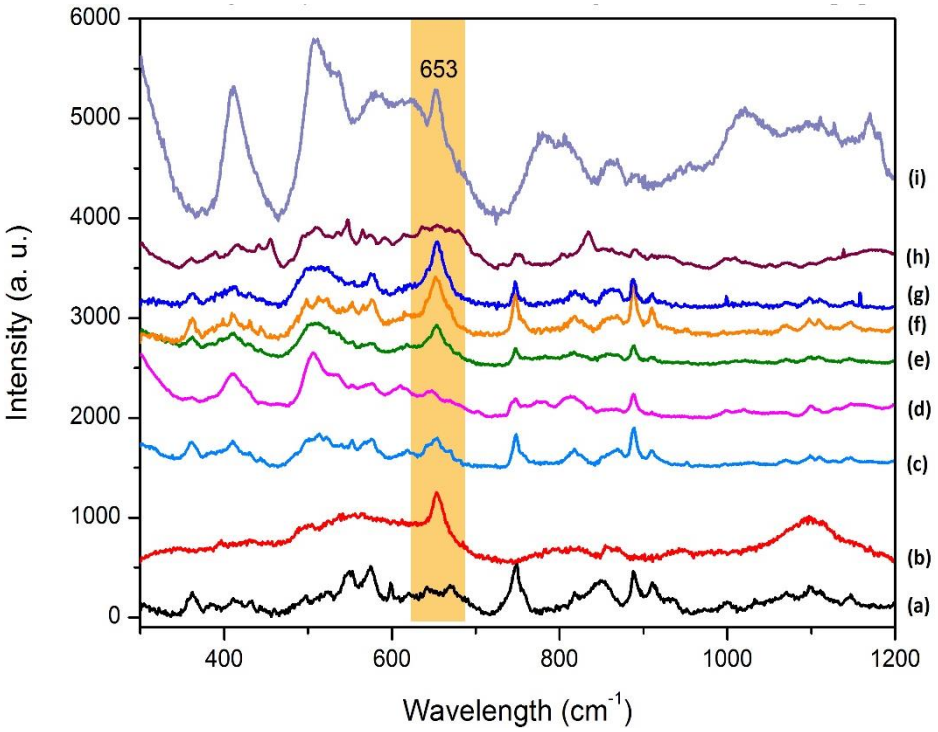

Figure 4. 24|Malathion SERS spectra in the optimized paper SERS substrates. (a) well without malathion, *i.e.*, 62.5 µL AgNSs in office paper; (b) pure malathion Raman spectrum (3.72 M). Same experimental conditions with several malathion concentrations added: (c) $1.5x10^{-2}$ M; (d) $2x10^{-2}$ M; (e) $2.5x10^{-2}$ M; (f) $3x10^{-2}$ M; (g) $3.5x10^{-2}$ M; and (h) $3x10^{-1}$ M; (i) 3.72 M.

The sensitivity of the SERS substrate toward malathion was evaluated by different concentrations from one stock solution. A correlation between SERS band area at 653 cm^{-1} and concentration was observed within the concentration range from $1x10^{-2}$ to 3.72 M. The plot represents the mean of three measurements for each well and the bar error for each data point is the SD of signal area (Figure 4. 25).

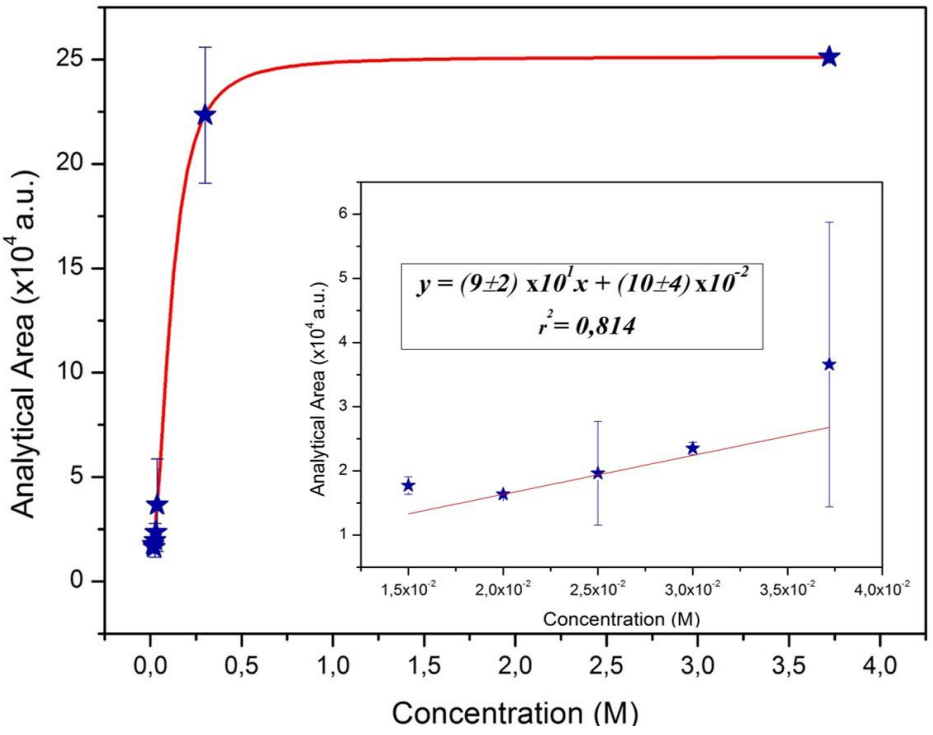

Figure 4. 25|Correlation between SERS band areas and malathion concentrations. Plots of analytical area *versus* malathion concentration for the band at 653 cm^{-1}. Each data point represents the average value from three SERS spectra. Error bars show the standard deviations.

This data was fit by a Langmuir isotherm where r^2, the coefficient that represents the goodness of the fitting, is 0.999. Although the r^2 suggests that quantitative detection of malathion can be performed using these SERS substrates, the areas obtained at concentrations lower than 3.7×10^{-2} M shows some overlapping hindering a reliable quantitative analysis.

At low concentrations, the band area increases linearly with the malathion concentration:

$$AA_{653\ cm^{-1}} = (9 \pm 2) \times 10^{1} C_{Malathion} + (10 \pm 4) \times 10^{-2} \qquad \textit{(Equation 4.7)}$$

The linear correlation allows to determine the LOD and LOQ as aforementioned by Equation 4.5 and Equation 4.6. The detection and quantify limits, of $(2 \pm 1) \times 10^{3}$ ppm and of 3944 ± 7 ppm, were achieved by this type of paper SERS substrate.

4.7.3 Domoic Acid

4.7.3.1 Raman spectrum of domoic acid

The main features of the Raman spectrum of DA were obtained in a similar manner (Figure 4. 26). The tentative assignments of the Raman bands were based on the Djaoued *et al.* work and are listed in Table 4. 8. Djaoued compared the DA spectrum with spectra from the structurally related aminoacids (alanine, glycine, proline and glutamic acid).[58]

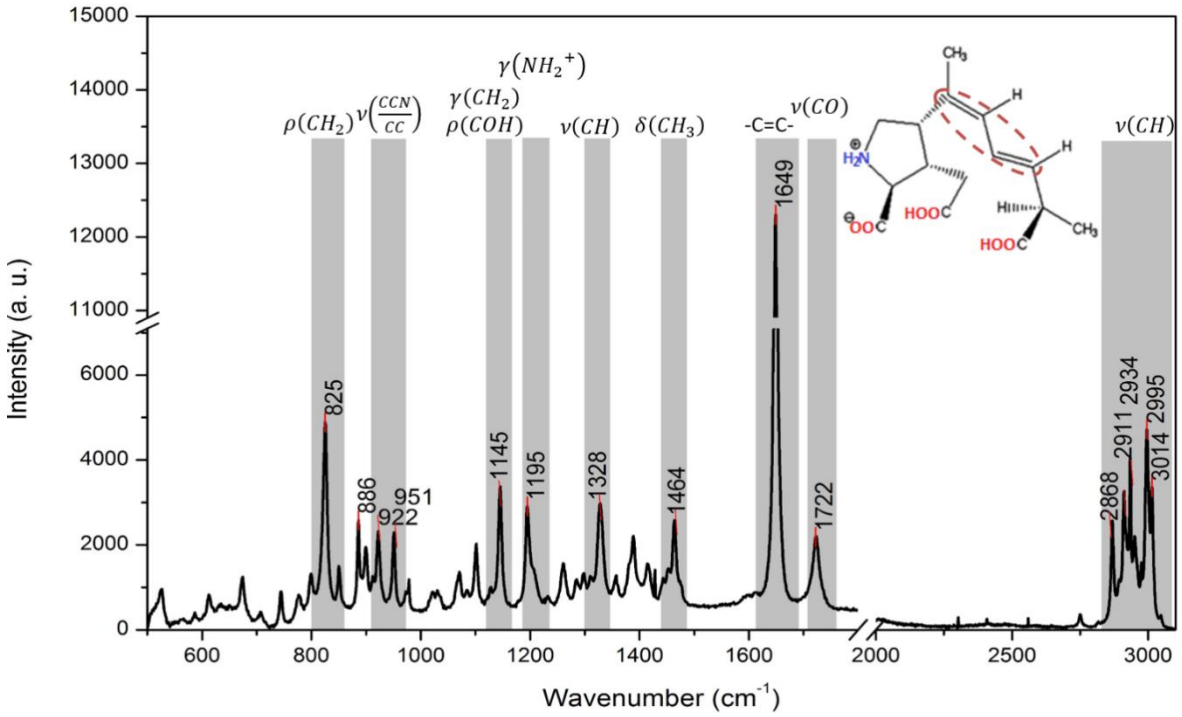

Figure 4. 26|Raman spectrum of DA. The regions that represent the main DA vibrations are in *grey* colour. *On the top* of the *grey* area are indicated the type of vibrational modes. The chemical structure of DA is display in the inset (*adapted from*[58]).

The strongest band occurs at 1649 cm^{-1} which was assigned to the stretching vibration of the conjugate bond C=C in the side chain of DA. This DA vibration is exclusively Raman-active and IR-inactive (see Figure 4. 26). The determination of the concentration of DA in aqueous solutions was performed with this band due to its very strong intensity.

Table 4. 8|Raman spectroscopic data with assignments for DA.[12,50,58,77]
Abbreviations: ν: sym./asym. stretching; δ: scissoring/bending; τ: twisting (out of plan bending); ρ: rocking (in-plane bending); γ: wagging modes;

Frequency (cm^{-1})	Strength	Assignments	Frequency (cm^{-1})	Strength	Assignments
527	vw	γCOO^-	1195	w	γNH_2^+
587		γCOO^- and δCOOH	1261	vw	γCH_2^+
613	vw	γCOO^- and δCOOH	1288	w	O-H in-plane deformation
674	vw	δCOO^-	1298	vw	δCH
707	vw		1328	w	δCH
745	vw		1358	vw	τCH_2
777	vw	Skeleton deformation	1389	vw	τNH_2^+
799	vw		1415	vw	νCOO^-
825	m	ρCH_2	1453	vw	δCH_2
850	vw	ρNH_2^+	1464	vw	δCH_3
886	w		1474	vw	δCH_2
899	vw	νCC	1649	vs	-C=C-
912	vw	νCC	1722	vw	νCO
915	vw	ρCH_3	2750	vw	νCH
922	vw	νCCN and νCC	2868	w	νCH
951	vw	νCCN and νCC	2894	vw	
978		γCH_3	2911	w	νCH
1021	vw	νCN	2934	m	νCH
1030	vw	$\nu C\text{-}C(OO^-)$ and νCN	2950	w	νCH
1071	vw	ρCH_2	2975	vw	νCH
1102	vw	νCCN	2995	m	νCH
1145	w	γCH_2 and νCOH	3014	w	νCH

4.7.3.2 SERS assay of domoic acid

In order to obtain the SERS spectrum of DA, a solution of 10^{-2} M was applied onto the paper SERS substrate (Figure 4. 27). Besides the observation at 1653 cm^{-1} indicative of the DA presence, it was not observed any other characteristic band apart from the already mentioned interferences. Hence, the DA molecule do not have a higher affinity to Ag than the citrate. At lower DA concentrations, the signal from the citrate bands, compromises a correct analysis. Therefore, it was not possible to confirm the presence of DA even after the tentative treatments discussed in section 4.6.4.

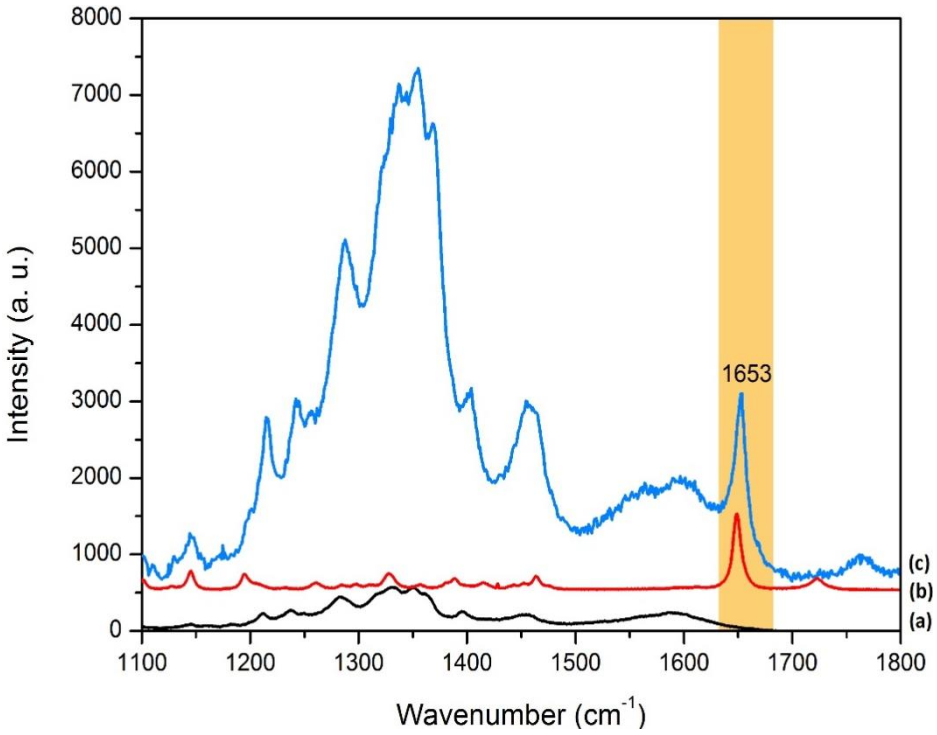

Figure 4. 27|SERS assay of DA on paper SERS substrate. (a) well without DA, *i.e.*, 62.5 µL AgNSs in office paper; (b) Raman spectrum of DA (one crystal). (c) SERS spectrum of 10^{-2} M DA in paper SERS substrate. The characteristic band at 1653 cm^{-1} was observed and the citrate bands appear in the region 1200-1400 cm^{-1}.

4.8 Reproducibility between different synthesis batches

The homogeneity of SERS signals from different wells is another important parameter in evaluating the usefulness of SERS substrates, especially in assessing the potential for mass production. To test the reproducibility of SERS substrates in office paper, three batches randomly selected were used to produce nine wells, and spectra were collected under ambient conditions and three different concentrations were evaluated (10^{-7}, 10^{-8} and 10^{-9} M) (Figure 4. 28).

The reproducibility of the R6G spectra is shown in Figure 4. 28. The main Raman vibrations of R6G for aromatic C-C stretching modes (1310, 1361, 1509 and 1649 cm^{-1}) are obviously enhanced in all batches, indicating good reproducibility. To obtain a statically meaningful result, the relative standard deviation (RSD) was calculated by variation in the 1509 cm^{-1} Raman spot-to-spot area. The RSD of the set with 10^{-9} M of R6G is about 1.7 % (Figure 4. 28-A). The spectra set with 10^{-7} M lie within a 4.4 % variation range and the other (10^{-8} M of R6G) is within 9.6 %, revealing high reproducibility of SERS substrates (Appendix XII – Figure XII. 1 and Figure XII. 2).

Therefore, AgNSs synthesis method could originate uniform nanostructure surfaces over several microns' scale, which leads to homogenous distribution of the resultant of *hot spots* in the project area of the incident laser, and in result, gives rise to highly inter-reproducible SERS responses.

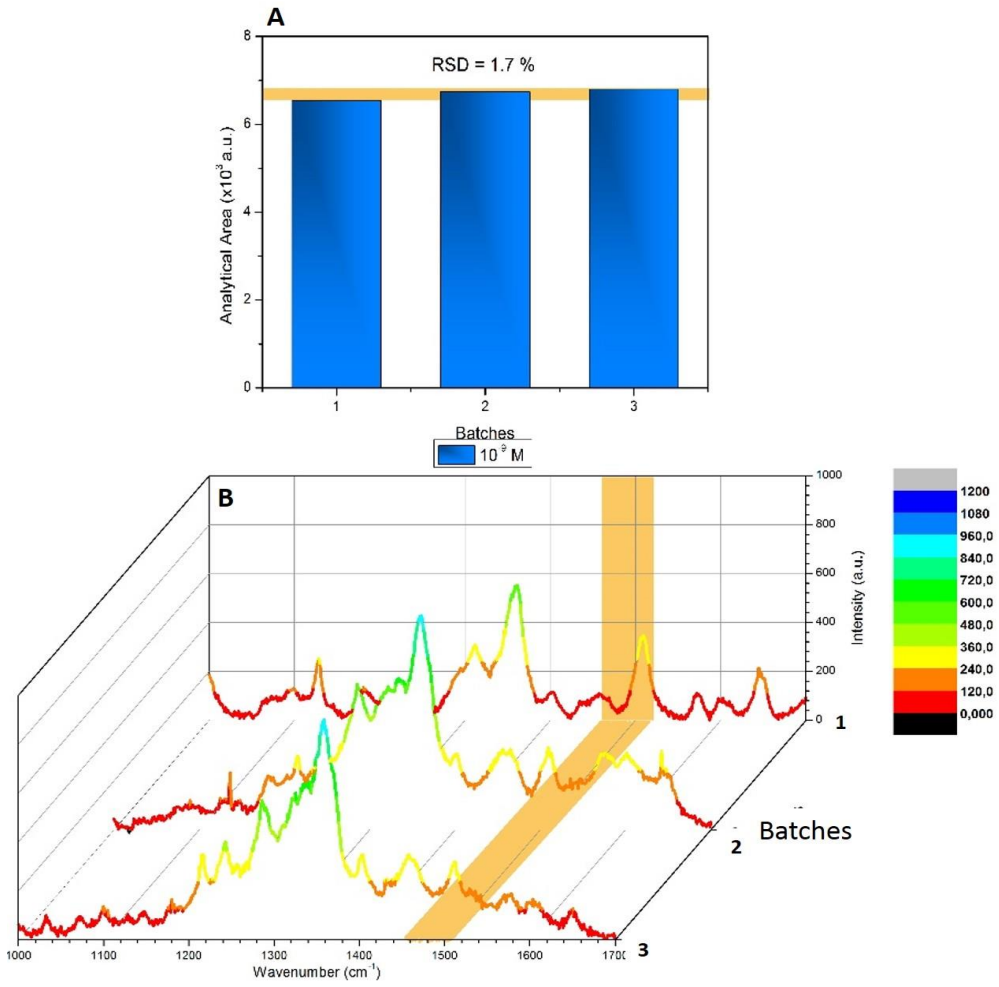

Figure 4. 28|Reproducibility of paper SERS substrate. (A) Area distribution of the 1509 cm^{-1} band in the spectra *versus* the number of batches. Each data point represents the average value from three SERS spectra measured at the vicinity of each spot. The *yellow* bar represents the relative standard-deviation (RSD = 1.7 %). (B) SERS spectra of 10^{-9} M R6G recorded from the optimized SERS substrate fabricated by three different batches of AgNSs colloidal solution. The intensity increase is represented by a colour code, from red to blue.

4.9 Time stability study of the paper SERS substrate

Besides the high sensitivity and good reproducibility, it is also crucial to considerer the stability of paper SERS substrates for field-based detection. For routine SERS analyses, an ideal sensor should be stable for a long period of time. Thus, the stability of the optimized paper SERS substrate was systematically investigated over a period of 5 weeks and between measurements it was stored at 4°C in a desiccator. Three different concentrations were to studies, 10^{-6}, 10^{-8} and 10^{-9} M.

It can be clearly seen from Figure 4. 29 that the profile of SERS spectra after 5 weeks is very similar to the obtained by freshly prepared substrates. Neither a shift in the major Raman bands, nor a significant change in Raman area was observed. The relative standard deviation obtained using the 1509 cm^{-1} band was 7.3 % (*n = 5*) for 10^{-9} M of R6G and the behaviour was similar with concentrations of 10^{-6} (RSD = 10.7 %) and 10^{-8} M (RSD = 13.7 %), suggesting rather stable paper SERS substrate (Appendix XIII – Figure XIII. 1 and Figure XIII. 2).

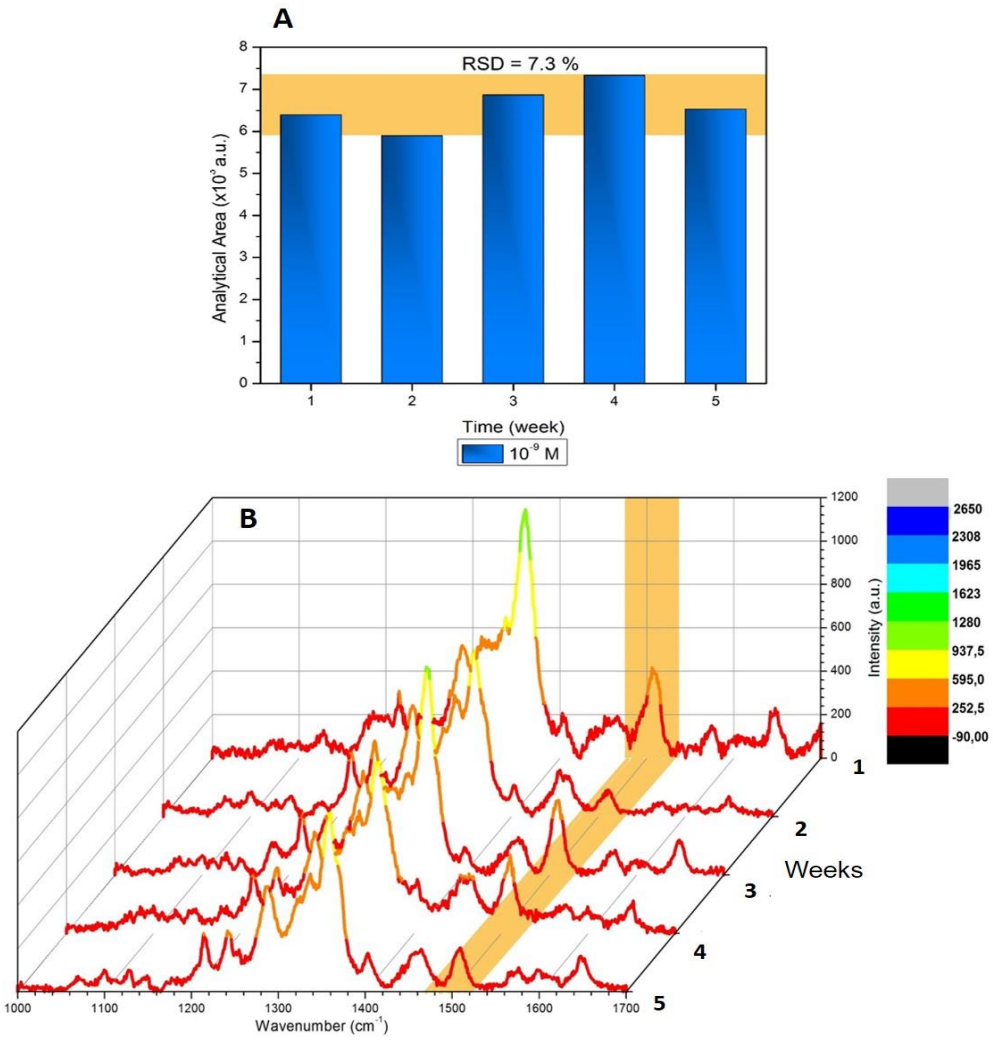

Figure 4. 29|Stability of SERS substrate. (A) Area distribution of the 1509 cm^{-1} band in the spectra *versus* stored time (5 weeks). Each data point represents the average value from three SERS spectra measured at the vicinity of each spot. The *yellow* bar shows the relative standard deviation (RSD = 7.3 %). (B) SERS spectra of 10^{-9} M R6G recorded from the optimized SERS substrate stored for 5 weeks under at 4 °C in a desiccator. The intensity increase is represented by a colour code, from red to blue.

4.10 Measurements of SERS substrates fabricated through physical vapour deposition method

In addition to the paper SERS substrates developed, the SERS efficiency of the several types of PVD SERS surfaces were evaluated, as well as the detection and quantification limits, and field-detection applications.

4.10.1 Detection and limits of detection and quantification of several analytes

4.10.1.1 SERS substrates with monolayer of silver nanoparticles

4.10.1.1.1 Rhodamine 6 G

Araújo *et al.* developed a new PVD SERS substrate composed by self-assembled closed packed arrays of semi-spherical AgNPs deposited by PVD. By depositing a thin layer (≈2 to 16 nm for Ag) of metals on solid supports such as cardboard, glass or silicon, islands of the evaporated metal tend to form. The clusters contribute to the high AEFs values (10^6 for cardboard) obtained. The high reproducibility could also be perceived. This is due to the several thousands of particles covered by the incident laser minimizing the possible existing heterogeneity.[29]

Freshly prepared PVD SERS substrates (6 nm layer of AgNPs deposited on a Si surface) were assayed for SERS efficiency by a single addition of the SERS label, R6G, at several concentrations (Figure 4. 30).

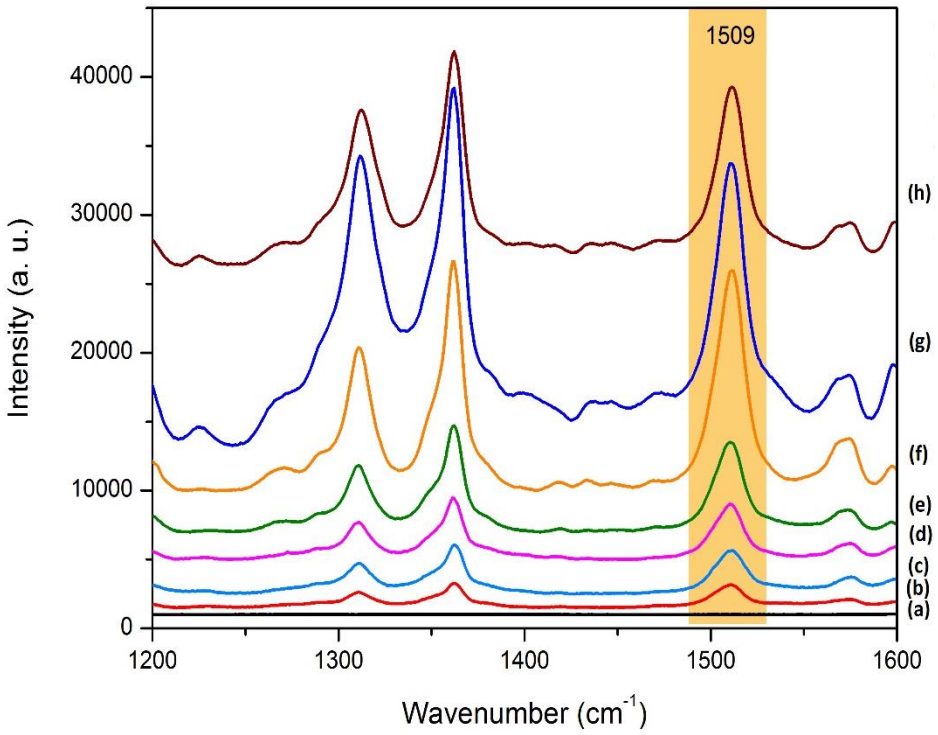

Figure 4. 30|R6G SERS spectra in PVD SERS substrate. (a) Substrate without R6G, *i.e.,* 6 nm of AgNPs (with 60 nm *per* particle) in crystalline silicon; same conditions and with several R6G concentrations added: (b) 10^{-9} M; (c) 10^{-8} M; (d) 10^{-7} M; (e) 10^{-6} M; (f) 10^{-5} M; (g) 10^{-4} M; and (h) 10^{-3} M;

To calculate the AEF values from SERS spectra of different concentrations of R6G, the bands areas of these spectra are obtained by using a peak fitting method.

Similarly, to the behaviour observed in the paper SERS substrates in section 4.6.3, the value AEF is smaller as the concentration of R6G increases.

As previously explained for the paper SERS substrates, the calculation of AEF assumes that all molecules contribute equally to the Raman signal. However, as the concentration of R6G increases, in terms of proportion, the percentage of molecules that experience a much larger enhancement in the *hot spots* is reduced. Consequently, the Raman signal of molecules away from *hot spots* may partly conceal the signal of molecules in these locations thereby decreasing the value of AEF (Figure 4. 31).[19]

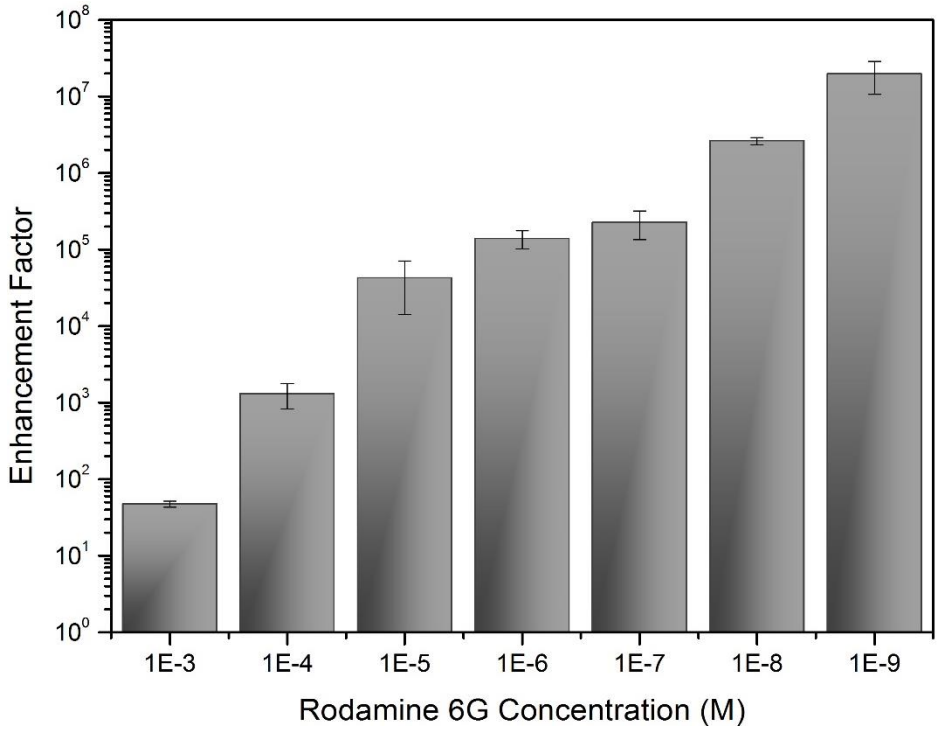

Figure 4. 31|Enhancement Factor values from the PVD SERS substrates. Each AEF value represented in the histogram is an average of three calculated areas values from three different locations of the SERS substrate with their respective SD.

The limit of detection was estimate by analysing the SERS signal from different concentrations of R6G from one stock solution. A correlation between SERS band areas and concentration was observed within the concentration range from 10^{-3} to 10^{-9} M. The plot in Figure 4. 32 represents the mean of three measurements of the SERS area at 1509 cm^{-1} and the error bar for each data point is the standard deviation of signal area.

The data points are fitted with a Langmuir isotherm with an r^2 of 0.947. Once again, it can be observed a maximum loading capacity of the substrate due to the limited number of adsorption sites to form an effective monolayer of analyte on that surface.[26,88]

A linear correlation in the range 10^{-6}-10^{-9} M allowed to determine LOD, sensitivity (slope of the working curve), and the linearity (r^2) from LOD to 10^{-6} M. The linear correlation resulted in a linear correlation coefficient of 0.993 with the following equation:

$$AA_{1509\ cm^{-1}} = (62 \pm 3) \times 10^4 C_{R6G} + (61 \pm 1) \times 10^{-2} \qquad \textit{(Equation 4.8)}$$

The LOD and LOQ obtained were (0.015 ± 0.02) ppm and (1.1 ± 0.2) ppm, respectively.

The standard deviations are due to the several factors in which the SERS signals depends, such as the surface diffusion of R6G molecules into and out of the *hot spots*, which is intrinsically related to their number. In fact, SERS intensity fluctuations in the measured timescale were observed.[9]

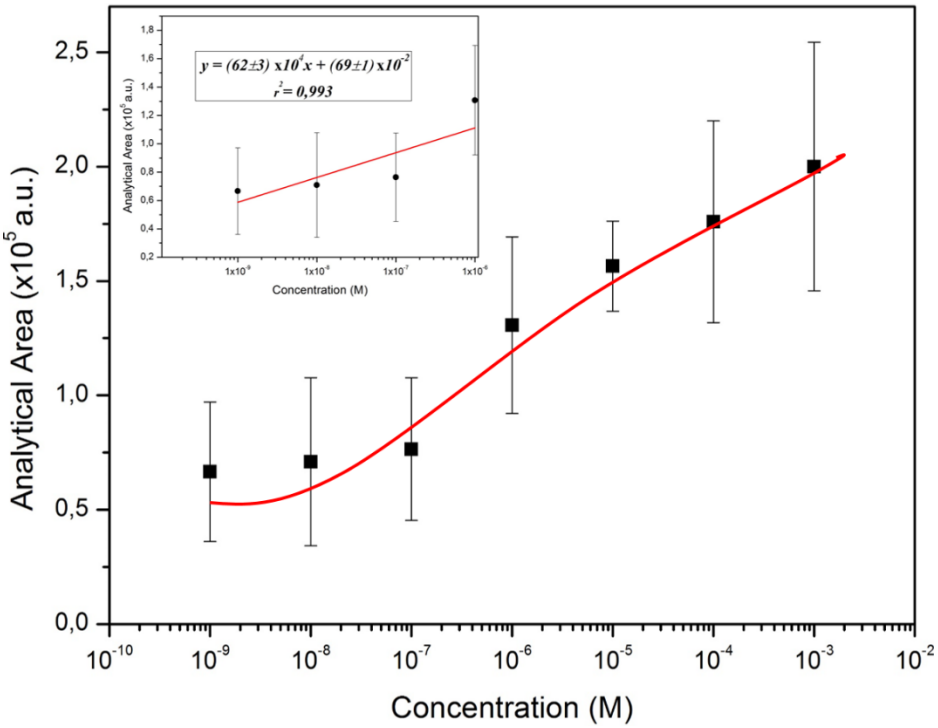

Figure 4. 32|Correlation between SERS band areas and R6G concentrations. Plots of analytical area *versus* R6G concentration for the band at 1509 cm^{-1}. Each data point represents the average value from three SERS spectra. Error bars show the standard deviations.

4.10.1.1.2 Malathion

In the same way that was performed in paper SERS substrate, the malathion detection performance was tested with several concentrations directly applied to the PVD SERS substrate. The detection performance for malathion is presented in Figure 4. 33 and can be identified by the band at 653 cm^{-1} (representative of the P=S bond).[96] Regarding the spectra from the PVD SERS substrate, a band at 521 cm^{-1} from silicon can be seen in all the SERS spectra with malathion, but there are other much feeble bands of unknown origin, emerging from the substrate.

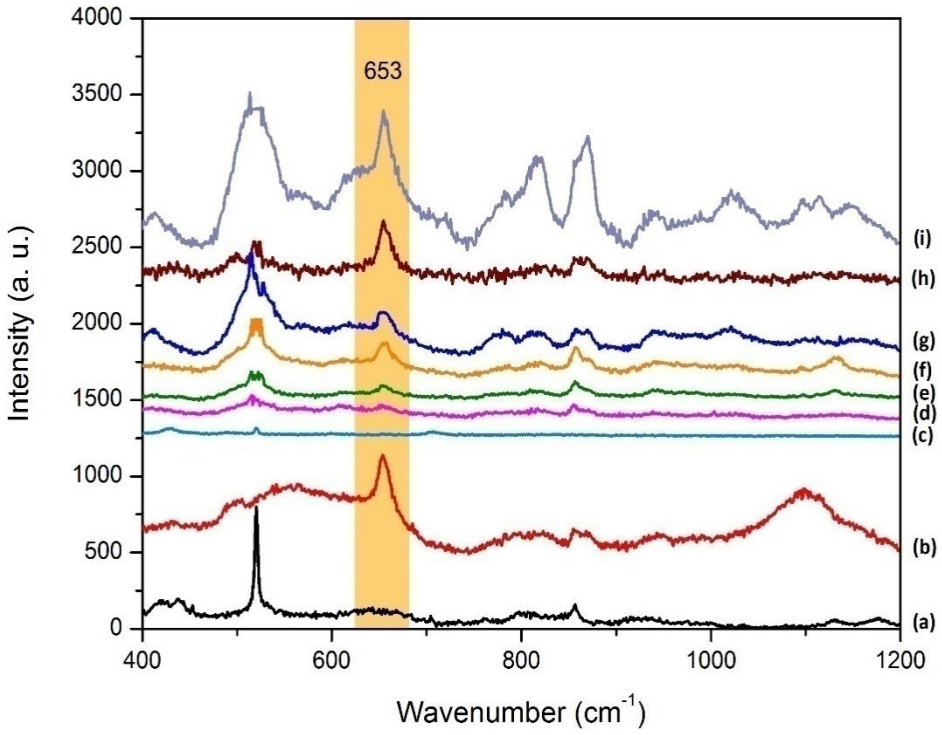

Figure 4. 33|Malathion SERS assay in PVD SERS substrate. (a) Substrate without malathion, *i.e.,* 6 nm of AgNPs (with 60 nm *per* particle) in crystalline silicon; (b) Raman spectrum of 3,72 M malathion with 660 µM of laser power. Same conditions and with several malathion concentrations added: (c) $1.5x10^{-2}$ M; (d) $2x10^{-2}$ M; (e) $2.5x10^{-2}$ M; (f) $3x10^{-2}$ M; (g) $3.5x10^{-2}$ M; and (h) $3x10^{-1}$ M; (i) 3.72 M. The characteristic band at 653 cm^{-1} was observed along with others distinctive bands. However, there are still slight interferences from the PVD SERS substrate.

The limit of detection for judging the PVD SERS substrate sensitivity for malathion detection method was evaluated with the same procedure used with paper SERS substrate (section 4.7.2). To evaluate the sensitivity of the SERS substrate, different concentrations of R6G from one stock solution were gauged.

The plot in Figure 4. 34 represents a correlation between 653 cm^{-1} band area and the concentration. Each point is the mean of three measurements and the error bar express the SD of signal area.

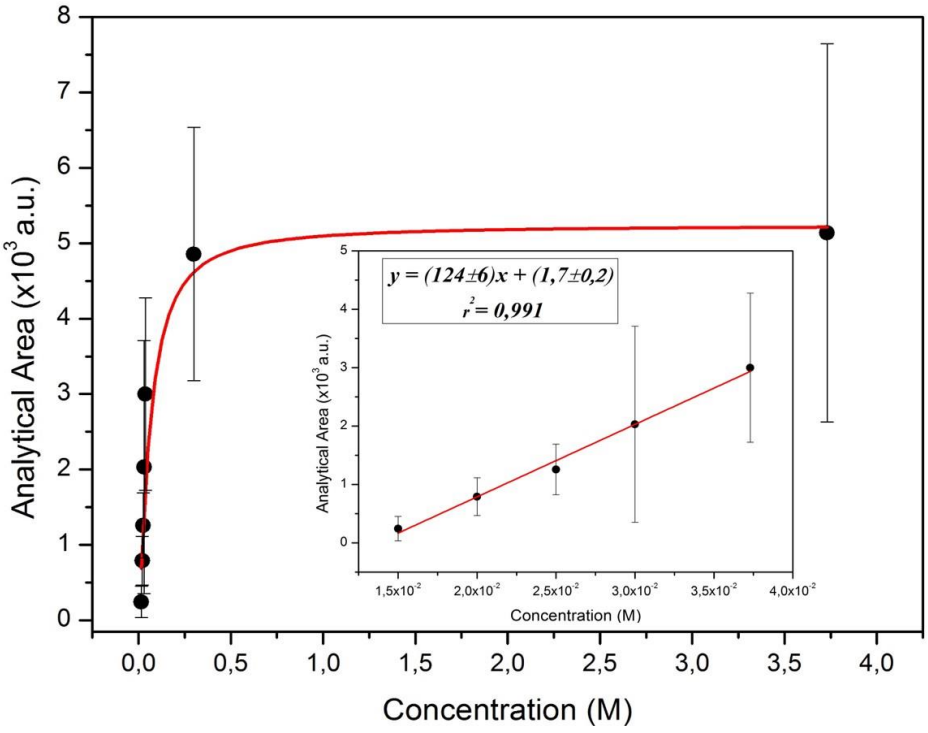

Figure 4. 34|Correlation between SERS band areas and malathion concentrations. Plots of analytical area *versus* malathion concentration for the band at 653 cm^{-1}. Each data point represents the average value from three SERS spectra. Error bars show the SD.

This data can be fit well by a Langmuir isotherm $r^2 = 0.948$, so quantitative detection of malathion can be performed using these PVD SERS substrates.

The Langmuir isotherm illustrate that with increasing concentration, as the surface coverage increases. The SERS intensity increases and attains maximum intensity at monolayer coverage.[26,70] As aforementioned, the band area increases linearly with concentration for low concentrations:

$$AA_{653\ cm^{-1}} = (124 \pm 6)C_{Malathion} + (1.7 \pm 0.2) \qquad \textit{(Equation 4.9)}$$

A linear correlation coefficient of $r^2 = 0.991$ was found. The linear correlation coefficient allows to determine the LOD and LOQ by equations 4.6 and 4.7. The LOD and LOQ, of $(9 \pm 7 \times 10^2)$ ppm and of $(5.6 \pm 0.1) \times 10^2$ ppm, were achieved by the PVD SERS substrate.

4.10.1.1.3 Domoic acid

Spectra from DA were also tried to concentrations of 10^{-2} and 10^{-3} M. By analysing the spectra, it is possible to identify bands corresponding only to DA (Figure 4. 35.*(b)*) such as 1653 and 1454 cm^{-1} and 1195 cm^{-1}, but also to the PVD SERS surface for instance 1141 cm^{-1} and 1605 cm^{-1} (Figure 4. 35.*(a)*). However, the bands relating to the PVD SERS surface are weak and thus do not interfere with DA spectra study.

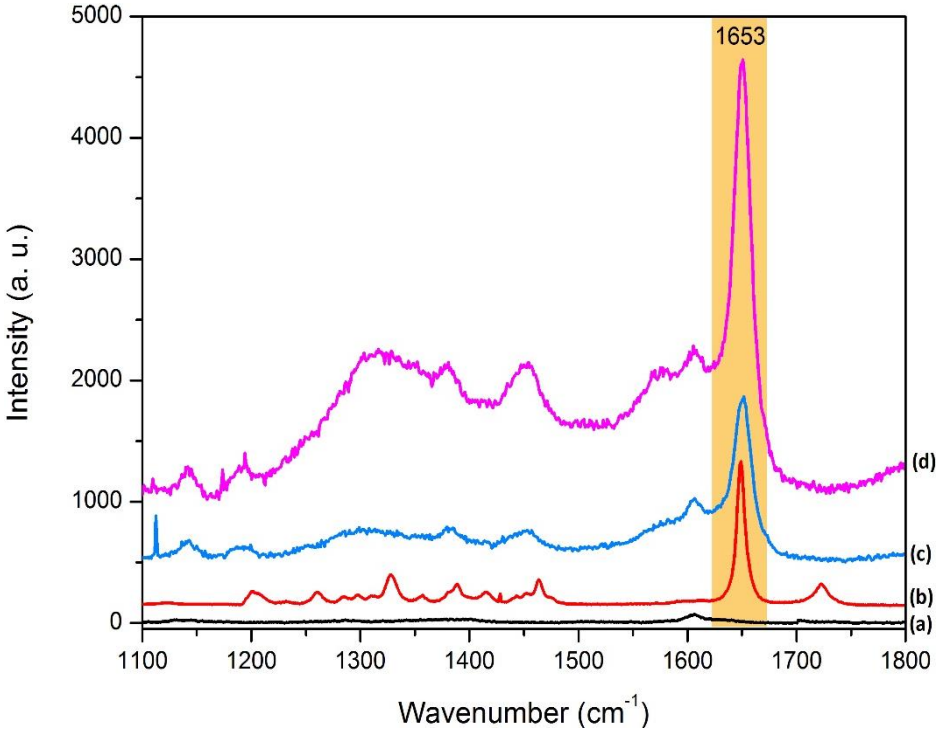

Figure 4. 35|SERS assay of DA on PVD SERS substrate. (a) Substrate without DA, *i.e.*, 6 nm of AgNPs (with 60 nm *per* particle) in crystalline silicon; (b) Raman spectrum of DA (one crystal). SERS spectra of (c) 10^{-3} M and (d) 10^{-2} M DA in the SERS substrate. The characteristic band at 1653 cm^{-1} was observed along with others distinctive bands. However, there are still slight interferences from the PVD SERS substrate.

4.10.2 SERS substrates with double layers of silver nanoparticles

In order to improve the original SERS PVD substrate, a second layer of NPs was deposited by the same method of PVD with or without a dielectric film (tantalum oxide – TaO_2) separating the two layers of 6 nm each. This approach had the intent of forming a three-dimensional surface with a higher density of *hot spots*. This oxide layer can also promote the stability against oxidation or contamination.[9] The thickness of the dielectric layer was varied and the SERS activity was measured in three types of support surfaces: cardboard, glass and silicon (Figure 4. 36).

Different laser power values were used to record the SERS signals across the different samples; the signals were normalized to the same laser power from the one used to obtained the R6G Raman signal spectra (660 µW).[33] Caution was attained by the fact that it is possible that surface modifications to the original materials may not be as laser tolerant, in other words, lower laser powers were applied first in detriment of the strongest.

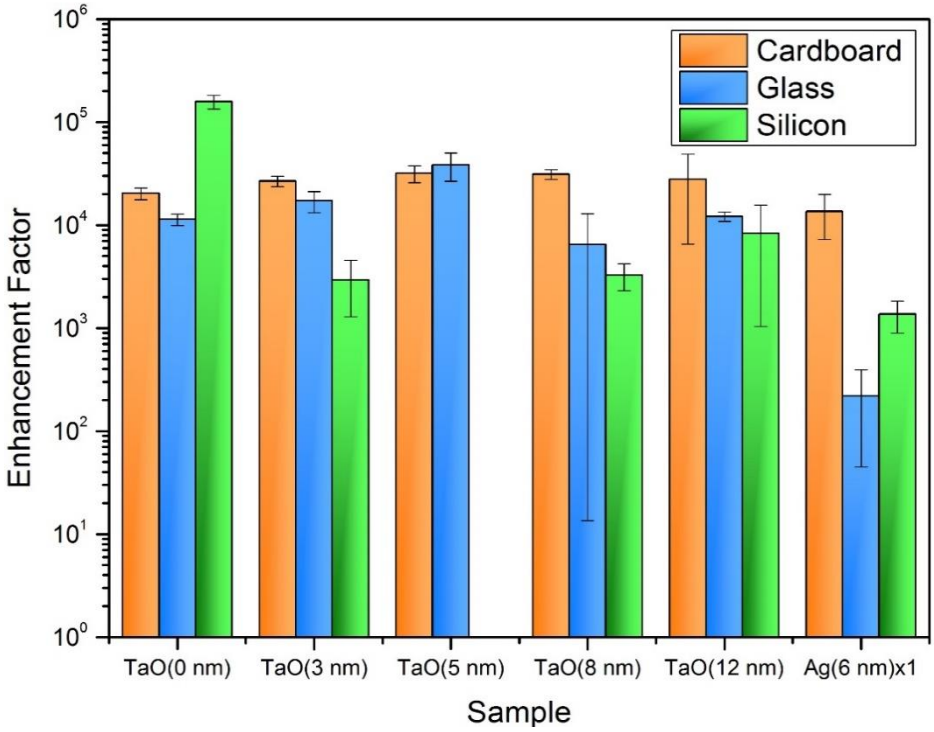

Figure 4. 36|AEF values from PVD SERS surfaces composited by a double layer of AgNPs with 6 nm of thick separated or not by a dielectric film of TaO_2. From the *right* to the *left*, the substrates are: Double layers of AgNPs without the TaO_2; Double layers of AgNPs with 3, 5, 8 and 12 nm of TaO_2 film separating the AgNPs and finally, the last samples investigated are the ones with just one layer of AgNPs with 6 nm to serve as control of those previously referred. In *yellow* are represented the data obtained in cardboard packaging substrate, in *blue* are the substrates produced in glass and in last the data acquired from the original PVD SERS surface in *green*.

The most striking observation is that the PVD SERS substrate with double layers produced on cardboard packaging substrate allowed more frequently higher AEFs values in detriment of the silicon and glass in same conditions which is in accordance with Araújo *et al.*. It was expected that the second layer would proportionate more *hot spots* contributing to an increase in the enhancement and since the Raman effect is distance dependence, an increase in TaO_2 thickness should diminish the AEF value. In fact, the resulted AEFs values were higher than the monolayer of AgNPs, however, several discrepancies are observed that compromises a reliable conclusion. Further studies are needed with a higher number of samples for statistical significance.

Another intriguing aspect is the variance between the different supports with the double layers. The SERS substrates supported in Si and glass present a more prominent variance between different samples. Conversely, the AEFs values for cardboard substrates are more stable. Thus the cardboard packaging substrate shows to be a very reproducible SERS substrate support.

4.10.3 SERS substrates with nanostars grown or deposited onto a monolayer of PVD silver nanoparticles

To improve the PVD SERS surface, chemically synthesized silver AgNSs were used and two different strategies were engaged: (1) growth of AgNSs onto NPs fabricated by PVD method; and (2) link of AgNSs to the original PVD SERS surface.

In the first strategy the aim was to stimulate *in-situ* the conversion of AgNPs to AgNSs by dipping the original PVD SERS surface into the synthesis media. The concentration of HA and immersion time used, were parameters evaluated, and the AEF values are represented in the following Figure 4. 37.I and II respectively. The Table 4. 9 shows the conditions in which the samples

were produced. The results were inconclusive since for independent series of SERS substrates the behaviour displayed was not consistent. More immersion time did not consistently show higher AEF values nor the increase of 10 and 20 times in HA concentration exhibited an invariably increase.

The AEF values here are relative to 10^{-3} M R6G in glass surface (as control) and the SERS substrate sample with 10^{-6} M. Thus relative to the original PVD SERS surface, the substrates obtained by this technique did not achieved reasonable improvement. A possible reason may be related to a lower concentration of AgNSs chemically grown on the surface. It was though that the conversion of the nuclei to AgNSs would be an energetically favoured process over the nucleation and growth of new AgNSs in solution. In fact, the synthesis of AgNSs in the solution was apparent.

Table 4. 9|Samples analysed produced by growing AgNSs onto a monolayer of AgNPs - PVD SERS substrate.

Nomenclature Series	HA		Surface	Thick layer of AgNPs
	Concentration (mM)	Immersion Time (min)		
A1	3	120	Si	4
A2	60	120	Si	4
B1	3	10	Si	4
B2	30	10	Si	4
B3	60	10	Si	4

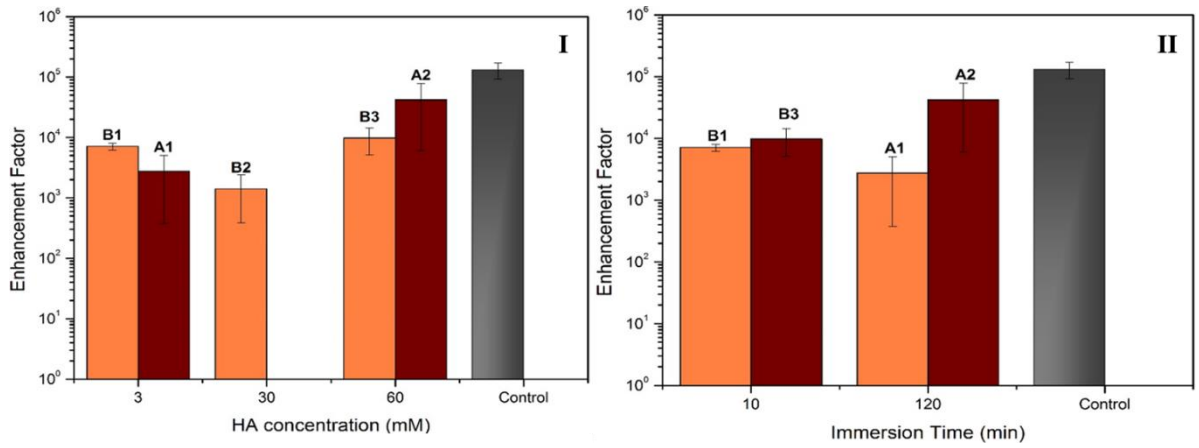

Figure 4. 37|AEF values from surfaces where growth of NPs fabricated by PVD method into AgNSs was performed. In (I) the concentration of HA was tested and in (II) was the immersion time of the original PVD SERS surface in the solution of HA. Control: monolayer of AgNPs.

The second strategy was performed by linking the previously synthesized AgNSs in solution to a linker to attain a homogenous deposition of AgNSs on the PVD SERS surface. Several conditions were tested relating to the linker concentration and the concentration of AgNSs used (Table 4. 10).

Higher concentration of linker (100 µM) resulted in very low AEF values and one possible explanation could be a steric hindrance for *hot spot*s by the ligand in relation to R6G molecules. At lower concentrations the AEF values increased and 1 µM ensued similar values comparing to surfaces were 10 µM of linker was applied (Figure 4. 38.I). An increase in the AgNSs concentration of 4 times demonstrated a factor of 10 intensification in AEF value which was according to the expected (Figure 4. 38.II).

However, this surfaces still did not present a progress regarding the original surface and exhibit lower AEF values. It is possible that the linker at the surfaces of the AgNSs did not allowed an approximation of R6G, and consequently, the number of R6G molecules that are enhanced is lower. Moreover, the substrates obtained by these methods although analysed promptly as possible, may not represent the best conditions since the original surface was aged at the time of the AgNSs deposition.

Table 4. 10|Samples analysed produced by depositing AgNSs onto a monolayer of AgNPs. The concentration of linker and the AgNSs used, were parameters evaluated and each sample corresponds to a letter and a number.

Nomenclature Series	Linker		AgNSs		Surface	Thick layer of AgNPs
	Concentration (μM)	Immersion Time (min)	Concentration (nM)	Immersion Time (min)		
A1	1	30	0.1	30	Si	6
A2	10	30	0.1	30	Si	6
B1	1	30	0.4	30	Si	6
B2	10	30	0.4	30	Si	6
C1	1	30	0.4	30	Cardboard	6
C2	10	30	0.4	30	Cardboard	6

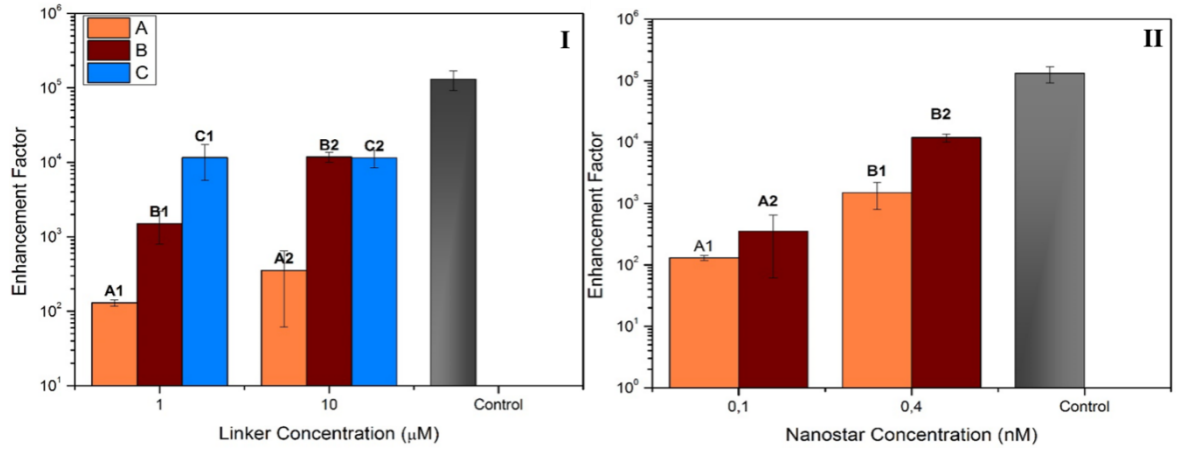

Figure 4. 38|Enhancement Factor values from surfaces where linkage of AgNSs to the original PVD SERS surface was performed. In (I) the linker concentration was tested and in (II) was the AgNSs concentration deposited in the original PVD SERS surface. Control: monolayer of AgNPs.

Chapter 5. Conclusion and Future Perspectives

This project had the main objective of developing new efficient substrates for SERS application. Two types of substrates SERS, paper and PVD substrates were investigated.

The paper-based SERS substrate is a disposable approach and two types of paper were investigated: Whatman no.1 paper and office paper. Both papers were *drop-casted* with several types of silver NPs with the aim to explore the most suitable alternative for sensitive SERS measurements. Characterization of the chemically synthesised NPs was performed by UV-Vis spectroscopy studies and followed by SEM. The paper SERS substrates were analysed through SEM-EDS and Raman techniques.

The performance of SERS substrates fabricated by PVD were also investigated. Several modifications were fulfilled with the aim of improve SERS efficiency and accomplishing detection limits in the sub ppb range.

SERS assays were performed in order to evaluate the efficiency of SERS substrates. The SERS label used in this project, was the R6G due its large effective cross-section that results in a strong SERS signal.

PVD SERS surfaces prepared and variations of this type of surfaces were evaluated in terms of SERS efficiency, and field-detection applications.

PVD SERS substrates (6 nm layer of AgNPs deposited on a Si surface) were assayed for SERS efficiency. The LOD and LOQ for R6G were of (0.015 ± 0.02) ppm and (1.1 ± 0.2) ppm, respectively. For malathion, the LOD and LOQ achieved by the PVD SERS substrate were of (9 ± 7) ppm and of $(5.6 \pm 0.1) \times 10^2$ ppm, respectively. SERS assay from DA were also tried, however only the DA concentrations of 10^{-2} and 10^{-3} M were detected.

PVD SERS substrate with double layers of AgNPs separated by a TaO_2 layer produced, had the intention of proportionate more *hot spots*, resulting in an average increased enhancement for any of the conditions tested. However, several discrepancies were observed compromising a reliable conclusion. Further studies are needed with a higher number of samples for statistical significance. Cardboard packaging substrate allowed more frequently higher AEFs values in detriment of the silicon and glass in same conditions with more reproducible signals, in accordance with what was reported by Araújo *et al.*.[29]

Chemically synthesized AgNSs were used with the aim to improve the PVD SERS surface, and two different strategies were used: (1) growth of AgNSs onto NPs fabricated by PVD method; and (2) link of AgNSs to the original PVD SERS surface. However, the AEF values demonstrated by this modification did not corresponded to the aimed. It is possible that the AgNSs originated from the NPs in (1), were not in sufficient concentration to enable higher AEF values. Regarding the AgNSs in (2), the linker chosen at the surfaces of the AgNSs did not allowed an approximation of R6G molecules, and consequently, the number of R6G molecules that are enhanced were lower.

Regarding the paper SERS substrates, three different morphologies of NPs were tested. The methods adapted to the synthesis of AgNPs, and AgNSs developed by Bastús *et al.* and Garcia-Leis *et al.* respectively, validated their high reproducibility since all the batches provided particles of identical size and concentrations.[83,84] The critical coagulation concentration was investigated in order to promote the aggregation of the AgNPs in identical conditions (50 mM NaCl). The use of aggregated AgNPs had the intention of generate several *hot spots,* which led, to higher enhancements. The degree of anisotropy was greater for AgNSs than for the other two types of NPs.

The suitable laser power for the SERS assays was 660 μW optimized through laser power influence study. It showed to be effective in the collection of SERS spectra because it resembles the

signals observed by conventional Raman spectrometry at high analyte concentrations minimizing the detrimental laser radiations effects on the sample.

The use of paper as support for SERS substrates is an abundant, usable, cost-efficient and biodegradable alternative. In the present work, two types of papers were characterized by SEM, EDS and Raman spectroscopy. Subsequently, their SERS performance as substrate supports was tested. The office paper revealed to have a more compact surface than the Whatman no.1 paper due to its intrinsic lower porosity. This feature proportionated a higher concentration of the NPs at the surface, since they have less space to penetrate into the paper.

The porosity of the papers proved to be a key factor in the development of an optimized SERS signal. Because the pronounced different cellulose fibril orientation in Whatman no.1 paper, irreproducible signs were more often observed as opposed to office paper. Increasing the volume of NPs to 500 μL allowed to accomplish higher AEF values and lower R6G concentrations of detection with reproducible results. These values are in agreement with the literature.[26]

The aggregated AgNPs and AgNSs (at low R6G concentrations) demonstrate the existence of anomalous Raman bands assigned to the capping agent citrate. Unfortunately, treatments with HCl performed onto the paper SERS substrates in order to oxidize superficial citrate molecules, were not completely successful, and further work is still required to completely remove its presence. This event illustrate that interferences should be well studied towards getting a well-reasoned analysis due to possible analyte-like appearing features.[97]

Aggregation triggered by salt was established as inadequate for paper SERS substrates. When AgNPs were added to the paper, an aggregation phenomenon occurred as the silver colloid solution dried. This aggregation of AgNPs allowed an AEF value of $1.1 \pm 0.4 \times 10^6$ to 10^{-8} M of R6G due to huge electric fields, originating from a higher degree in anisotropy of NPs formed by particle intergrowth. Although the aggregations may sometimes provide excellent SERS substrate, its low reproducibility level of uncontrolled aggregation, varying the SERS efficiency, limits their use.

The AgNSs provide larger AEF values and smaller detectable concentrations ($(1.1 \pm 0.8 \times 10^6)$ to 10^{-9} M of R6G) in accordance with expected. The sharp protrusions in the stars leads to a large and spatially confined electromagnetic enhancement effect, but also in spaces between arms.

The sensitivity of the paper SERS substrate was estimated by stablishing a correlation between SERS band areas and the analyte concentration. For the R6G, the detection and quantification limits were 0.17 ± 0.04 ppb and 2.5 ± 0.5 ppb. The malathion achieved a LOD of $(2 \pm 1) \times 10^3$ ppm and a LOQ of 3944 ± 7 ppm. The DA spectra only exhibited a band at 1650 cm^{-1}, therefore this toxin could not be reliable detected.

SERS measurements include an average of several AgNSs, which reduces the variation in plasmonic enhancement, leading to low standard-deviations and consequently, this type of paper SERS substrates reveal intra-well reproducibility. Additionally, reproducibility inter-wells (independent batches) was evaluated revealing 1.9% of RSD, and the time stability study conceded and RSD of 7.3% suggesting a stable SERS substrate.

In this study efficient SERS substrates were produced and investigated. The results suggest that the shift in the vibrational level, due to surface interaction between adsorbed molecules and AgNPs of the PVD and paper SERS substrates, was not significantly different from other types of SERS substrate reported in literature.[29,30,33] The distinct values of LOD and LOQ obtained for all the analytes herein referred, highlight that the sensitivity proprieties are not the same for all molecules or species adsorbed on metallic substrates. The overall enhancement of the Raman signal is dependent of the interfacial affinity and also of the resonance mechanisms.

The modifications in the PVD SERS substrate for higher AEF values achievement were unsuccessful. Nevertheless, the original PVD SERS substrate developed is simple, highly sensitive and economical since it is fabricated by a low-temperature methodology. Also, SERS assays in both substrates are rapid and takes less than 10 min since the sample is added to its detection and analysis.

The paper SERS substrate reported in this project used AgNSs with good plasmonic properties to present a large SERS intensification without requiring to aggregation methods. However, further investigations are necessary to eliminate the possible interferences from the capping agent used in the AgNS synthesis. To overcome this problem, amino-functionalized AgNSs could be attained.[50]

After the interference problems are eliminated, the analytes could be investigated in different matrices such as DA, which can be detected in clam tissue and malathion in fruit crops to evidence practical-field applications**.**

Ultimately, the paper and PVD SERS substrates are rapid, inexpensive and sensitive. Both establish an extremely simple promising analyte detection platform by Raman spectroscopy that may have immediate applications for food safety, providing *on-site* trace chemical analysis and even in remote locations.

Chapter 6. References

1. Zheng, J. & He, L. Surface-Enhanced Raman Spectroscopy for the Chemical Analysis of Food. *Compr. Rev. Food Sci. Food Saf.* **13,** 317–328 (2014).
2. Wu, Q. *et al.* UV resonance Raman detection and quantitation of domoic acid in phytoplankton. *Anal. Chem.* **72,** 1666–71 (2000).
3. Campàs, M., Prieto-Simón, B. & Marty, J.-L. Biosensors to detect marine toxins: Assessing seafood safety. *Talanta* **72,** 884–95 (2007).
4. Olson, T. Y., Schwartzberg, A. M., Liu, J. L. & Zhang, J. Z. Raman and Surface-Enhanced Raman Detection of Domoic Acid and Saxitoxin. *Appl. Spectrosc.* **65,** 159–164 (2011).
5. Dubois, M. *et al.* Development of ELISAs for detecting domoic acid, okadaic acid, and saxitoxin and their applicability for the detection of marine toxins in samples collected in Belgium. *Food Addit. Contam. Part A. Chem. Anal. Control. Expo. Risk Assess.* **27,** 859–68 (2010).
6. Haughey, S. a *et al.* Comparison of biosensor platforms for surface plasmon resonance based detection of paralytic shellfish toxins. *Talanta* **85,** 519–26 (2011).
7. Nelson, W. H., Hanlon, E. G., Dasari, R. R. & Feld, M. Uv Raman detection of micro-organisms and their toxins in fish tissue. *Proc. SPIE* **4577,** 193–204 (2002).
8. Siebert, F. & Hildebrandt, P. *Theory of Infrared Absorption and Raman Spectroscopy*. *Vibrational Spectroscopy in Life Science* (2008).
9. Schlücker, S. Surface-enhanced Raman spectroscopy: concepts and chemical applications. *Angew. Chem. Int. Ed. Engl.* **53,** 4756–95 (2014).
10. Fleischmann, M., Hendra, P. J. & McQuillan, A. J. Raman Spectra of pyridine adsorbed at a silver electrode. *Chem. Phys. Lett.* **26,** 2–5 (1974).
11. D Howes, P., Rana, S. & M Stevens, M. Plasmonic nanomaterials for biodiagnostics. *Chem. Soc. Rev.* **43,** 3835–53 (2014).
12. Pearman, W. F. & Hall, S. Surface-Enhanced Raman Spectroscopy of Saxitoxins: Exploratory Studies. *Photonics Res. Cent. United States Mil. Acad. West Point, NY 10996 (2009 Progr. Rev.* 2–9 (2009).
13. Jeanmaire, D. L. & Van Duyne, R. P. Surface Raman Spectroelectrochemistry. *J. Electroanal. Chem.* **84,** 1–20 (1977).
14. Albrecht, M. G. & Creighton, J. A. Anomalously Intense Raman Spectra of Pyridine at a Silver Electrode. *J. Am. Chem. Soc.* 5215–5217 (1977).
15. Nie, S. & Emory, S. R. Probing Single Molecules and Single Nanoparticles by Surface-Enhanced Raman Scattering. *Science (80-.).* **275,** 1102–1106 (1997).
16. Kneipp, K. *et al.* Single Molecule Detection Using Surface-Enhanced Raman Scattering (SERS). *Phys. Rev. Lett.* **78,** 1667–1670 (1997).
17. Stiles, P. L., Dieringer, J. a, Shah, N. C. & Van Duyne, R. P. Surface-enhanced Raman spectroscopy. *Annu. Rev. Anal. Chem. (Palo Alto. Calif).* **1,** 601–26 (2008).
18. Valley, N., Greeneltch, N., Van Duyne, R. P. & Schatz, G. C. A look at the origin and

magnitude of the chemical contribution to the enhancement mechanism of surface-enhanced Raman spectroscopy (SERS): Theory and experiment. *J. Phys. Chem. Lett.* **4,** 2599–2604 (2013).

19. LeRu, E. C., Meyer, M. & Etchegoin, P. G. Surface Enhanced Raman Scattering Enhancement Factors: A Comprehensive Study. *J. Phys. Chem. B* **111,** 13794–13803 (2007).

20. Xu, H., Aizpurua, J., Kall, M. & Apell, P. Electromagnetic contributions to single-molecule sensitivity in surface-enhanced raman scattering. *Phys. Rev. E. Stat. Phys. Plasmas. Fluids. Relat. Interdiscip. Topics* **62,** 4318–24 (2000).

21. Ma, W. Y. *et al.* A numerical investigation of the effect of vertex geometry on localized surface plasmon resonance of nanostructures. *Opt. Express* **18,** 843–853 (2010).

22. Betz, J. F., Yu, W. W., Cheng, Y., White, I. M. & Rubloff, G. W. Simple SERS substrates: powerful, portable, and full of potential. *Phys. Chem. Chem. Phys.* **16,** 2224–39 (2014).

23. Yang, K.-H., Liu, Y.-C. & Yu, C.-C. Enhancements in intensity and stability of surface-enhanced Raman scattering on optimally electrochemically roughened silver substrates. *J. Mater. Chem.* **18,** 4849 (2008).

24. Fan, M., Andrade, G. F. S. & Brolo, A. G. A review on the fabrication of substrates for surface enhanced Raman spectroscopy and their applications in analytical chemistry. *Anal. Chim. Acta* **693,** 7–25 (2011).

25. Cao, Y., Li, D., Jiang, F., Yang, Y. & Huang, Z. Engineering metal nanostructure for SERS application. *J. Nanomater.* **2013,** 12 (2013).

26. Hoppmann, E. P., Yu, W. W. & White, I. M. Highly sensitive and flexible inkjet printed SERS sensors on paper. *Methods* **63,** 219–24 (2013).

27. Hulteen, J. C. & Duyne, R. P. Van. Nanosphere lithography : A materials general fabrication process for periodic particle array surfaces. *J. Vac. Sci. Technol.* **13,** 1553–1558 (1995).

28. Tao, A. R., Habas, S. & Yang, P. Shape control of colloidal metal nanocrystals. *Small* **4,** 310–325 (2008).

29. Araújo, A. *et al.* Highly efficient nanoplasmonic SERS on cardboard packaging substrates. *Nanotechnology* **25,** 415202 (2014).

30. Yu, W. W. & White, I. M. Inkjet-printed paper-based SERS dipsticks and swabs for trace chemical detection. *Analyst* **138,** 1020–5 (2013).

31. Cheng, M. L., Tsai, B. C. & Yang, J. Silver nanoparticle-treated filter paper as a highly sensitive surface-enhanced Raman scattering (SERS) substrate for detection of tyrosine in aqueous solution. *Anal. Chim. Acta* **708,** 89–96 (2011).

32. Lee, C. H., Tian, L. & Singamaneni, S. Paper-based SERS swab for rapid trace detection on real-world surfaces. *ACS Appl. Mater. Interfaces* **2,** 3429–35 (2010).

33. Yu, W. W. & White, I. M. Inkjet printed surface enhanced raman spectroscopy array on cellulose paper. *Anal. Chem.* **82,** 9626–9630 (2010).

34. Wu, D. & Fang, Y. The adsorption behavior of p-hydroxybenzoic acid on a silver-

coated filter paper by surface enhanced Raman scattering. *J. Colloid Interface Sci.* **265,** 234–238 (2003).

35. Yu, W. W. & White, I. M. A simple filter-based approach to surface enhanced Raman spectroscopy for trace chemical detection. *Manuscript, Author* **137,** 1168–1173 (2012).

36. Qu, L.-L. *et al.* Fabrication of bimetallic microfluidic surface-enhanced Raman scattering sensors on paper by screen printing. *Anal. Chim. Acta* **792,** 86–92 (2013).

37. Yetisen, A. K., Akram, M. S. & Lowe, C. R. Paper-based microfluidic point-of-care diagnostic devices. *Lab Chip* **13,** 2210–51 (2013).

38. Zhao, W. & van der Berg, A. Lab on paper. *Lab Chip* **8,** 1988–1991 (2008).

39. Costa, M. N. *et al.* A low cost, safe, disposable, rapid and self-sustainable paper-based platform for diagnostic testing: lab-on-paper. *Nanotechnology* **25,** 094006 (2014).

40. Laufmann, M. in *Handbook of Paper and Board* (ed. Holik, H.) 109–143 (Wiley-VCH Verlag GmbH & Co. KGaA, 2013).

41. Shim, S., Stuart, C. M. & Mathies, R. a. Resonance Raman cross-sections and vibronic analysis of rhodamine 6G from broadband stimulated raman spectroscopy. *ChemPhysChem* **9,** 697–699 (2008).

42. Jensen, L. & Schatz, G. C. Resonance Raman scattering of rhodamine 6G as calculated using time-dependent density functional theory. *J. Phys. Chem. A* **110,** 5973–5977 (2006).

43. Smith, W. E. Practical understanding and use of surface enhanced Raman scattering/surface enhanced resonance Raman scattering in chemical and biological analysis. *Chem. Soc. Rev.* **37,** 955–64 (2008).

44. Dieringer, J. a *et al.* Surface-Enhanced Raman Excitation Spectroscopy of a Single Rhodamine 6G Molecule. *J. Am. Chem. Soc.* **131,** 849–854 (2009).

45. PubChem Compound Database. Chemical Structure of Rhodamine 6 G (CID=13806). *National Center for Biotechnology Information* at <http://pubchem.ncbi.nlm.nih.gov/compound/13806#section=Top>

46. Burri, S. & Vale, P. Contaminação de bivalves por DSP : risco de episódios de gastrenterites numa região de toxicidade endémica. **24,** 115–124 (2006).

47. Garrison, D. L., Conrad, S. M., Eilers, P. P. & Waldron, E. M. Confirmation of domoic acid Production by Pseudonitzschia Australis (Bacillariophyceae) Cultures. *J. Phycol.* **28,** 604–607 (1992).

48. Douglas, D. J. *et al.* Accumulation of domoic acid by the sea scallop (Placopecten magellanicus) fed cultured cells of toxic Pseudo-nitzschia multiseries. *Can. J. Fish. Aquat. Sci.* **54,** 907–913 (1997).

49. Paytan, A. *et al.* Toxicity of atmospheric aerosols on marine phytoplankton. *Proc. Natl. Acad. Sci. U. S. A.* **106,** 4601–5 (2009).

50. Müller, C. *et al.* Amnesic shellfish poisoning biotoxin detection in seawater using pure or amino-functionalized Ag nanoparticles and SERS. *Talanta* (2014).

51. Gerssen, A. *et al.* Marine toxins: chemistry, toxicity, occurrence and detection, with

special reference to the Dutch situation. *Toxins (Basel).* **2,** 878–904 (2010).

52. Lefebvre, K. a & Robertson, A. Domoic acid and human exposure risks: a review. *Toxicon* **56,** 218–30 (2010).

53. Commission, T. H. E., The, O. F. & Communities, E. Commission Decision of 15 March 2002 laying down detailed rules for the implementation of Council Directive 91/492/EEC as regards the maximum levels and the methods of analysis of certain marine biotoxins in bivalve molluscs, echinoderms, tunicates and ma. *Off. J. Eur. Communities* 62–64 (2002).

54. Vilariño, N., Louzao, M. C., Vieytes, M. R. & Botana, L. M. Biological methods for marine toxin detection. *Anal. Bioanal. Chem.* **397,** 1673–81 (2010).

55. 293/98, D.-L. n. . Ministério da agricultura, do desenvolvimento rural e das pescas - Capítulo V (Prescrições relativas aos moluscos bivalves vivos). *Diário da República* 4828–4838 (1998).

56. Bates, S. S. *et al.* Pennate Diatom Nitzxchia pungens as the Primary Source of Domoic Acid, a Toxin in Shellfish from Eastern Prince Edward Island, Canada. *Can. J. Fish. Aquat. Sci.* **46,** 1203–1215 (1989).

57. Teitelbaum, J. S. *et al.* Neurologic Sequelae of Domoic Acid Intoxication due to the Ingestion of Contaminated Mussels. *N. Engl. J. Med.* **322,** 1781–1787 (1990).

58. Djaoued, Y., Balaji, S. & Priya, S. Non-resonance micro-Raman spectroscopic studies on crystalline domoic acid and its aqueous solutions. *Spectrochim. Acta. A. Mol. Biomol. Spectrosc.* **67,** 1362–9 (2007).

59. Diouf, J. Hundred and Twenty-third Session of the Food and Agriculture Organization of the United Nations Council. in *International Code of Conduct on the Distribution and Use of Pesticides - Revised version* (ed. Diouf, J.) (Management Service Information Division, 2005).

60. Nili-Ahmadabadi, A. *et al.* On the biochemical and molecular mechanisms by which malathion induces dysfunction in pancreatic islets in vivo and in vitro. *Pestic. Biochem. Physiol.* **106,** 51–60 (2013).

61. Quintás, G., Garrigues, S. & De La Guardia, M. FT-Raman spectrometry determination of Malathion in pesticide formulations. *Talanta* **63,** 345–350 (2004).

62. Singhal, R. K. Remediation of Malathion Contaminated Soil Using Zero Valent Iron Nano-Particles. *Am. J. Anal. Chem.* **03,** 76–82 (2012).

63. Molecular Structure of Malathion. *PubChem Open Chemistry Databased - National Center for Biotechnology Information* (2005). at <http://pubchem.ncbi.nlm.nih.gov/compound/4004#section=Top>

64. Shende, C., Gift, A., Inscore, F., Maksymiuk, P. & Farquharson, S. Inspection of pesticide residues on food by surface enhanced Raman spectroscopy. *Proc. SPIE* **5271,** 28–34 (2004).

65. Pope, C., Karanth, S. & Liu, J. Pharmacology and toxicology of cholinesterase inhibitors: Uses and misuses of a common mechanism of action. *Environ. Toxicol. Pharmacol.* **19,** 433–446 (2005).

66. Cholinesterase Inhibitors-Organophosphates. *Equine Vet Adventures* (2014). at

<http://equinevetadventures.tumblr.com/post/103395273330/cholinesterase-inhibitors-organophosphates-and>

67. Lai, S. C. S. & Koper, M. T. M. Ethanol electro-oxidation on platinum in alkaline media. *Phys. Chem. Chem. Phys.* **11,** 10446–56 (2009).

68. Zhang, X., Shah, N. C. & Van Duyne, R. P. Sensitive and selective chem/bio sensing based on surface-enhanced Raman spectroscopy (SERS). *Vib. Spectrosc.* **42,** 2–8 (2006).

69. Piorek, B. D., Lee, S. J., Moskovits, M. & Meinhart, C. D. Free-Surface Microfluidics/Surface-Enhanced Raman Spectroscopy for Real-Time Trace Vapor Detection of Explosives. *Anal. Chem.* **84,** 9700–9705 (2012).

70. Dasary, S. S. R., Singh, A. K., Senapati, D., Yu, H. & Ray, P. C. Gold nanoparticle based label-free SERS probe for ultrasensitive and selective detection of trinitrotoluene. *J. Am. Chem. Soc.* **131,** 13806–12 (2009).

71. Wustholz, K. L., Brosseau, C. L., Casadio, F. & Duyne, R. P. Van. Surface-enhanced Raman spectroscopy of dyes: from single molecules to the artists' canvas. *Phys. Chem. Chem. Phys.* **11,** 7348–9 (2009).

72. Wijaya, W., Pang, S., Labuza, T. P. & He, L. Rapid detection of acetamiprid in foods using surface-enhanced Raman spectroscopy (SERS). *J. Food Sci.* **79,** T743–7 (2014).

73. Zhang, X. F. *et al.* Detection of melamine in liquid milk using surface-enhanced Raman scattering spectroscopy. *J. Raman Spectrosc.* **41,** 1655–1660 (2010).

74. Liu, Y. & Liu, T. Determination of pesticide residues on the surface of fruits using micro-Raman spectroscopy. *IFIP Adv. Inf. Commun. Technol.* **347 AICT,** 427–434 (2011).

75. Huai, Q., Gao, C., Miao, J., Yao, H. & Wang, Z. Fast detection of saxitoxin using laser tweezers surface enhanced Raman spectroscopy. *Anal. Methods* **5,** 6870 (2013).

76. Lin, W.-C. *et al.* SERS Study of Tetrodotoxin (TTX) by Using Silver Nanoparticle Arrays. *Plasmonics* **4,** 187–192 (2009).

77. Pearman, W. F., Angel, S. M., Ferry, J. L. & Hall, S. Characterization of the Ag mediated surface-enhanced Raman spectroscopy of saxitoxin. *Appl. Spectrosc.* **62,** 727–32 (2008).

78. Pearman, W. F., Jones, C., Johnson, K. & Hall, S. Verification of Silver Colloidal Properties for Surface Enhanced Raman Spectroscopic Analysis of Saxitoxins. *Photonics Res. Cent. United States Mil. Acad. West Point, NY 10996 (2012 Progr. Rev.* 6–15 (2012).

79. Li, Y. T. *et al.* Rapid and sensitive in-situ detection of polar antibiotics in water using a disposable Ag-graphene sensor based on electrophoretic preconcentration and surface-enhanced Raman spectroscopy (Supplementary Material). *Biosens. Bioelectron.* **43,** 94–100 (2013).

80. Barahona, F., Bardliving, C. L., Phifer, A., Bruno, J. G. & Batt, C. a. An Aptasensor Based on Polymer-Gold Nanoparticle Composite Microspheres for the Detection of Malathion Using Surface-Enhanced Raman Spectroscopy. *Ind. Biotechnol.* **9,** 42–50 (2013).

81. Albuquerque, C. D. L. & Poppi, R. J. Detection of malathion in food peels by surface-enhanced Raman imaging spectroscopy and multivariate curve resolution. *Anal. Chim. Acta* **879,** 24–33 (2015).

82. Lee, P. C. & Meisel, D. Adsorption and surface-enhanced Raman of dyes on silver and gold sols. *J.Phys.Chem.* **86,** 3391–3395 (1982).

83. Bastús, N. G., Merkoçi, F., Piella, J. & Puntes, V. Synthesis of Highly Monodisperse Citrate-Stabilized Silver Nanoparticles of up to 200 nm: Kinetic Control and Catalytic Properties. *Chem. Mater.* **26,** 2836–2846 (2014).

84. Garcia-Leis, A., Garcia-Ramos, J. V. & Sanchez-Cortes, S. Silver nanostars with high SERS performance. *J. Phys. Chem. C* **117,** 7791–7795 (2013).

85. Martinez, A. W., Phillips, S. T., Butte, M. J. & Whitesides, G. M. Patterned paper as a platform for inexpensive, low-volume, portable bioassays. *Angew. Chem. Int. Ed. Engl.* **46,** 1318–20 (2007).

86. Bhandari, D., Walworth, M. J. & Sepaniak, M. J. Dual function surface-enhanced Raman active extractor for the detection of environmental contaminants. *Appl. Spectrosc.* **63,** 571–8 (2009).

87. Wang, G. *et al.* Surface-enhanced Raman scattering in nanoliter droplets: towards high-sensitivity detection of mercury (II) ions. *Anal. Bioanal. Chem.* **394,** 1827–32 (2009).

88. De Jesús, M. a., Giesfeldt, K. S. & Sepaniak, M. J. Improving the analytical figures of merit of SERS for the analysis of model environmental pollutants. *J. Raman Spectrosc.* **35,** 895–904 (2004).

89. De Jesús, M. a., Giesfeldt, K. S. & Sepaniak, M. J. Use of a sample translation technique to minimize adverse effects of laser irradiation in surface-enhanced Raman spectrometry. *Appl. Spectrosc.* **57,** 428–438 (2003).

90. Swapp, S. Scanning Electron Microscopy (SEM). *Geochemical Instrumentation and Analysis* 2 (2015). at <http://serc.carleton.edu/research_education/geochemsheets/techniques/SEM.html>

91. R. F. Egerton. *Physical principles of electron microscopy*. **8,** (Springer, 2005).

92. Goodge, J. Energy-Dispersive X-Ray Spectroscopy (EDS). *Geochemical Instrumentation and Analysis* 2 (2015). at <http://serc.carleton.edu/research_education/geochemsheets/eds.html>

93. Paramelle, D. *et al.* Rapid method to estimate the concentration of citrate capped silver nanoparticles from UV-visible light spectra. *Analyst* **139,** 4855–4861 (2014).

94. Haiss, W., Thanh, N. T. K., Aveyard, J. & Fernig, D. G. Determination of Size and Concentration of Gold Nanoparticles from UV - Vis Spectra. **79,** 4215–4221 (2007).

95. Krishnan, B. Y. R. S., Sc, F. a & Balasubramanian, K. Spectrum Hydrochloride of Hydroxylamine. 285–292 (1964).

96. Yaffe, N. R. & Blanch, E. W. Effects and anomalies that can occur in SERS spectra of biological molecules when using a wide range of aggregating agents for hydroxylamine-reduced and citrate-reduced silver colloids. *Vib. Spectrosc.* **48,** 196–

201 (2008).

97. Sánchez-Cortés, S. & García-Ramos, J. V. Anomalous Raman bands appearing in surface-enhanced Raman spectra. *J. Raman Spectrosc.* **29,** 365–371 (1998).

98. Bhatia, P. *et al.* Onset of Intense Surface Enhanced Raman Scattering and Aggregation in the Au @ Ag System. **2015,** 11 (2015).

99. Huynh, K. a. & Chen, K. L. Aggregation kinetics of citrate and polyvinylpyrrolidone coated silver nanoparticles in monovalent and divalent electrolyte solutions. *Environ. Sci. Technol.* **45,** 5564–5571 (2011).

100. Badawy, a. M. E. *et al.* Impact of environmental conditions (pH, ionic strength,and electrolyte type) on the surface charge and aggregation of silver nanoparticle suspensions. *Environ. Sci. Technol.* **44,** 1260–1266 (2010).

101. Giannini, V., Rodríguez-Oliveros, R. & Sánchez-Gil, J. a. Surface plasmon resonances of metallic nanostars/nanoflowers for surface-enhanced Raman scattering. *Plasmonics* **5,** 99–104 (2010).

102. Kleinman, S. L. *et al.* Structure enhancement factor relationships in single gold nanoantennas by surface-enhanced raman excitation spectroscopy. *J. Am. Chem. Soc.* **135,** 301–308 (2013).

103. Nagashree, K. L., Lavanya, R., Kavitha, C., Narayanan, N. S. V & Sampath, S. Spontaneous formation of branched nanochains from room temperature molten amides: visible and near-IR active, SERS substrates for non-fluorescent and fluorescent analytes. *Rsc Adv.* **3,** 8356–8364 (2013).

104. Shebanova, O. N. & Lazor, P. Raman study of magnetite (Fe3O4): Laser-induced thermal effects and oxidation. *J. Raman Spectrosc.* **34,** 845–852 (2003).

105. Lin, X. M., Cui, Y., Xu, Y. H., Ren, B. & Tian, Z. Q. Surface-enhanced raman spectroscopy: Substrate-related issues. *Anal. Bioanal. Chem.* **394,** 1729–1745 (2009).

106. Marques, A. C. Desenvolvimento de um sensor colorimétrico em papel para a deteção de bactérias eletroquimicamente ativas. (Universidade Nova de Lisboa, 2014).

107. Castro, K. *et al.* Assessment of the weathering effects on cellulose based materials through a multianalytical approach. *Nucl. Instruments Methods Phys. Res. Sect. B Beam Interact. with Mater. Atoms* **269,** 1401–1410 (2011).

108. Tănase, I. G., Udrştioiu, F. M., Bunaciu, A. a. & Aboul-Enein, H. Y. Validation of Raman and FTIR Spectroscopy Methods in Forensic Analysis of Questioned Documents. *Appl. Spectrosc. Rev.* **47,** 484–494 (2012).

109. Sutcu, M. & Akkurt, S. The use of recycled paper processing residues in making porous brick with reduced thermal conductivity. *Ceram. Int.* **35,** 2625–2631 (2009).

110. Costa, M. Desenvolvimento de Microfluídica em Papel para Utilização em Biossensores. (Universidade Nova de Lisboa, 2012).

111. Österberg, M., Schmidt, U. & Jääskeläinen, A.-S. Combining confocal Raman spectroscopy and atomic force microscopy to study wood extractives on cellulose surfaces. *Colloids Surfaces A Physicochem. Eng. Asp.* **291,** 197–201 (2006).

112. Wiley, H. & Atua, R. H. Band assignments in the Raman spectra of celluloses. *Science*

(80-.). **160,** 113–129 (1987).

113. Michaelian, K. H. The Raman spectrum of kaolinite #9 at 21°C. *Can. J. Chem.* **64,** 285–294 (1986).

114. Bell, S. E. J., Sirimuthu, N. M. S. & Colloids, C. S. Surface-Enhanced Raman Spectroscopy as a Probe of Competitive Binding by Anions to Citrate-Reduced Silver Colloids Surface-Enhanced Raman Spectroscopy as a Probe of Competitive Binding by Anions to. *Society* **109,** 7405–7410 (2005).

115. PubChem Compound Database. Chemical Structure of Citrate (CID=31348). *National Center for Biotechnology Information* at <http://pubchem.ncbi.nlm.nih.gov/compound/citrate#section=Top>

116. Zhang, Y., Wang, F., Yin, H. & Hong, M. Nonuniform Distribution of Capping Ligands Promoting Aggregation of Silver Nanoparticles for Use as a Substrate for SERS. *Adv. Nanoparticles* **2013,** 104–111 (2013).

117. Tada, H., Bronkema, J. & Bell, a T. Application of in situ surface-enhanced Raman spectroscopy (SERS) to the study of citrate oxidation on silica-supported silver nanoparticles. *Catal. Letters* **92,** 93–99 (2004).

118. Silva, A. M. N., Kong, X., Parkin, M. C., Cammack, R. & Hider, R. C. Iron(III) citrate speciation in aqueous solution. *Dalton Trans.* 8616–8625 (2009).

119. Lewis, S. *et al.* Chelate-Modified Fenton Reaction for the Degradation of Trichloroethylene in Aqueous and Two-Phase Systems. *Environ. Eng. Sci.* **26,** 849–859 (2009).

120. Greeneltch, N. G., Blaber, M. G., Henry, A.-I., Schatz, G. C. & Van Duyne, R. P. Immobilized nanorod assemblies: fabrication and understanding of large area surface-enhanced Raman spectroscopy substrates. *Anal. Chem.* **85,** 2297–2303 (2013).

121. Fathi, F., Lagugné-Labarthet, F., Pedersen, D. B. & Kraatz, H.-B. Studies of the interaction of two organophosphonates with nanostructured silver surfaces. *Analyst* **137,** 4448 (2012).

122. Spencer, K. M., Sylvia, J. M., Clauson, S. L., Bertone, J. F. & Christesen, S. D. Surface-Enhanced Raman for Monitoring Toxins in Water. *Proc. SPIE* **5268,** 340–348 (2004).

123. Mcdonnell, G. & Russell, a. D. Antiseptics and disinfectants: Activity, action, and resistance. *Clin. Microbiol. Rev.* **12,** 147–179 (1999).

124. Brayner, R., Fiever, F. & Thibaud, C. Nanomaterials: A Danger or a Promise? 407 (2013).

Appendix

I. Chemicals, materials and instruments

i. Chemicals reagents

Reagent	Supplier
Domoic Acid 99% ($C_{15}H_{21}NO_6$) Hydrochloric Acid 98% (HCl) Hydroxylamine 50 wt. % in H_2O (NH_2OH); Malathion PESTANAL® 98,7% ($C_{10}H_{19}O_6PS_2$) Silver Nitrate 99,8% ($AgNO_3$) Sodium Citrate Tribasic Dihydrate 99% ($HOC(COONa)(CH_2COONa)_2 \cdot 2H_2O$) Sodium Hydroxide 98% (NaOH) Tannic Acid ($C_{76}H_{52}O_{46}$) Tetrathylrhodamine Hydrochloride (Rhodamine 6G - $C_{28}H_{31}N_2O_3Cl$)	Sigma-Aldrich
Acetone ($CH_3(CO)CH_3$)	Labchem
Industrial Nitrogen	Air Liquide
Sodium Chloride 99,5% (NaCl)	Scharlau

All chemicals were used without further purification or modification and 18.2 $M\Omega.cm^{-1}$ Milli-Q water (purified by a Millipore system - *Millipore Corporation*) was used throughout the synthesis and experiments.

ii. Materials

Material	Supplier
Whatman no.1 paper	Whatman International Ltd., Florham Park, NJ
Office Paper	300% Portucel Soporcel Group, Setúbal, Portugal

Mono crystalline silicon wafer (500 μm), soda lime glass (1 mm) and cardboard packaging substrate (cellulose fibers pressed with polymeric coatings and evaporated aluminium) were also used as support for SERS substrates.

iii. Instruments

Instrument	Supplier
Analytical Balance AS 220/C/2	Radwag
Centrifuge	Eppendorf
Heating Plate	Heidolph MR HeiTec, Schwabach, Germany
Heating Plate Agimatic-N Ultrasonic Bath Ultra-Sons P	Selecta
pH Electrode Basic 20+	Crison
Wax Printer	Xerox ColorCube 8570, Xerox Corporation, Norwalk, CT, USA

II. Laser power from different filters

Table II. 1|The spectrometer used in this work had six filters and the higher its identification number, the lower the laser power reaching the sample.

Laser Filter	*Objective of 50x Power*	*Units*
Without Filter	*7.87*	*mW*
D0,3	*4.02*	*mW*
D0,6	*1.75*	*mW*
D1	*660*	*µW*
D2	*86.6*	*µW*
D3	*11.8*	*µW*
D4	*1.44*	*µW*

III. Determining diameter and molar concentration of spherical citrate-capped silver nanoparticles in water according to Paramelle *et al.* method

The molar extinction coefficient value (ε) can be used to calculate the particle molar concentration (c) in mol *per* liter from the absorption (A) at the particles measured λ_{max}, using the Lambert-Beer law: A= εbc. b is the path length of light through the sample (usually 1 cm for a cuvette).

The diameter is estimated by λ_{max} at the LSPR band of the colloidal solution of AgNPs.

Table III. 1|Data for determining molar concentration of spherical citrate-capped silver nanoparticles in water using UV-Vis spectra. Adapted from[93]

d / nm	λ_{max} / nm	ε / M^{-1} cm^{-1} · 10^8	d / nm	λ_{max} / nm	ε / M^{-1} cm^{-1} · 10^8
8	392.0*	1.84	56	427.0	658
10	392.1*	5.56	58	429.2	699
12	395.2*	10.1	60	431.5	739
14	397.2*	15.8	62	433.8	779
16	398.5*	22.7	64	436.2	820
18	399.7*	31.3	66	438.7	860
20	400.8	41.8	68	441.3	900
22	401.6	54.8	70	443.8	941
24	402.5	70.8	72	446.7	981
26	403.5	90.5	74	449.5	1021
28	404.5	115	76	452.3	1062
30	405.6	145	78	455.3	1102
32	406.8	181	80	458.3	1142
34	408.1	215	82	461.4	1183
36	409.4	255	84	464.6	1223
38	410.8	295	86	467.9	1263
40	412.3	336	88	471.2	1304
42	413.9	376	90	474.6	1344
44	415.5	416	92	478.1	1384
46	417.3	457	94	481.6	1425
48	419.1	497	96	485.3	1465
50	420.9	537	98	489.0	1505
52	422.9	578	100	492.8	1546
54	424.9	618			

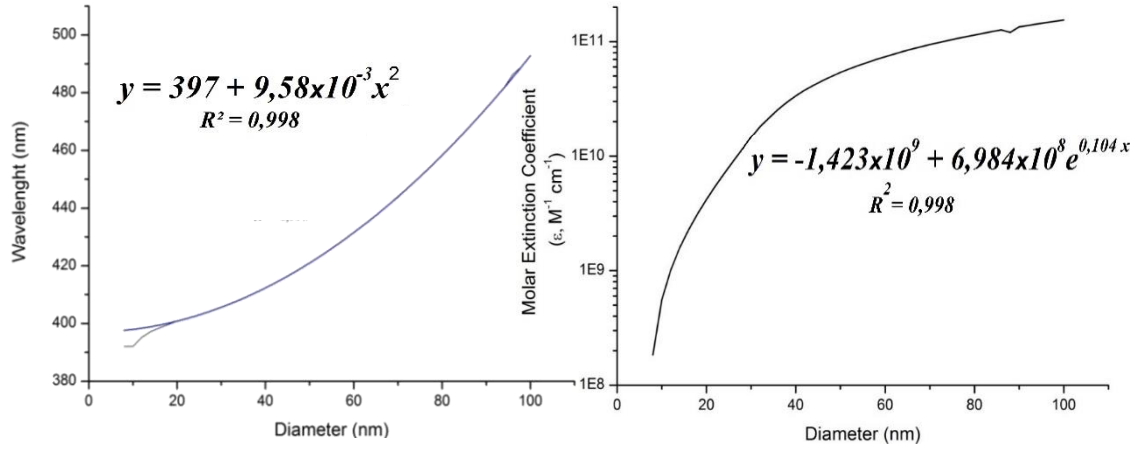

Figure III. 1|Comparison of absorbance peaks for silver nanoparticles obtained experimentally (*black*) and according with Mie theory (*blue*) (*on the left)*. For determining molar concentration of spherical citrate-capped silver nanoparticles in water using nanoparticle size (*on the right*) (a*dapted from*[93]).

IV. Formation Mechanism of Ag Nanoparticles

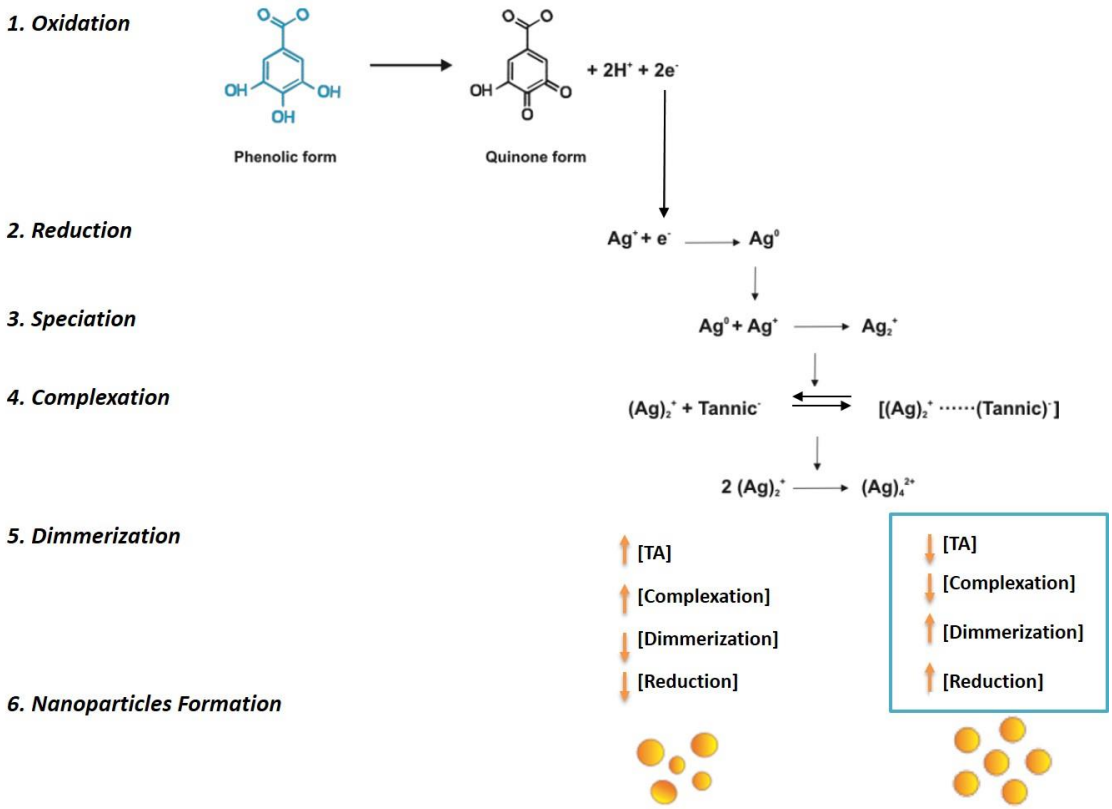

Figure IV. 1|(1) Oxidation. Oxidation of the phenolic hydroxyls of TA to form quinone form. (2) Reduction. The quinone form of TA, allows a donation of two electrons for the reduction of Ag+ precursor. (3) Speciation. Production of Ag0 and further formation of Ag2+. (4) Complexation. Formation of complex between TA and the new spice, Ag2+. (5) Dimerization. This phenomenon depends on the TA concentration, higher TA concentrations leads to an increase in the complexation and consequently, the rate of nucleation slows, (6) which leads to the formation of larger Ag NPs with irregular sizes. When TA is in low concentrations (5), the reduction is fast leading to a (6) rapid nucleation and hence, to small monodisperse AgNPs (*adapted from*[83]).

The tannic acid (TA) consists in a central core of glucose linked by ester bonds to polygalloyl ester chains. This reagent has different roles in the mechanism of AgNPs formation, as reducing agent, stabilizer and complexation agent. The phenolic hydroxyls from TA undergo in a two-electron oxidation (quinone form) donating two electrons for reduction of Ag^+ precursor. Then, the presence of Ag^+ originates Ag^0 followed by a formation of a new specie, Ag_2^+. Subsequently, TA interacts with Ag_2^+ forming [Ag_2^+-TA] complexes that undergoes in slower transformations compared to the un-complexed Ag_2^+ which dimerizes and forms Ag_4^{2+}, the monomer for formation of AgNPs. This seed formation proceeds according to the La Mer model and depends on the complexation of TA with Ag_2^+, hence, is governed by the TA concentration.

According to the La Mer model, homogenous nanoparticle dispersions are favored by a single, rapid nucleation that happens when it is verified a rapid depletion of the reactants. If the concentration of TA is high, the complexation rate increases and the conversion from Ag_2^+ into Ag_4^{2+} and consequently the particle formation is slow leading to variations in growth rate for seed particles formed at different reaction times. Therefore, favoring the formation of large and polidisperse AgNPs. On the other hand, at low concentrations, TA acts as a primary reducer leading to a fast nucleation event and all subsequent growth occurs on the pre-existing nuclei leading to monodisperse AgNPs. Once the catalytic nuclei are formed, sodium citrate (SC) functions as secondary reducer and strong complexing stabilizer.[28,83,124]

V. Study the stability of the AgNPs

A. By variation of ionic strength

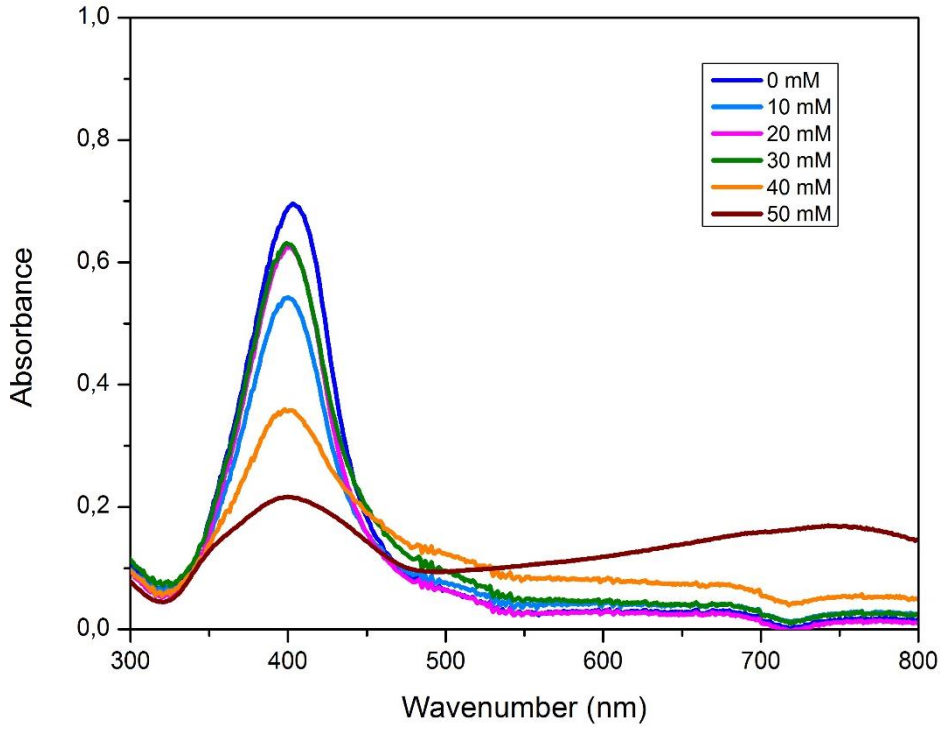

Figure V. 1|UV-Vis spectra of AgNPs obtained using different NaCl concentrations. The CCC achieved was 50 mM – *red* spectrum. The aggregated AgNPs present two main LSPR bands centred approximately at 401 nm with a narrower bandwidth and a new and progressively broadening band at ≈743 nm.

B. By variation of pH value

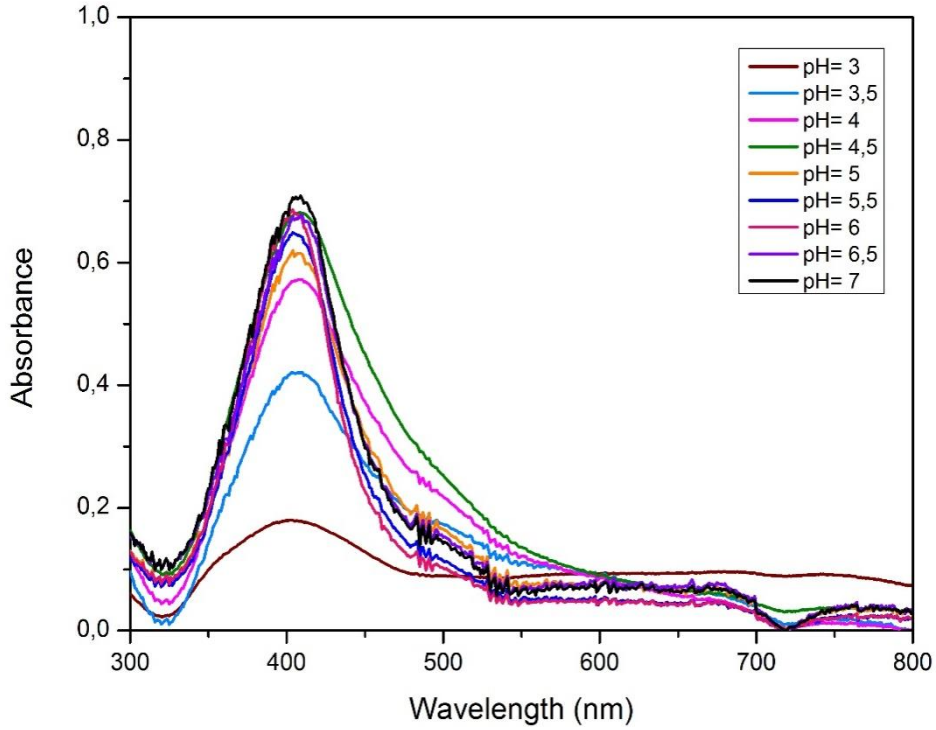

Figure V. 2|UV-Vis spectra of AgNPs obtained by different pH values. The aggregated AgNPs present two main LSPR bands centred approximately at 401 nm with a narrower bandwidth and a new and progressively broadening band at 743 nm.

VI. Distribution of AgNSs by the two papers: Whatman no.1 and Office paper.

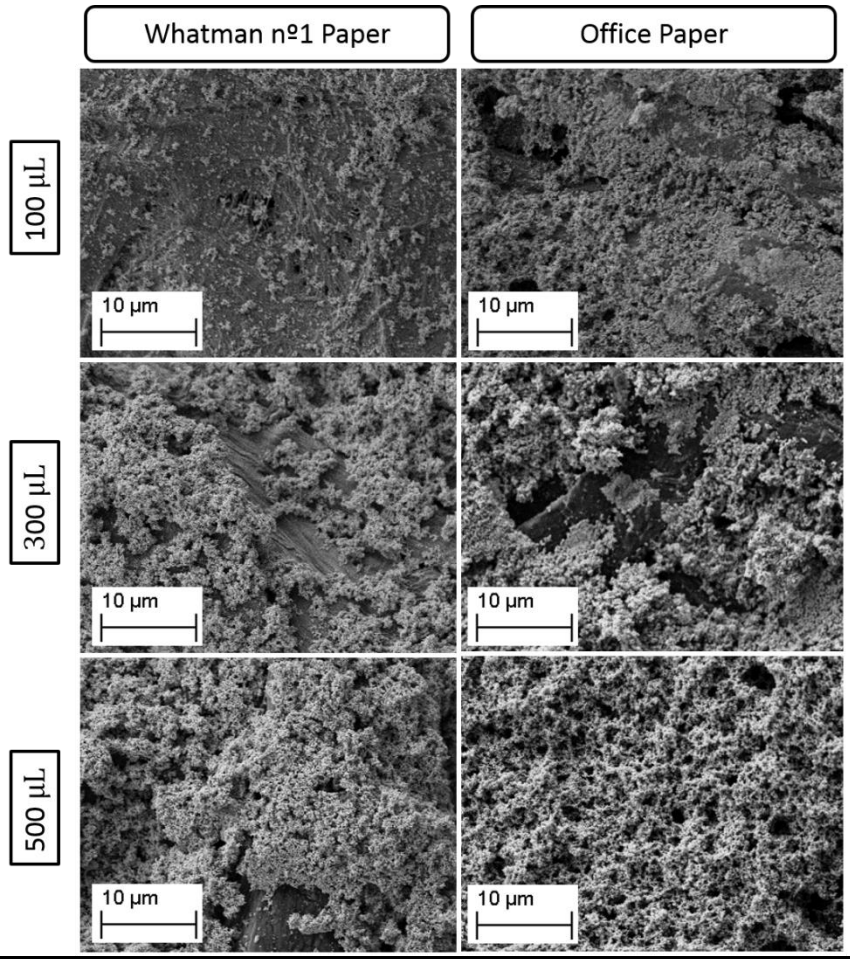

Figure VI. 1|SEM images of AgNSs in the two types of papers: Whatman no.1 (*on the left*) and office (*on the right*) paper to evaluate their distribution. From the top to the bottom of the figure, the volume added onto the paper well increases being 100 µL (*on the top*), 300 µL (*on the middle*) and 500 µL (*on the bottom*). The SEM images show that for higher volumes added, more NPs can be seen on the paper surface regardless of the type of paper. However, for office paper, the necessary amount to cover the same area of the paper surface is much lesser than for Whatman no.1 paper.

VII. Porosity of Whatman no.1 and office paper

As in previous studies,[106,110] the SEM images represented next show the surface morphology of paper substrates used to support the development of substrate for SERS. Due to its composition, manufacturing process and purpose, there are differences in the morphology of the two paper surfaces. Although both are made of a three-dimensional network of intertwined cellulose fibers, paper Whatman no.1 has more cylindrical fibers thereby contributing to greater thickness and porosity, while observing flatter fiber and a higher density for office paper. The high fiber density of the office paper and the coating enables obtaining a more uniform surface and therefore an evenly distribution of NPs and over the surface.

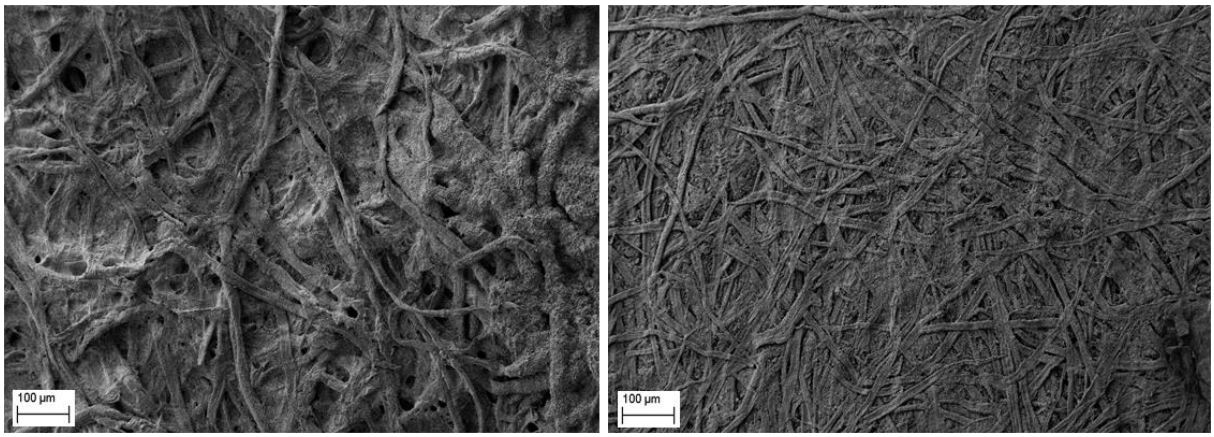

Figure VII. 1|SEM image of the surface morphology of paper substrates used to support the development of substrate for SERS. Due to its composition, manufacturing process and purpose, there are differences in the morphology of the two paper surfaces. The high fiber density of the office paper enables obtaining a more uniform surface and therefore an evenly distribution of NPs and over the surface.

VIII. EDS analysis on two different papers: Whatman no.1 and office paper

A. Distribution map of the key elements identified in Whatman no.1 paper.

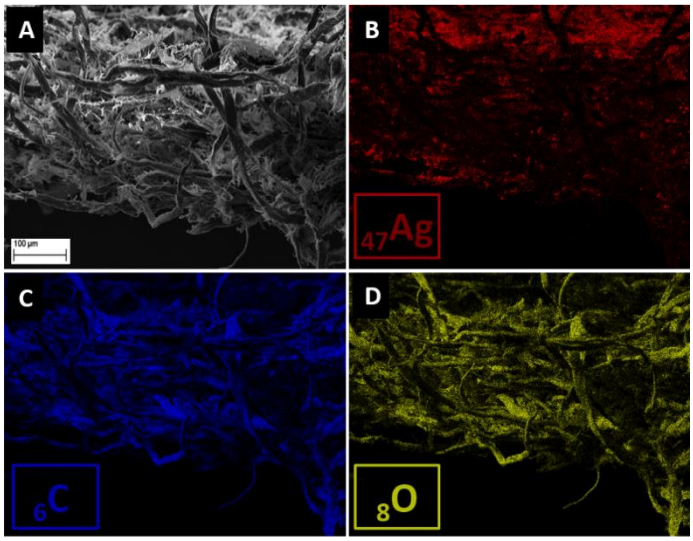

Figure VIII. 1|(A) SEM image of a well corresponding to the paper SERS substrate in Whatman no.1 paper. Results from EDS analysis of a cross section of the paper for the (B) silver; (C) carbon and (D) oxygen elements. The Ag element is observed along the thickness of the paper. The carbon and oxygen elements are the main constituents of this paper substrate, so the images display the fibers in the image of SEM.

B. Distribution map of the key elements identified in office paper.

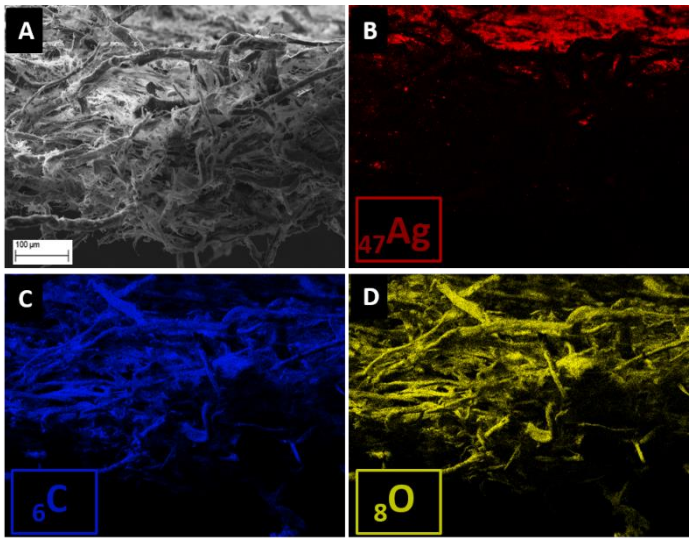

Figure VIII. 2|(A) SEM image of a well corresponding to the paper SERS substrate in office paper. Results from EDS analysis of a cross-section of the paper for the (B) silver; (C) carbon and (D) oxygen elements. The Ag element is observed nearly only the surface of the office paper. The carbon and oxygen elements are the main constituents of this paper substrate, so the images display the fibers in the image of SEM.

IX. Spectra of R6G with silver nanoparticles in Whatman no.1 paper

A. SERS spectra for citrate capped non-aggregated silver nanoparticles non-aggregated

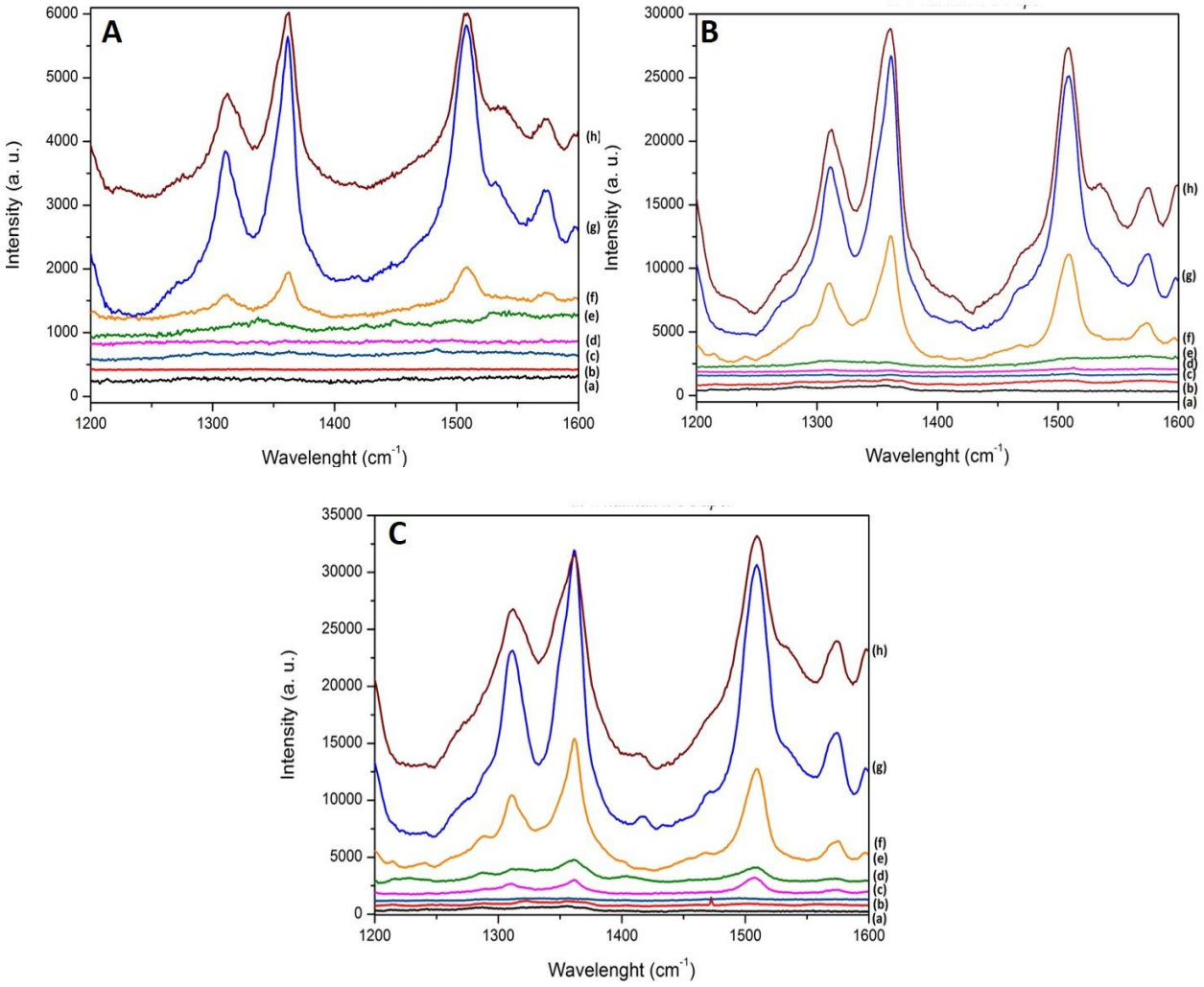

Figure IX. 1|R6G SERS spectra in wells of 4 mm diameter with non-aggregated AgNPs: (A) 100; (B) 300 and (C) 500 µL *drop-casted* in Whatman no.1 paper. For all the sets of SERS spectra the corresponding legend is: (a) well without the R6G, *i.e.*, with the 100, 300 or 500 µL of non-aggregated AgNPs in Whatman no.1 paper; same well conditions and with several R6G concentrations added: (b) 10^{-9} M; (c) 10^{-8} M; (d) 10^{-7} M; (e) 10^{-6} M; (f) 10^{-5} M; (g) 10^{-4} M; and (h) 10^{-3} M.

B. SERS spectra for citrate capped aggregated silver nanoparticles

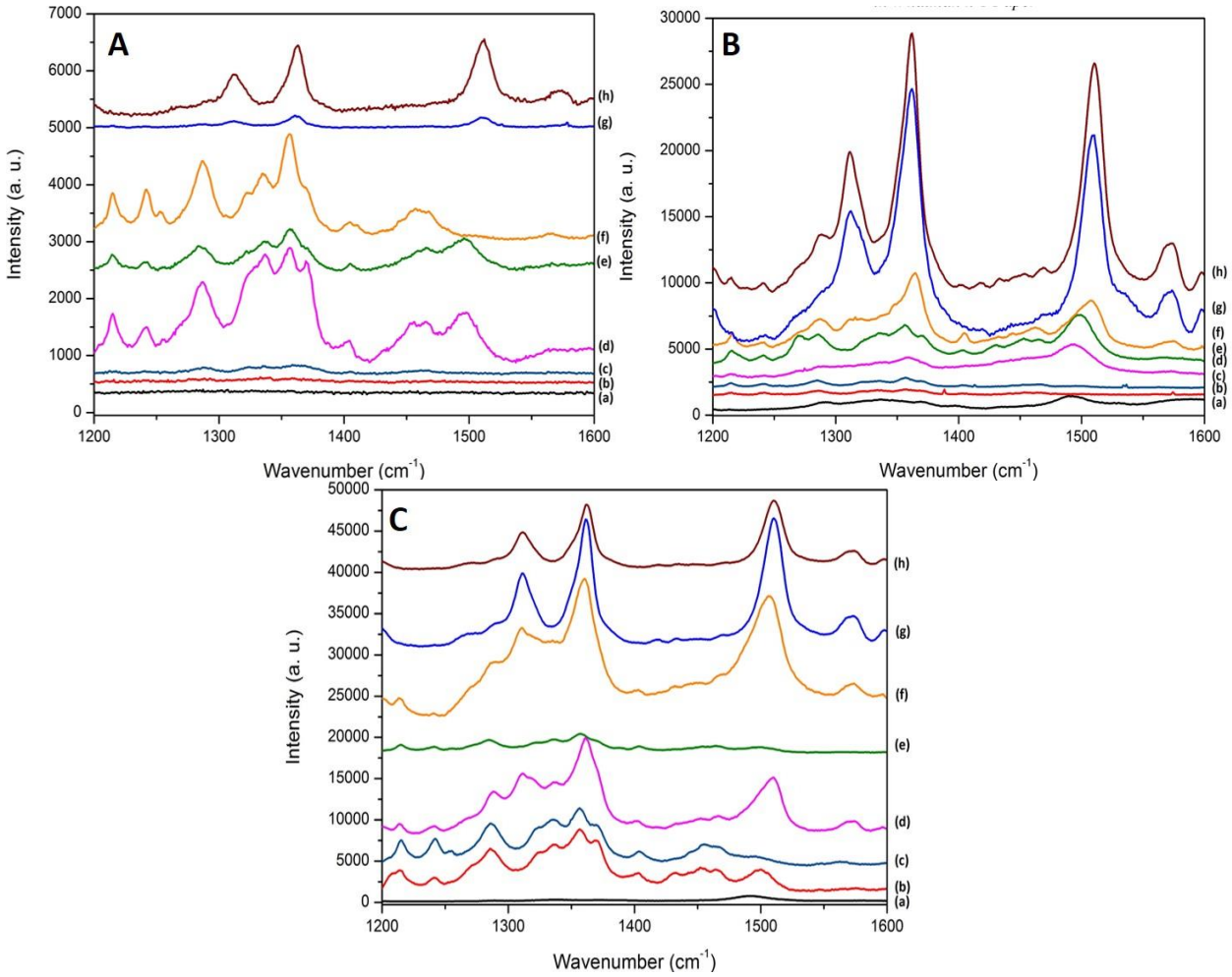

Figure IX. 2|R6G SERS spectra in wells of 4 mm diameter with aggregated AgNPs: (A) 100; (B) 300 and (C) 500 µL *drop-casted* in Whatman no.1 paper. For all the sets of SERS spectra the corresponding legend is: (a) well without the R6G, *i.e.*, with the 100, 300 or 500 µL of aggregated AgNPs in Whatman no.1 paper; same well conditions and with several R6G concentrations added: (b) 10^{-9} M; (c) 10^{-8} M; (d) 10^{-7} M; (e) 10^{-6} M; (f) 10^{-5} M; (g) 10^{-4} M; and (h) 10^{-3} M.

C. SERS spectra for citrate capped star-shaped silver nanoparticles

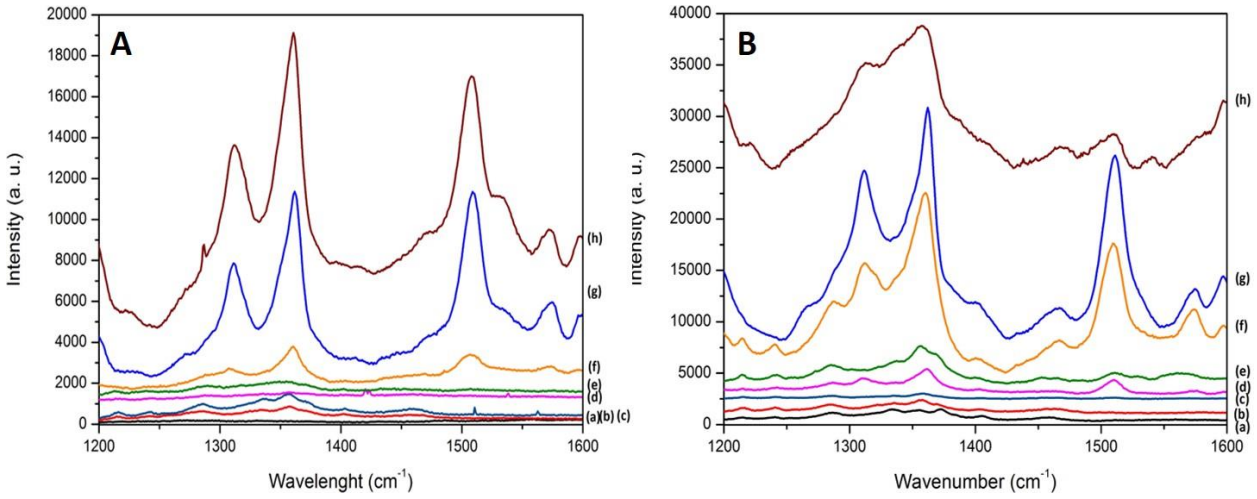

Figure IX. 3|R6G SERS spectra in wells of 4 mm diameter with AgNSs: (A) 100 and (B) 300 µL *drop-casted* in Whatman no.1 paper. For all the sets of SERS spectra the corresponding legend is: (a) well without the R6G, *i.e.*, with the 100 or 300 µL of AgNSs in Whatman no.1 paper; same well conditions and with several R6G concentrations added: (b) 10^{-9} M; (c) 10^{-8} M; (d) 10^{-7} M; (e) 10^{-6} M; (f) 10^{-5} M; (g) 10^{-4} M; and (h) 10^{-3} M.

X. Spectra of R6G with silver nanoparticles in office paper

A. SERS spectra for citrate capped non-aggregated silver nanoparticles

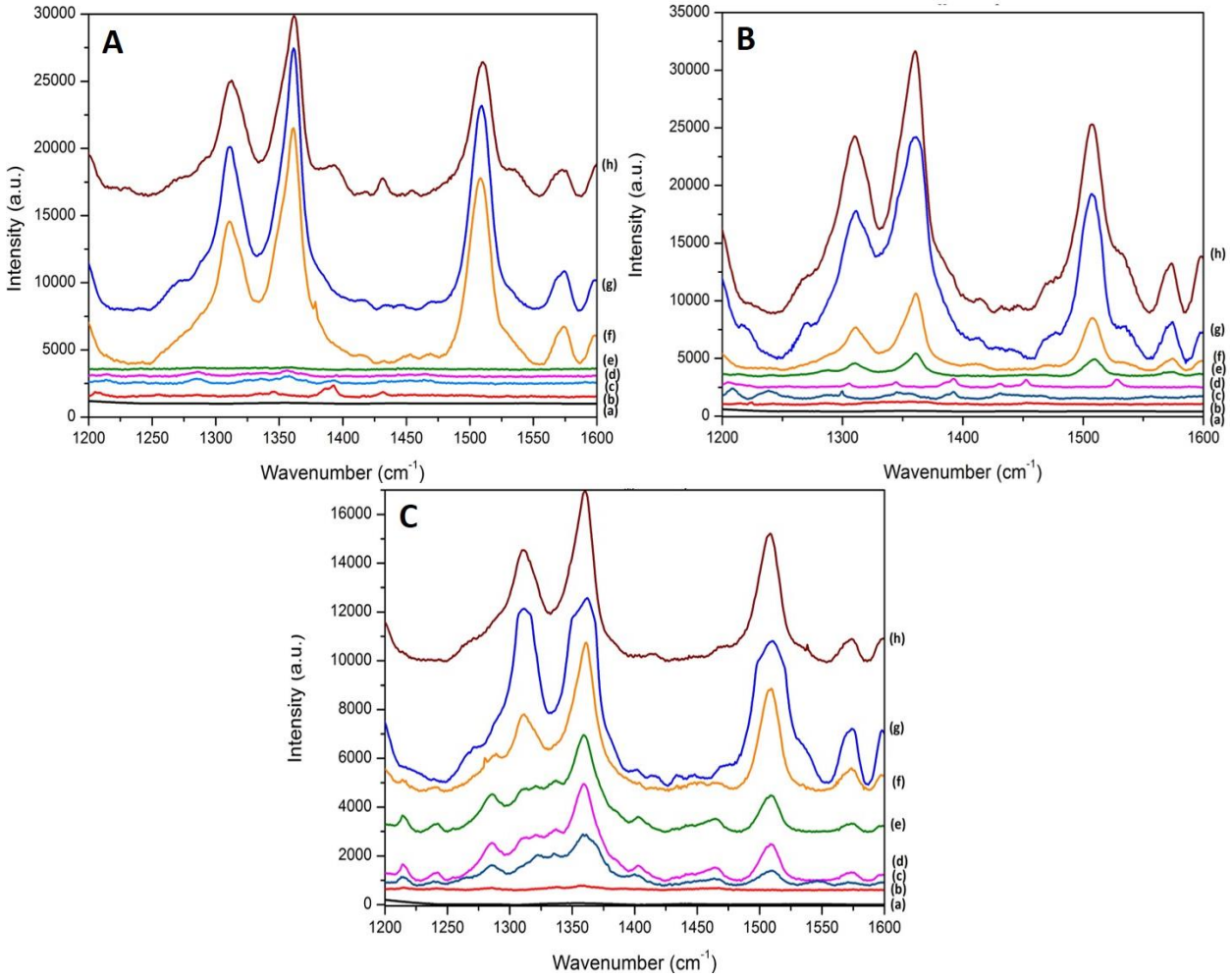

Figure X. 1|R6G SERS spectra in wells of 4 mm diameter with non-aggregated AgNPs: (A) 100; (B) 300 and (C) 500 µL *drop-casted* in office paper. For all the sets of SERS spectra the corresponding legend is: (a) well without the R6G, *i.e.*, with the 100, 300 or 500 µL of non-aggregated AgNPs in office paper; same well conditions and with several R6G concentrations added: (b) 10^{-9} M; (c) 10^{-8} M; (d) 10^{-7} M; (e) 10^{-6} M; (f) 10^{-5} M; (g) 10^{-4} M; and (h) 10^{-3} M.

B. SERS spectra for citrate capped aggregated silver nanoparticles

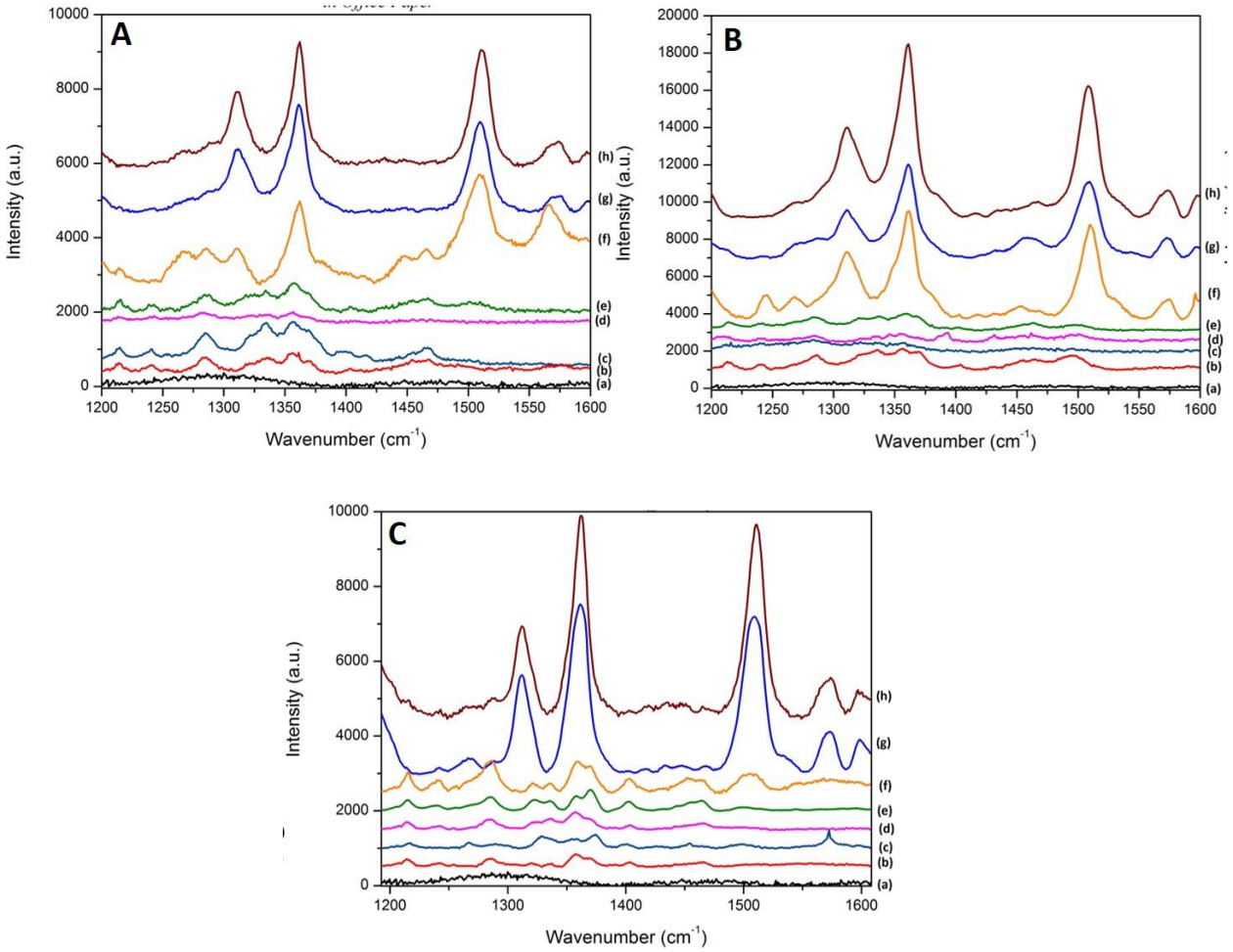

Figure X. 2|R6G SERS spectra in wells of 4 mm diameter with aggregated AgNPs: (A) 100; (B) 300 and (C) 500 µL *drop-casted* in office paper. For all the sets of SERS spectra the corresponding legend is: (a) well without the R6G, *i.e.*, with the 100, 300 or 500 µL of aggregated AgNPs in office paper; same well conditions and with several R6G concentrations added: (b) 10^{-9} M; (c) 10^{-8} M; (d) 10^{-7} M; (e) 10^{-6} M; (f) 10^{-5} M; (g) 10^{-4} M; and (h) 10^{-3} M.

C. SERS spectra for citrate capped star-shaped silver nanoparticles

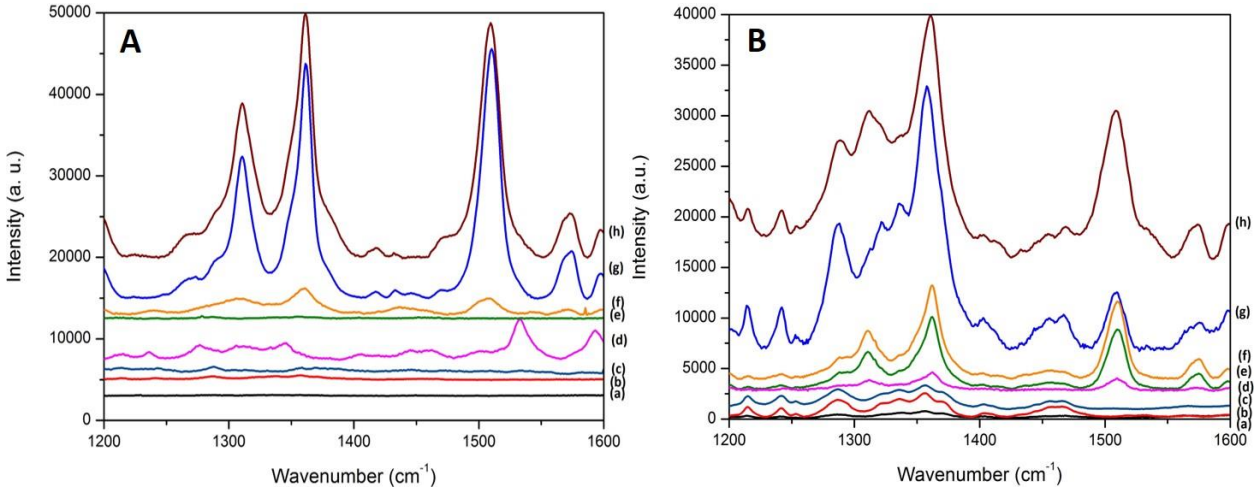

Figure X. 3|R6G SERS spectra in wells of 4 mm diameter with AgNSs: (A) 100; (B) 300 and (C) 500 µL *drop-casted* in office paper. For all the sets of SERS spectra the corresponding legend is: (a) well without the R6G, *i.e.*, with the 100, 300 or 500 µL of non-aggregated AgNSs in office paper; same well conditions and with several R6G concentrations added: (b) 10^{-9} M; (c) 10^{-8} M; (d) 10^{-7} M; (e) 10^{-6} M; (f) 10^{-5} M; (g) 10^{-4} M; and (h) 10^{-3} M.

XI. Optimization of paper SERS substrate

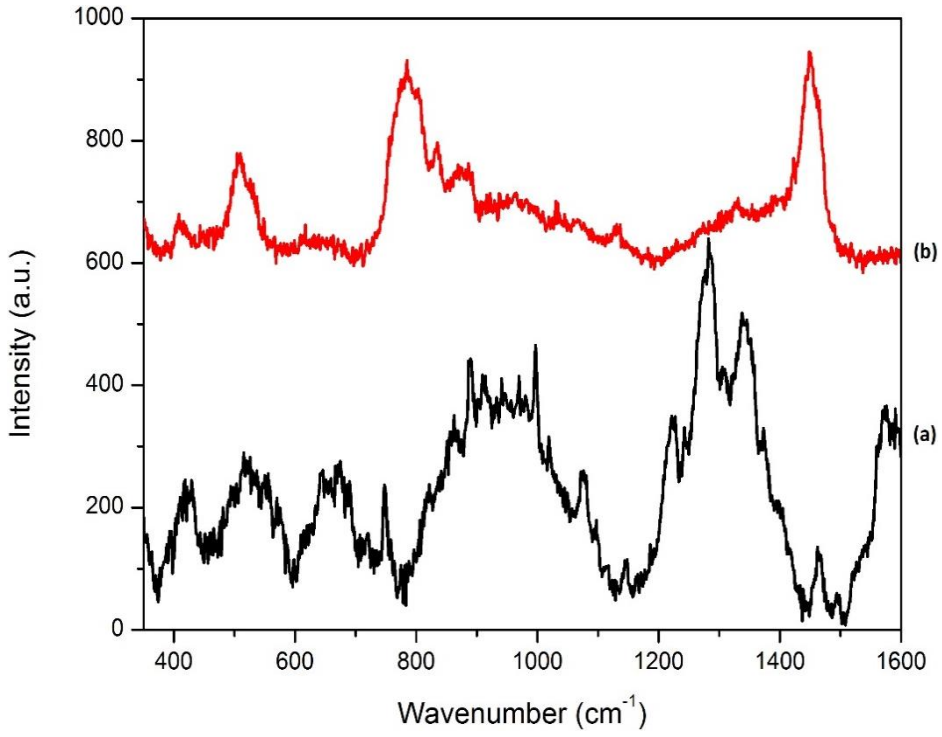

Figure XI. 1|SERS spectra of malathion deposited on the wells submitted to treatments (a) 1 mM $FeCl_2$ and (b) 2 M HCl. For both spectra the signal from malathion did not had be demonstrated.

XII. Reproducibility between different AgNSs synthesis batches

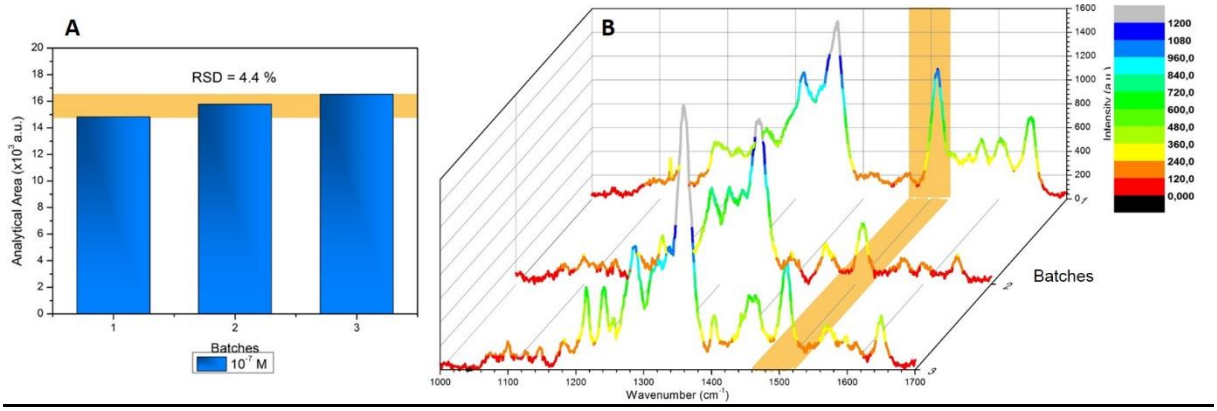

Figure XII. 1|Reproducibility of SERS substrate (office paper with AgNSs *drop-casted*). (A) Area distribution of the 1509 cm^{-1} band in the spectra *versus* the number of batches. Each data point represents the average value from three SERS spectra measured at the vicinity of each spot. The *yellow* region shows the relative standard deviation (RSD = 4.4 %). (B) SERS spectra of 10^{-7} M R6G recorded from the optimized SERS substrate fabricated by three different batches of AgNSs colloidal solution.

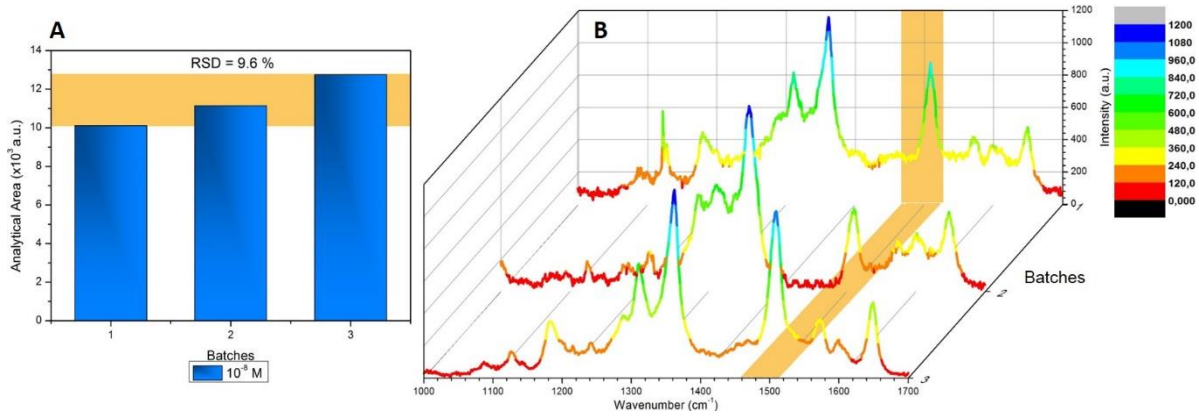

Figure XII. 2|Reproducibility of SERS substrate (office paper with AgNSs *drop-casted*). (A) Area distribution of the 1509 cm^{-1} band in the spectra *versus* the number of batches. Each data point represents the average value from three SERS spectra measured at the vicinity of each spot. The *yellow* region shows the relative standard deviation (RSD = 9.6 %). (B) SERS spectra of 10^{-8} M R6G recorded from the optimized SERS substrate fabricated by three different batches of AgNSs colloidal solution.

XIII. Time Stability Study of the paper SERS substrate

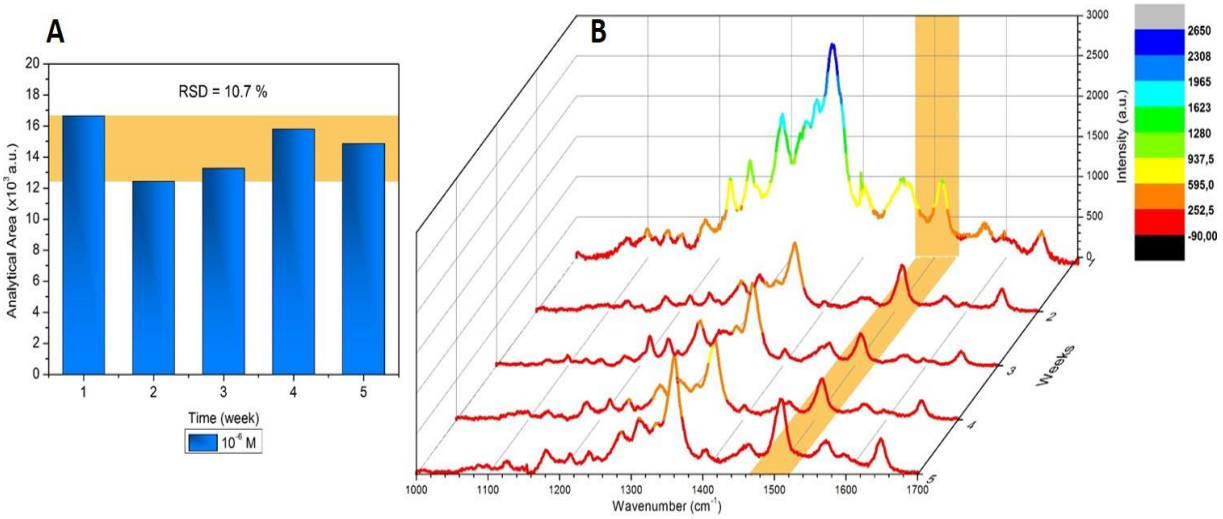

Figure XIII. 1|Stability of SERS substrate (office paper with AgNSs *drop-casted*). (A) Area distribution of the 1509 cm^{-1} band in the spectra *versus* stored time (5 weeks). Each data point represents the average value from three SERS spectra measured at the vicinity of each spot. The *yellow* region shows the RSD (RSD = 10.7 %). (B) SERS spectra of 10^{-6} M R6G recorded from the optimized SERS substrate stored over a number of weeks under at 4ºC in a desiccator.

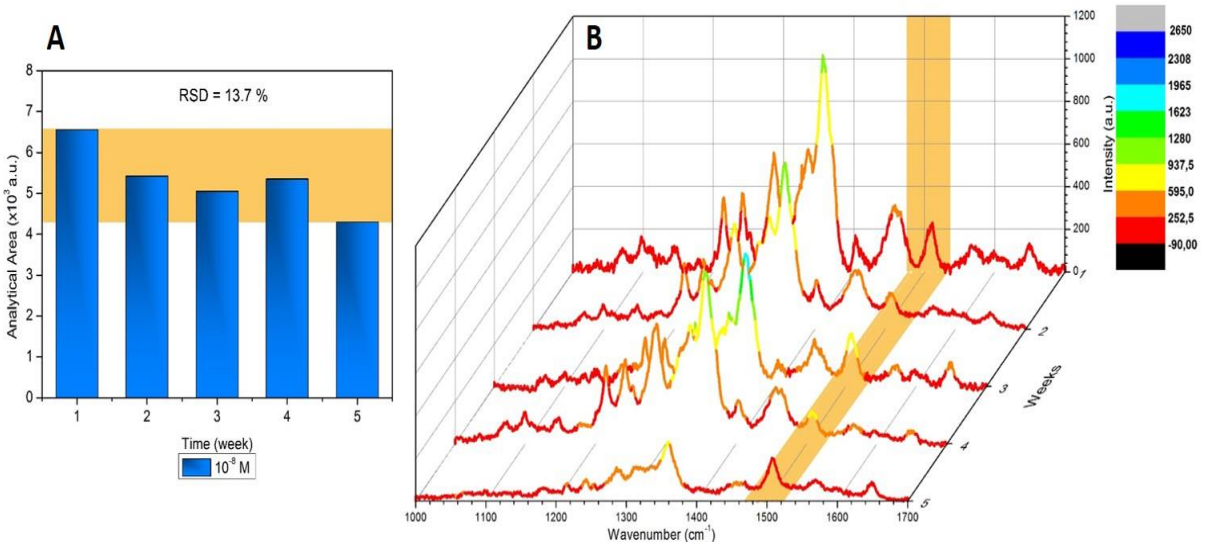

Figure XIII. 2|Stability of SERS substrate (office paper with AgNSs *drop-casted*). (A) Area distribution of the 1509 cm^{-1} band in the spectra *versus* stored time (5 weeks). Each data point represents the average value from three SERS spectra measured at the vicinity of each spot. The *yellow* region shows the RSD (RSD = 13.7 %). (B) SERS spectra of 10^{-8} M R6G recorded from the optimized SERS substrate stored over a number of 5 weeks at 4 ºC in a desiccator.